Deformation-induced ε-martensitic transformation effect and fatigue crack growth mechanism on the low cycle fatigue in high-Mn austenitic alloys

ジュ, ユンバン

https://doi.org/10.15017/1866294

出版情報：Kyushu University, 2017, 博士（工学）, 課程博士
バージョン：
権利関係：

Deformation-induced ε-martensitic transformation effect and fatigue crack growth mechanism on the low cycle fatigue in high-Mn austenitic alloys

A dissertation submitted to the faculty of engineering

Graduate school, Kyushu University, Japan

For the degree of doctor of philosophy

Presented by

Yun-Byum JU

May 2017

Contents

CHAPTER 1. GENERAL INTRODUCTION

1.1 Background of this study

In many industries, technology has been developed and companies have applied the new technology. In past, many companies focused on high performance of their product such as high speed car with high displacement volume. However, increasing environmental regulation, competition of high fuel efficiency and made automobile companies to reduce the weight of their products. And the trend of weight reduction has spread out into other industries and has lasted until now because of a benefit to decrease an entry cost of their products. On the other hand, many automobile companies have also made a lot of efforts in development of new materials to satisfy increasing crash worthiness as shown in Fig. 1.1. The high-Mn austenitic steels have been considered as structural applications in automotive industry [1].

Numerous studies have been performed on high-Mn austenitic steels because of their high strength and ductility. The excellent mechanical properties of high-Mn steels arise from either transformation-induced plasticity (TRIP) or twinning-induced plasticity (TWIP) effects [2, 3]. The dominant plastic deformation mechanism is dependent upon a variety of factors, including the chemical composition and temperature [2, 4-6]. It has been reported that the stacking fault energy (SFE), which depends upon the chemical composition and temperature, controls the plastic deformation mechanisms in high-Mn austenitic steels [4, 5]. Fig. 1.2 shows the volume fraction changes of ε-martensitic transformation in high-Mn austenitic alloys [7]. In the Fe-30Mn-Al-Si alloys, when the Si component increased, the volume fraction of ε-martensitic transformation also increased as shown in Fig. 1.2 (g) and (k). In addition, it has been also reported that the SFE of the Fe-30Mn-3Al-3Si and Fe-30Mn-6Si alloys are 7.8 mJ/m^2 and 40 mJ/m^2, respectively [8, 9]. Therefore, the addition of Al and Si (i.e., solute elements) has been used to control the SFE to obtain the desired TRIP and TWIP effects [2, 10]. The plastic deformation mode of high-Mn austenitic alloys depends on the SFE. The ε-martensitic transformation and mechanical twinning are reported to occur in high-Mn alloys, which have the SFE below 18-20 mJ/m^2 and between 15-45 mJ/m^2, respectively [11, 12]. When the SFE is higher than 45 mJ/m^2, the dominant plastic deformation become dislocation cross-slip [13]. For example, when the SFE is extremely low, e.g., in Fe-30Mn-6Si and Fe-30Mn-4Si-2Al alloys, remarkable ε-martensitic transformation occurs, which result in TRIP effects [10].

Recently, the austenitic TRIP steels that are associated with ε-martensite have received much attention as potential damping materials for buildings because of their superior low-cycle fatigue properties [6, 7, 14]. In previous study, fatigue tests of the Fe-30Mn-xSi-(6-x)Al alloys (x=0~6) were conducted to investigate the fatigue properties as shown in Table 1.1 [6]. And the Fe-30Mn-4Si-2Al alloy has a fatigue life that is more than four times longer than that of conventional austenitic steels, such as TWIP and stainless steels [6]. To clarify the importance of ε-martensitic transformation, the fatigue lives of various high-Mn austenitic steels with different γ/ε phase stabilities have been compared [6]. The results of this comparative study indicated that deformation-induced, reversible, $\gamma \leftrightarrow \varepsilon$ martensitic transformation plays a crucial role in improving the fatigue life [15, 16]. However, the relationship between the low cycle fatigue resistance and effect of ε-martensitic transformation in the Fe-30Mn-4Si-2Al alloy still has remained unclear. Moreover, the fatigue crack growth mechanism of the Fe-30Mn-4Si-2Al alloy has not uncovered.

The fatigue life is composed of the crack initiation period and crack propagation period [17]. The crack initiation life is used in the fatigue life prediction method called ‘safe-life’. In the safe-life design based on the prediction of fatigue crack nucleation, a large margin should be selected to avoid unexpected fails, which can be caused by many factors such as scatter in experiment results and error in expected service load, etc. [18]. And the large margin contributes to the increase in the weight and production cost. For these reason, some industries such as a nuclear power plant, airplane, and etc. that demand a high entry cost and long operating time have used the crack propagation life for the fatigue life prediction. In addition, high-Mn austenitic steels showed short the crack initiation life compared to the crack propagation life in low cycle fatigue. For example, a fatigue crack in the Fe-30Mn-4Si-2Al alloy was initiated at 200 cycles and at a total strain range of 2%, even though the total fatigue life was longer than 11,000 cycles [19]. Therefore, when high-Mn austenitic steels are considered as structural materials in not only these industries but also automobile companies, the study of fatigue crack propagation behavior in high-Mn austenitic steels is important for effective design.

In present study, the Fe-30Mn-6Al, Fe-30Mn-4Si-2Al alloy and Fe-30Mn-6Si alloys were used. The chemical composition and results of tensile test are shown in Table 1.2 and Fig. 1.3 [20]. The SFE and associated plastic deformation mode of three alloys are summarized in Table 1.3 [8-13]. The Fe-30Mn-4Si-2Al alloy, which showed low cycle fatigue resistance, was used to investigate the fatigue crack growth mechanism. In addition, the Fe-30Mn-6Al and Fe-30Mn-6Si alloys, which have slip deformation and ε-martensitic transformation as a dominant plastic deformation mode respectively, were used to compare the effect of ε-martensitic transformation in low cycle fatigue. More specifically, the Fe-30Mn-6Al and Fe-30Mn-4Si-2Al alloys have same initial microstructure and different plastic deformation mode. Therefore, the effect of ε-martensitic transformation on the fatigue crack growth behavior can be compared during low cycle fatigue. The Fe-30Mn-4Si-2Al and Fe-30Mn-6Si alloys have same plastic deformation mode. However, only the Fe-30Mn-6Si alloy shows pre-existing ε-martensite before fatigue test. Therefore, the effects of pre-existing ε-martensite and volume fraction of ε-martensite can be compared.

1.2 Outline of this study

The main theme of this thesis is the investigations of fatigue crack growth mechanisms in high-Mn-austenitic alloys during low-cycle fatigue. The Fe-30Mn-6Al, Fe-30Mn-4Si-2Al and Fe-30Mn-6Si alloys that showed conventional slip deformation, strong low cycle fatigue resistance and highest volume fraction of ε-martensite respectively were used to compare the crack growth mechanisms.

Chapter 1. General introduction of this study was described with research background and outline of this thesis.

Chapter 2. The microstructural changes and macroscopic fatigue crack growth behavior in Fe-30Mn-6Al, Fe-30Mn-4Si-2Al, and Fe-30Mn-6Si alloys were observed in situ by optical microscopy. The results indicate that ε-martensitic transformation in the Fe-30Mn-4Si-2Al alloy has three positive effects on crack growth: I) the suppression of strain localization; II) zigzag crack propagation, which enhances roughness-induced crack closure; and III) subcrack formation, which induced crack toughening, such as stress redistribution. On the other hand, the ε-martensite has a negative effect on crack growth, i.e., it causes subcrack initiation, which leads to the subcrack coalescence with the main crack. However, the ε-martensitic transformation in the Fe-30Mn-4Si-2Al alloy is optimized so that the positive effects are maximized and the negative effect is minimized, which results in the superior resistance of the alloy against low-cycle fatigue.

Chapter 3. In order to examine ε-martensitic transformation effect on localization of plastic strain, plastic strain evolutions in the vicinity of crack path were investigated at different crack lengths in Fe-30Mn-6Al, Fe-30Mn-4Si-2Al, and Fe-30Mn-6Si alloys. Specifically, fractographic analyses and electron backscatter diffraction measurements underneath the fracture surfaces were carried out. In terms of crack tip deformation, the key roles of ε-martensitic transformation are (1) brittle-like cracking along γ/ε interface, (2) inhibition of fatigue damage accumulation, and (3) geometrical constraint of ε-martensite crystallographic structure at a fatigue crack tip. Because of the roles (2) and (3) above, the Fe-30Mn-4Si-2Al alloy showed the lowest fatigue crack growth compared to the other tested alloys. This chapter presents the proposed ε-martensite-related crack growth mechanism in details.

Chapter 4. In order to examine the mechanisms proposed in chapter 2, microscopic fatigue crack growth behaviors of the Fe-30Mn-4Si-2Al and Fe-30Mn-6Si alloys were investigated by in situ SEM observation during one cycle. The results indicate that the Fe-30Mn-6Si alloy has subcrack initiation and cracking behavior caused by pre-existing ε-martensite as a dominant crack growth behavior. The fatigue crack growth rate of the Fe-30Mn-4Si-2Al alloy is delayed due to positive effects of ε-martensitic transformation and annealing twin boundary. The suppression of plastic deformation localization by reverse transformation of ε-martensite and decrease of driving force at a crack tip contributed to low cycle fatigue resistance in the Fe-30Mn-4Si-2Al alloy.

Chapter 5. General conclusion of the each chapters by present studies are summarized.

References

[1] O. Bouaziz, S. Allain, C.P. Scott, P. Cugy, D. Barbier, High manganese austenitic twinning induced plasticity steels: A review of the microstructure properties relationships, Curr. Opin. Solid. State. Mater. Sci. 15 (2011) 141-168.

[2] O. Grässel, L. Krüger, G. Frommeyer, L.W. Meyer, High strength Fe-Mn-(Al, Si) TRIP/TWIP steels development d properties d application, Int. J. Plast. 16 (2000) 1391-1409.

[3] Y.K. Lee, Microstructural evolution during plastic deformation of twinning-induced plasticity steels, Scr. Mater. 66 (2012) 1002-1006.

[4] L. Remy, A. Pineau, Twinning and strain-induced F.C.C. → H.C.P. transformation in the Fe-Mn-Cr-C system, Mater. Sci. Eng. 28 (1977) 99-107.

[5] S. Allain, J.-P. Chateau, O. Bouaziz, S. Migot, N. Guelton, Correlations between the calculated stacking fault energy and the plasticity mechanisms in Fe-Mn-C alloys, Mater. Sci. Eng. A 387 (2004) 158-162.

[6] I. Nikulin, T. Sawaguchi, K. Tsuzaki, Effect of alloying composition on low-cycle fatigue properties and microstructure of Fe-30Mn-(6-x)Si-xAl TRIP/TWIP alloys, Mater. Sci. Eng. A 587 (2013) 192-200.

[7] T. Sawaguchi, I. Nikulin, K. Ogawa, K. Sekido, S. Takamori, T. Maruyama, Y. Chiba, A. Kushibe, Y. Inoue, K. Tsuzaki, Designing Fe-Mn-Si alloys with improved low-cycle fatigue lives, Scr. Mater. 99 (2015) 49-52.

[8] J. Xuejun, Z. Jihua, T.Y. Hsu, Mater. Des. 21 (2000) 537-539.

[9] S. Vercammen, B. Blanpain, B.C. de Cooman, P. wollants, Acta Mater. 52

(2004) 2005-2012.

[10] K. Ogawa, T. Sawaguchi, T. Kikuchi, M. Koyama, M. Murakami, Influence of Al concentration on deformation behavior and fracture mode of fe-30Mn-6(Si, Al) alloys, in: International Conference on Shape Memory and Superelastic Technologies, SMST-2007, 2008.

[11] H.-G. Lambers, C.J. Rusing, T. Niendorf, D. Geissler, J. Freudenberger, H.J. Maier, Int. J. Fat. 40 (2012) 51-60.

[12] Y.F. Shen, C.H. Qiu, L. Wang, X. Sun, X.M. Zhao, L. Zuo, Mater. Sci. Eng. A 561 (2013) 329-337.

[13] M. Iker, D. Gaude-Fugarolas, P.J. Jacques, F. Delannay, Adv. Mater. Res. 15-17 (2007) 852-857.

[14] H. Li, M. Koyama, T. Sawaguchi, K. Tsuzaki, H. Noguchi, Importance of crack propagation-induced ε-martensite in strain-controlled low-cycle fatigue of high-Mn austenitic steel, Phill. Mag. Lett. 95 (2015) 303-311.

[15] T. Sawaguchi, P. Sahu, T. Kikuchi, K. Ogawa, S. Kajiwara, A. Kushibe, M. Higashino, T. Ogawa, Vibration mitigation by the reversible fcc/hcp martensitic transformation during cyclic tension-compression loading of an Fe-Mn-Si-based shape memory alloy, Scr. Mater. 54 (2006) 1885-1890.

[16] T. Sawaguchi, L.G. Bujoreanu, T. Kikuchi, K. Ogawa, M. Koyama, M. Murakami, Mechanism of reversible transformation-induced plasticity of Fe-Mn-Si shape memory alloys, Scr. Mater. 59 (2008) 826-829.

[17] J. Schijve, Fatigue of Structures and Materials, Springer, 2009

[18] S. Suresh, Fatigue of Materials, Cambridge, 1998

[19] H. Li, M. Koyama, T. Sawaguchi, K. Tsuzaki, H. Noguchi, Importance of

crack propagation-induced ε-martensite in strain-controlled low-cycle fatigue of high-Mn austenitic steel, Phill. Mag. Lett. 95 (2015) 303-311

[20] K. Yamada, M. Koyama, T. Kaneko, K. Tsuzaki, Positive and negative effects of hydrogen on tensile behavior in polycrystalline Fe-30Mn-(6-x)Si-xAl austenitic alloys, Scr. Mater. 105 (2015) 54-57.

Table 1.1 LCF life, N_f, Young's modulus, E, and monotonic tensile properties [6].

Material	N_f (cycles)	E (GPa)	$\sigma_{0.2}$ (MPa)	σ_{UTS} (MPa)	n	δ (%)
Fe-30Mn-6Al-0Si	750	156	214	479	0.21	54
Fe-30Mn-5Al-1Si	770	163	228	492	0.20	56
Fe-30Mn-4Al-2Si	1790	171	238	507	0.19	65
Fe-30Mn-3Al-3Si	2112	174	260	574	0.19	72
Fe-30Mn-2Al-4Si	8070	179	290	634	0.18	64
Fe-30Mn-1Al-5Si	2080	174	248	690	0.26	57
Fe-30Mn-0Al-6Si	2024	150	218	745	0.28	30

Table 1.2 Chemical compositions of the alloys used (wt.%) [20].

Alloys	Mn	Al	Si	Fe
Fe-30Mn-6Al	30.1	5.75	0	Bal.
Fe-30Mn-4Si-2Al	29.99	1.98	4.06	Bal.
Fe-30Mn-6Si	30.08	0.004	6.08	Bal.

Table 1.3 SFE and associated plastic deformation mode by chemical composition of Al and Si [8, 9, 11-13].

Alloys	SFE	γ stability	Plastic deformation mode
Fe-30Mn-6Al-0Si	↑	γ stable	Slip deformation
Fe-30Mn-5Al-4Si		↕	
Fe-30Mn-4Al-2Si			
Fe-30Mn-3Al-3Si	40 mJ/m^2		Twinning deformation
Fe-30Mn-2Al-4Si	↕		Twinning / ε-martensitic transformation
Fe-30Mn-1Al-5Si			
Fe-30Mn-0Al-6Si	7.8 mJ/m^2	γ → ε	ε-martensitic transformation

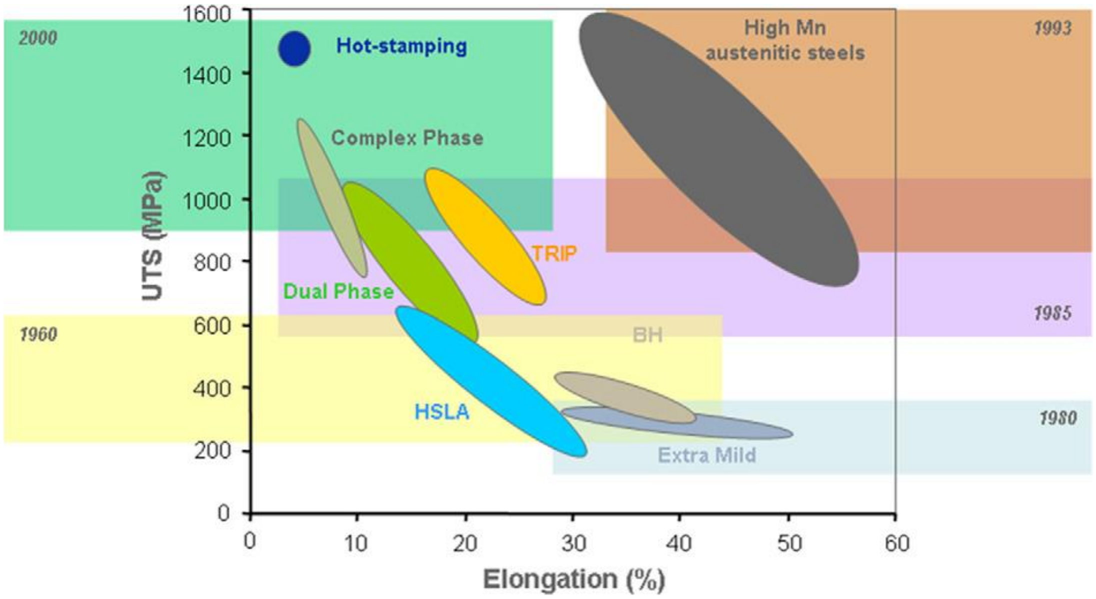

Fig. 1.1 Development of steels for structural applications in the automotive industry [1]

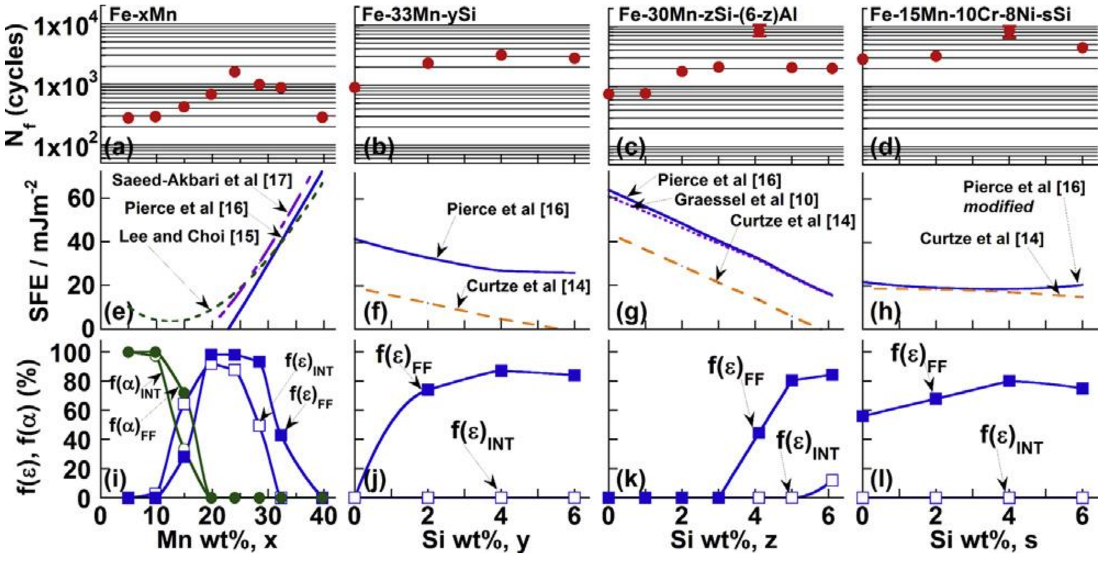

Fig. 1.2 SFE dependence on chemical composition of Si [7].

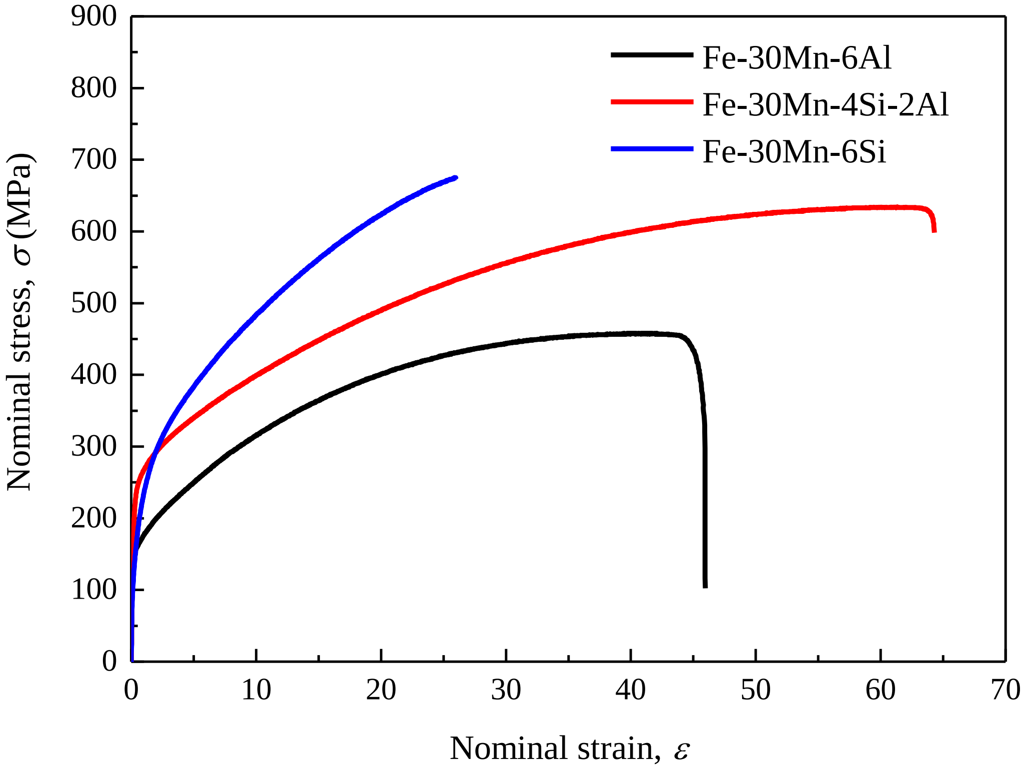

Fig. 1.3 Nominal stress- nominal strain curves of the Fe-30Mn-6Al, Fe-30Mn-4Si-2Al and Fe-30Mn-6Si alloys [20].

CHAPTER 2. Macroscopic observation of low cycle fatigue crack growth behavior associated with deformation-induced ε-martensitic transformation in high-Mn austenitic alloys

2.1 Introduction

In previous study, the Fe-30Mn-4Si-2Al alloy showed the short crack initiation life compared to the crack propagation life [1]. This indicates that the factor dominating the low-cycle fatigue properties is the low crack growth rate, which stems from the ε-martensite transformation. However, the effects of ε-martensitic transformation on the crack growth behavior have not yet been reported. In addition, it is still unclear why the Fe-30Mn-4Si-2Al alloy is the optimal composition.

Therefore, when considering fatigue-crack propagation, the crack-propagation path and effects of subcracks must be investigated. It has been reported that zigzag propagation paths reduce the fatigue-crack propagation rate and enhance roughness-induced crack closure [1, 2, 3]. Subcrack formation has two effects on propagation; it decreases the crack propagation rate because of the effects of crack toughening [4, 5], but it can also increase the crack propagation rate owing to the coalescing of the main crack with the subcracks [6, 7]. Moreover, by correlating these factors with microstructural features, it is expected that the mechanisms underlying the superior low-cycle fatigue behavior associated with ε-martensitic transformations can be understood.

In-situ observation is one of powerful method to investigate the fatigue crack growth behavior because the method facilitates direct observation of the fatigue crack growth from the crack initiation to crack propagation. Moreover, in-situ observation method has advantage of an immediate comparison between the fatigue crack growth rate and crack growth behavior. For instance, when the crack coalescence with subcrack occurs, the crack growth behavior and increased crack length can be observed at same time. In addition, the change of fatigue crack growth behavior can be investigated in the short and long crack regions through continuous observation during the fatigue test.

In this study, we observed the macroscopic fatigue-crack propagation and evolution of the microstructure in situ to clarify the characteristics of the propagation path and subcracks associated with ε-martensitic transformation. In addition, the crack growth behavior was observed at different crack lengths because the crack growth behavior can be changed due to increasing stress intensity factor. Thus, with the results of this study, the superior low-cycle performance of the Fe-30Mn-4Si-2Al alloy can be explained in terms of fatigue-crack growth.

2.2 Experimental procedures

The materials used in this study were Fe-30Mn-6Al, Fe-30Mn-4Si-2Al, and Fe-30Mn-6Si alloys. These alloys are dominated by different plastic deformation mechanisms during fatigue tests because of their different SFEs [8]. The alloys were forged and rolled at 1000 °C. The hot-rolled bars were then heat treated at 1000 °C for 1 h and subsequently water-quenched. The bars were cut via electric-discharge machining (EDM) to create the specimens for the bending fatigue test. The specimens were chemically polished with a solution of H_2O_2 and HF (ratio = 10:1, respectively) to remove the EDM-affected layer. The top surface of each specimen was then mechanically polished. Fig. 2.1 shows the geometry of the specimens used for the bending fatigue tests. A hole with a diameter (d) and height (h) of 100 μm was drilled in the center of the top surface of the specimens to control the crack initiation site. The surface was etched with a solution containing HNO_3 and C_2H_5OH (ratio = 1:9, respectively) to observe the evolution of the microstructure and its effects on crack propagation.

The bending fatigue tests were performed under fully reversed loading conditions at room temperature. The fatigue tests were conducted under an optical microscope with a total strain range of 0.7% and at a frequency of 6 Hz. The fatigue-crack length (l; see Fig. 1(d) for the definition of l) was directly measured from images obtained with the optical microscope. The fatigue tests were conducted until l reached 1 mm. After the bending fatigue tests, the specimens were mechanically polished to remove the deformation-induced topography. The microstructure at the crack tips was then observed via electron-backscatter diffraction (EBSD) measurements. All of the EBSD measurements were conducted with a beam step-size of 50 nm and an accelerating voltage of 20 kV. In addition, to observe the striations that arise from mode I fatigue-crack growth, additional specimens with drilled holes were fractured by fatigue under the same conditions as the in situ experiments. The fracture surfaces of these specimens were then observed via scanning electron microscopy (SEM) at an accelerating voltage of 15 kV.

2.3 Results

2.3.1 Fatigue crack growth rate

Fig. 2.2 shows l as a function of the number of cycles (N) for each alloy. The fatigue crack growth rates of the Fe-30Mn-6Al and Fe-30Mn-6Si alloys are comparable. Contrastingly, the fatigue crack growth rate of the Fe-30Mn-4Si-2Al alloy is markedly lower than that of the other alloys, which is similar to the trends reported in the literature [8, 9]. The sudden increase in the fatigue crack growth rate is due to the coalescence of the main crack with subcracks, as shown later. In Section 2.3.2, some characteristics of the fatigue crack growth behaviors of the three alloys are discussed by comparing the in situ images.

2.3.2 Fatigue crack growth behavior

2.3.2.1 Fe-30Mn-6Al alloy

Fig. 2.3 shows in situ images of the Fe-30Mn-6Al alloy during the fatigue test. A crack was initiated at the drilled hole after 2×10^3 cycles, and it subsequently propagated, as shown in Fig. 2.3(b). Fig. 2.3(c) shows that intensive surface reliefs are present at both the left- and right-hand side crack tips. Fig. 2.3(c-e) show that the propagation path of the left-hand side fatigue crack is a zigzag. In addition, subcracks were initiated at the grain boundaries, as indicated by the red arrows in Fig.

2.3(c) and (d). These subcracks eventually coalesce with the main fatigue crack (Fig. 2.3(f)), which accelerates the fatigue crack propagation rate (Fig. 2.2). To analyze the growth behavior of the zigzag crack (left-hand side crack), magnified images of the outlined region in Fig. 2.3(f) were obtained (Fig. 2.4). The propagation path can be decomposed into two directions; directions A and B, as indicated by the arrow in Fig. 2.4(f). Direction A is approximately perpendicular to the loading direction, but it does not contain any specific crystallographic features. The fatigue crack propagation in direction A is accompanied by the formation of slip traces along two slip planes. On the other hand, direction B is always along pre-existing slip traces, which indicates that direction B is along the $\{111\}_\gamma$ slip plane. The fatigue crack propagation stops at the grain boundary (Fig. 2.4(d)), but it then restarts, as shown in Fig. 2.4(e). The pre-existing slip traces are present even at 1.9×10^4 cycles (Fig. 2.4(a)), and the number of traces increases with the number of cycles until the main crack approaches the grain boundary, as shown in Fig. 2.4(b-d). By fatigue testing another Fe-30Mn-6Al specimen until it fractured, SEM images of the fracture surface were obtained, as shown in Fig. 2.4(g-i). Fig. 2.4(h) and (i) show that the early and late propagation regions mostly contain surface features with and without striations, respectively.

2.3.2.2 Fe-30Mn-4Si-2Al alloy

Fig. 2.5 shows in situ images of the Fe-30Mn-4Si-2Al alloy during the fatigue test. Fig. 2.5(b) shows that a considerable amount of deformation-induced plate-like products has formed. It has been reported that these plate-like products are mainly ε-martensite [8]. A subcrack was initiated at a grain boundary at 5.0×10^3 cycles, with the main crack initiated at 1.5×10^4 cycles, as shown in Fig. 2.5(b). The crack on the right-hand side reaches annealing twin boundaries, and then continues to propagate along the twin boundaries, as shown in Fig. 2.5(c) and (d). The fatigue crack branched to the perpendicular direction to the loading direction and then it is deflected again along the second annealing twin boundary (Fig. 2.5(e)); this deflection delayed the fatigue crack growth. After the crack passes through the annealing twin boundaries, the crack propagation occurs along a zigzag path (Fig. 2.5(f)). The zigzag propagation can be clearly seen in Fig. 2.6. Fig. 2.6(a) shows that a considerable amount of the plate-like products is present in front of the main crack tip. These plate-like products are ε-martensite, as shown by the phase map (Fig. 2.6(g)). By fatigue testing another Fe-30Mn-4Si-2Al specimen until it fractured, SEM image of the fracture surface were obtained, as shown in Fig. 2.6(i-k). Fig. 2.6(j) shows that the early propagation region exhibits a fracture surface without striation. Even though the fracture surface partially exhibits striation-like features (Fig. 2.6(k)), the distance between the striations (approximately 1-2 μm) corresponds to the spacing or thickness of the ε-martensite plates rather than the fatigue crack propagation rate. Even the late propagation region does not exhibit clear striation, and it contains features that are similar to those reported for tensile fractures that are associated with ε-martensitic transformation [10, 11].

2.3.2.3 Fe-30Mn-6Si alloy

Fig. 2.7 shows in situ images of the Fe-30Mn-6Si alloy during the fatigue test. Fig. 2.7(a) shows that before the fatigue test was performed, thermally induced ε-martensite was present. Crack initiation occurred at 6.0×10^3 cycles at the right-hand side of the drill hole, while a crack was initiated at the left-hand side of the drill hole at 1.3×10^4 cycles (Fig. 2.7(b)). However, the fatigue crack growth on the left-hand side is faster than that of the right-hand side (Fig. 2.7(c)). In addition, there is a considerable amount of thermally induced ε-martensite near the right-hand side crack tip, while the region around the left-hand side of the drill hole only exhibits a small amount. Fig. 2.7(d) shows that the crack growth on the right-hand side creates a zigzag propagation path. Moreover, a subcrack then forms and coalesces with the main crack (Fig. 2.7(e) and (f)). To understand this crack growth behavior, magnified images of the zigzag region were obtained (Fig. 2.8). Fig. 2.8(a) shows the formation of a subcrack near the main crack tip. The main crack then coalesces with the subcrack, which accelerates the fatigue crack growth (Fig. 2.8(b)); this is similar to the coalescence observed in Fig. 2.7(f). Furthermore, Fig. 2.8(c-f) show that the coalescence of the main crack with subcracks occurs repeatedly. As has been described in Sections 2.3.2.1 and 2.3.2.2, the fracture surface of a different specimen composed of the same alloy was observed via SEM (Fig. 2.8(g-i)). In contrast to the other alloys, Fig. 2.8(h) shows that a considerable number of secondary cracks are present on the fracture surface, as indicated by the arrows. Fig. 2.8(i) shows that these secondary cracks and steps become clearer as *l* increases. Moreover, the red broken like in Fig. 2.8(i) indicates the presence of a pyramidal surface feature.

2.3.3 Microstructural features at the crack tips

Fig. 2.9 shows the results of the EBSD measurements performed around the fatigue crack tip in the Fe-30Mn-6Al alloy after the fatigue test was completed. The phase map shown in Fig. 2.9(b) indicates that no ε-martensite has formed near the crack tip. In addition, the image quality (IQ) map (Fig. 2.9(c)) does not indicate the presence of plates, which indicate that neither thin mechanical twin plates nor ε-martensite formed during this fatigue test. Furthermore, the $\{111\}_\gamma$ plane traces have been highlighted in the IQ map, which indicate that the majority of the fatigue crack growths along the $\{111\}_\gamma$ planes.

Fig. 2.10 shows the results of the EBSD measurements performed around the fatigue crack tip in the Fe-30Mn-4Si-2Al alloy after the fatigue test was completed. Fig. 2.10(b) shows that deformation-induced ε-martensitic transformation have occurred near the fatigue crack tip. In addition, the fatigue crack has propagated along γ/ε-interfaces when the propagation path is aligned with the $\{111\}_\gamma$ planes.

Fig. 2.11 shows the results of the EBSD measurements performed around the fatigue crack tip in the Fe-30Mn-6Si alloy after the fatigue test was completed. Fig. 2.11(b) shows that a considerable amount of ε-martensite plates can be clearly seen in the IQ image (Fig. 2.11(c)). The majority of the fatigue crack along the $\{111\}_\gamma$ planes, which most likely corresponds to the γ/ε-interfaces, as discussed in Section 2.4.1.

2.3.4 Crack opening and closing processes during one cycle

Fig. 2.12(a-i) show the crack opening and closing processes in the Fe-30Mn-4Si-2Al alloy during one cycle. Here, the both main and subcracks are present in the images. The plates observed around the cracks are ε-martensite, as shown by the phase and IQ maps (Fig. 2.12(j) and (k), respectively). A considerable number of subcracks are present along the γ/ε-interfaces, as shown in Fig. 2.5 and 2.12. In addition, these subcracks are often aligned parallel to the main crack. Furthermore, the subcracks usually grow until a critical length is achieved, which corresponding to approximately the grain size. Fig. 2.12(a-i) shows that the main crack and subcracks open and close simultaneously.

2.4 Discussion

2.4.1 Crack propagation path along the $\{111\}_\gamma$ planes; similar behaviors produced by different underlying mechanisms

The fatigue cracks of the three alloys investigated in this study mainly propagated along the $\{111\}_\gamma$ planes. That is, the fatigue crack propagation paths look similar regardless of the composition. However, when studied in detail, the underlying propagation mechanisms in the three alloys are extremely different. The Fe-30Mn-6Al alloy exhibited neither mechanical twins nor ε-martensite, as shown in Fig. 2.9. Therefore, the fatigue crack propagation along the $\{111\}_\gamma$ planes is believed to stem from slip localization. Dislocation planar slip and the resulting persistent Lüders banding (PLB) are the most likely candidates for the fatigue propagation mechanisms in the Fe-30Mn-6Al alloy [12, 13]. Even though the SFE of the Fe-30Mn-6Al alloy is relatively high compared to that of the other alloys, the SFE divided by the shear modulus is approximately 0.9 mJ/(m^2 ·GPa) (Shear modulus = 65 GPa [24]. SFE = 60 mJ/m^2 [9]). This value is lower than that of other face-centered cubic (FCC) alloys, such as pure Cu (approximately 1.6 mJ/(m^2 ·GPa) [15]), which exhibits frequent cross slips that result in persistent slip banding [16]. Accordingly, a low SFE is believed to promote intensive planar dislocation slip, which causes plastic strain localization (i.e., PLB) [12, 13]. In addition, PLB has been reported to initiate fatigue cracks [13, 16]. Therefore, because PLB forms along the slip plane, the fatigue crack in an FCC alloy with a relatively low SFE propagates along the $\{111\}_\gamma$ planes. The zigzag fatigue crack growth shown in Fig. 2.4 is the result of a combination of fatigue phenomena: PLB and conventional mode I propagation that is accompanied by the formation of slip traces on different slip planes, as shown in Fig. 2.4. In addition, the conventional mode I propagation can be explained with a blunting and re-sharpening mechanism. The blunting/re-sharpening and PLB mechanisms correspond to the crack propagation along the A and B directions, respectively. Furthermore, the blunting/re-sharpening and PLB processes are accompanied by striation and brittle-like features, respectively. According to the fractographic analysis (Fig. 2.4(g-i)), the early and late fatigue crack propagation behaviors are dominated by the PLB and blunting/re-sharpening behaviors are dominated by the PLB and blunting/re-sharpening mechanisms, respectively. The zigzag propagation that stems from the combination of these mechanisms is believed to be an intermediate fatigue crack propagation behavior. One possible reason for the change in the propagation mechanism is the difference between the number of dislocations emitted from the crack tips of short and long fatigue cracks. When numerous emitted dislocations pile up around the crack tip during a single cycle, cross slip occurs to accommodate the back stress. Accordingly, the strain distribution is relatively homogenous, which assists the occurrence of the typical mode I fatigue crack propagation.

In contrast, when the fatigue crack growth path lies along the $\{111\}_\gamma$ planes in the Fe-30Mn-4Si-2Al and Fe-30Mn-6Si alloys, the mechanism that causes the crack propagation is the formation of ε-martensite. When a crack propagates along the $\{111\}_\gamma$ planes, the γ/ε-interface can be considered the crack propagation path because the γ/ε-interface always satisfies the Shoji-Nishiyama relationship [17]. The γ/ε-interface can be the preferred fatigue crack propagation path because of the two following factors. The first factor is the low resistance against brittle-like cracking on the γ/ε-interface [11, 18]. This is because a $\{111\}_\gamma$ plane is parallel to the basal plane of ε-martensite, and therefore, the dislocation motions of the other $\{111\}_\gamma$ planes are strongly inhibited at the γ/ε-interface. Thus, the stress concentration at the γ/ε-interface causes brittle-like cracking. The second factor is the reversible motion of leading partial dislocations on the γ/ε-interface [19, 20]. It has been reported that ε-martensite grows through leading dislocation motions on every other $\{111\}_\gamma$ plane. Therefore, because the ε-martensite in Fe-30Mn-Si-based alloys exhibits shape-memory effect-like deformation-induced reverse transformation [19, 20], the reverse transformation mostly occurs via the reverse motion of leading partial dislocations. Thus, as long as reversible ε-martensitic transformation can occur effectively, the dislocation motions are activated mainly on the γ/ε-interface. During the reversible dislocation motions, irreversible lattice defects, such as residual dislocations that are due to the forward/reverse transformations, might from, which causes the fatigue crack propagation at the γ/ε-interface. Moreover, as shown in Fig. 2.11, there is a considerable number of intersecting ε-martensite domains in the Fe-30Mn-6Si alloy. As has been reported for Fe-Mn-Si-based shape memory alloys, this intersection requires the formation of complex microstructures, such as FCC phases and hexagonal close-packed (HCP) twins [21-23], which may reduce the reversibility of the deformation-induced transformation. Therefore, the irreversibility of these intersections could also be a reason for the preferential formation of fatigue damage at ε-martensite plates during low cycle fatigue. The resulting $\{111\}_\gamma$ fatigue crack propagation is a cause of the formation of striation-free features on the fracture surface (Fig. 2.6(j) and 2.8(h)). If a considerable amount of ε-martensite plates is activated on multiple slip planes, the smoothness of the fatigue crack propagation is disturbed at the γ/ε-interfaces, which results in the striation-like features (Fig. 2.6(k)) with a spacing that corresponds to the spacing or thickness of the ε-martensite plates.

In addition, fatigue crack propagation along annealing twin boundaries in a $\{111\}_\gamma$ plane was also observed (Fig. 2.6). The fatigue crack growth behavior shown in Fig. 2.6 indicates both the positive and negative effects of annealing twin boundaries on the resistance against fatigue crack growth. First, the fatigue crack impinged on the annealing twin boundary. Then, the fatigue crack propagated along the same twin boundary. The former indicates that twin boundaries that are aligned perpendicular to the crack propagation direction can inhibit crack growth, while the latter implies that the twin boundary is a preferred site for the accumulation of fatigue damage. Σ3 coherent twin boundaries have been reported to act as string obstacles against dislocation motions. This is because a large amount of energy is required for dislocation dissociation to occur at twin boundaries [24, 25]. The dislocation dissociation is indispensably needed for the dislocation to penetrate the coherent boundary [26, 27], inhibiting the further dislocation motions at the twin boundary. This property of twin boundaries contributes to the prevention of fatigue crack growth. In contrast, the ease with which fatigue cracks are initiated at twin boundaries has also been reported by previous studies [24, 28-30]. Specifically, it has been reported that intersections between slip bands and twin boundaries act as the initiation sites for cracks [28]. The fatigue damage-induced initiation of cracks is believed to occur through the accumulation of irreversible lattice defects on the twin boundary. As mentioned in Section 2.4.1, dislocation penetration across a coherent twin boundary requires dislocation dissociation. The dislocation dissociation results in an irreversible dislocation. For example, a dislocation dissociation at a twin boundary can be expressed by the reaction shown in Eq. (1) [26]:

$$\frac{1}{2}[\bar{1}01](111)11\frac{1}{6}[\bar{1}14](\overline{511}) + \frac{1}{6}[\overline{211}](\bar{1}11) \qquad (1)$$

where $[\bar{1}01](111)$ represents the incident dislocation and the $(\bar{1}11)$ plane is the obstacle twin boundary. The slip plane and direction can be expressed by indices in the matrix. That is, (1/6) $[\bar{1}14](\overline{511})$ corresponds to a perfect dislocation at the twin boundary. Fig. 2.13 shows a schematic diagram for the various interactions between the dislocation and coherent twin boundary. A (1/6) $[\overline{211}](\bar{1}11)$ dislocation is generated when the incident dislocation passes through the $(\bar{1}11)$ twin boundary. Even when a (1/6) $[\bar{1}14](\overline{511})$ dislocation completes the reverse motion during the compression process of the fatigue, the dislocation dissociation for the dislocation penetration across the twin boundary in the reverse motion requires another dislocation that corresponds to a (1/6) $[\overline{211}](\bar{1}11)$ dislocation during the tension process. Therefore, irreversible dislocations are accumulated through the repetition of dislocation dissociations at the twin boundary, which results in the fatigue damage-induced formation of crack at the twin boundary.

2.4.2 Effects of subcracks: coalescence and crack toughening

In addition to the growth of the main crack, subcracks formed during the fatigue tests, especially in the Fe-30Mn-4Si-2Al and Fe-30Mn-6Si alloys. The formation of subcracks has two effects on fatigue crack growth: coalescence with the main crack and crack toughening. The former and latter accelerates and decelerates fatigue crack growth, respectively. The formation of subcracks near the tip of the main crack was common in the Fe-30Mn-6Si alloy. Therefore, because the propagation proceeds via the repeated coalescence of the main crack was common in the Fe-30Mn-6Si alloy. Therefore, because the propagation proceeds via the repeated coalescence of the main crack with the subcracks, the fatigue crack propagation of the Fe-30Mn-6Si alloy was discontinuous. As a result of this coalescence, secondary cracks and steps appeared in the fracture surface of this alloy, as shown in Fig. 2.8(h) and (i). Furthermore, the pyramidal surface feature in Fig. 2.8(i) can also be explained by either coalescence or propagation along three different $\{111\}_\gamma$ planes.

On the other hand, the coplanar subcracks of the Fe-30Mn-4Si-2Al alloy did not appear near the tip of the main crack. Instead, the subcracks formed beside the main crack, as shown in Fig. 2.12. The subcracks beside the main crack can decelerate the fatigue crack growth through two processes. The first process is stress redistribution, which occurs because of the release of residual stress at a crack tip during subcrack initiation and propagation [4]. This behavior enhances the resistance against the fatigue crack propagation of the main crack through a crack tip shielding mechanism [5]. The second process is a reduction in the crack tip opening displacement (CTOD), which arises from the opening of subcracks, such as the one shown in Fig. 2.12. Therefore, because the fatigue tests performed in this study were strain-controlled, the CTOD of the main crack at the maximum strain decreases when non-coplanar subcracks of significant length are present. As we proposed in our previous study [1], these microscopic changes in fatigue can be classified into two cases: crack propagation-induced events and macroscopic deformation-induced events. The latter does not depend on when the main crack initiation and propagation occurs. Thus, the most important factor controlling the fatigue crack growth of the Fe-30Mn-4Si-2Al alloy is the crack propagation-induced event. The effects of stress redistribution can be categorized as crack propagation-induced event. On the other hand, a reduction in the CTOD can be categorized as a macroscopic deformation-induced event, which indicates that the reduction of the CTOD is a minor factor in the deceleration of crack growth under the conditions of this study. However, the contribution from the reduction of the CTOD can be enhanced by greatly increasing the number of subcracks. Therefore, reducing the CTOD may significantly contribute to the deceleration of crack growth when under extreme conditions that cause the formation of many subcracks.

2.4.3 Factors affecting fatigue crack growth: why does the Fe-30Mn-4Si-2Al alloy show the outstanding fatigue resistance?

From the viewpoint of microstructural evolution, the deformation-induced ε-martensitic transformation plays an important role in fatigue crack growth. The effects of the chemical composition on the phase stability are the most crucial factors because it will affect the behaviors of both the forward and reverse transformation. The stability of the austenite phase to ε-phase of in the Fe-30Mn-4Si-2Al alloy is lower than that of the Fe-30Mn-6Al alloy, which allows the ε-martensitic transformation to occur, but it is higher than that of the Fe-30Mn-6Si alloy, which facilities the deformation-induced reverse transformation at room temperature. In addition to the thermodynamic effect, the two effects of ε-martensitic transformation on fatigue crack growth must be considered: the promotion of fatigue crack formation on γ/ε-interface and the suppression of slip-related strain localization at the crack tip. The promotion of fatigue crack formation has both positive and negative effects on fatigue crack growth. The negative effect is the coalescence with the main crack, which accelerates fatigue crack growth. The positive effect is the crack toughening, which is associated with crack tip shielding and a reduction in the CTOD at the maximum strain during a cycle. Moreover, the evolution of γ/ε-interface fatigue damage produces a zigzag fatigue crack propagation path along the $\{111\}_{\gamma}$ plane, which assists the roughness-induced crack closure [2, 3]. The suppression of slip related strain localization is attributed to the reversible motion of leading partial dislocations, which inhibits PLB that stems from the accumulation of irreversible lattice defects. Therefore, because PLB causes fatigue damage evolution, its suppression decelerates fatigue crack growth.

In this context, the behavior of ε-martensitic transformation must be controlled to achieve an exceptional resistance against low cycle fatigue crack growth, such as that exhibited by the Fe-30Mn-4Si-2Al alloy (Fig. 2.2). For example, the Fe-30Mn-6Al alloy contains no ε-martensite, and hence, it does not receive the positive effects of ε-martensite, which results in the lower resistance against fatigue compared to the Fe-30Mn-4Si-2Al alloy. In contrast, in the case of the Fe-30Mn-6Si alloy, a considerable number of subcracks preferentially formed near the crack tip, which promoted fatigue crack growth by coalescing with the main crack. The ease with which the subcracks formed is probably because of the higher amount of ε-martensite. The high amount of ε-martensite increases the degree of stress concentration and decreases the reversibility because of intersections of ε-martensite plates. Furthermore, the addition of Si is known to have a significant effect to deteriorate the plasticity of steels [31]. The reduction in plasticity potentially causes the γ/ε-interface to crack more easily. The brittle features of ε-martensite-related cracks can be clearly observed in tensile tests when more than 6% of Si is added to Fe-high-Mn alloys [11].

2.5 Conclusions

In this study, the microstructural evolution of Fe-30Mn-6Al, Fe-30Mn-4Si-2Al, and Fe-30Mn-6Si alloys during strain-controlled bending fatigue tests was observed in situ. From the results, the factors that produce the superior resistance of the Fe-30Mn-4Si-2Al alloy against low cycle fatigue were determined in terms of the crack propagation behavior. The main conclusions are summarized below.

(1) The Fe-30Mn-6Al alloy exhibited fatigue crack growth along the $\{111\}_\gamma$ plane in addition to conventional mode I propagation. The fatigue crack propagation along the $\{111\}_\gamma$ plane is caused by the strain localization and the subsequent fatigue crack formation.

(2) The Fe-30Mn-4Si-2Al and Fe-30Mn-6Si alloys also exhibited fatigue-crack growth along the $\{111\}_\gamma$ plane. However, the propagation mechanisms involved are not the same as that of the Fe-30Mn-6Al alloy. That is, the fatigue cracks in the Fe-30Mn-4Si-2Al and Fe-30Mn-6Si alloys propagated along the γ/ε-interfaces. The fatigue crack propagation along the γ/ε-interfaces causes the formation of a zigzag propagation path. The zigzag propagation path is believed to decelerate fatigue crack growth because of the enhanced roughness-induced crack closure.

(3) Subcracks that formed near the crack tip coalesced with the main crack, which accelerated crack growth in the Fe-30Mn-6Si alloy. In contrast, the subcracks in the Fe-30Mn-4Si-2Al alloy did not coalesce with the main crack. This is

believed to decelerate fatigue crack growth because of the stress redistribution and a reduction in the CTOD, which stem from the opening of subcracks.

Hence, in terms of crack growth, the ε-martensitic transformation has three positive effects: 1) the suppression of strain localization; 2) zigzag crack propagation, which enhances roughness-induced crack closure; and 3) subcrack formation, which induces crack-toughening, such as the stress redistribution. However, the ε-martensitic transformation also has a negative effect on crack growth, i.e., it causes subcrack initiation, which leads to the subcrack coalescence with the main crack. The ε-martensitic transformation in the Fe-30Mn-4Si-2Al alloy is optimized so that the three positive effects are maximized while the negative effect is minimized, which results in the superior resistance of the alloy against low cycle fatigue. In future works, the optimal plasticity, amount (phase stability), and morphology of ε-martensite must be determined, and its associated subcrack formation behavior that assists crack toughening and roughness-induced crack closure without coalescence with the main crack should be investigated further.

References

[1] H. Li, M. Koyama, T. Sawaguchi, K. Tsuzaki, H. Noguchi, Importance of crack propagation-induced ε-martensite in strain-controlled low-cycle fatigue of high-Mn austenitic steel, Phill. Mag. Lett. 95 (2015) 303-311.

[2] G. Gray, J. Williams, A. Thompson, Roughness-induced crack closure: an explanation for microstructurally sensitive fatigue crack growth, Metall. Trans. A 14 (1983) 421-433.

[3] R. Ritchie, S. Suresh, Some considerations on fatigue crack closure at near threshold stress intensities due to fracture surface morphology, Metall. Trans. A 13 (1982) 937-940.

[4] D.K.M. Shum, J.W. Hutchinson, On toughening by microcracks, Mech. Mater. 9 (1990) 83-91.

[5] R.O. Ritchie, workshop on the mechanics and physics of crack growth: application to life prediction mechanisms of fatigue crack propagation in metals, ceramics and composites: role of crack tip shielding, Mater. Sci. Eng. A 103 (1988) 15-28.

[6] K. Le Biavant, S. Pommier, C. Prioul, Local texture and fatigue crack initiation in a Ti-6Al-4V titanium alloy, Fatigue Fract. Eng. Mater. Struct. 25 (2002) 527-545.

[7] T. Sawaguchi, I. Nikulin, K. Ogawa, K. Sekido

[8] Z.-J. Xi, M. Koyama, Y. Yoshida, N. Yoshimura, K. Ushioda, H. Noguchi, Effects of cementite morphology on short-fatigue-crack propagation in binary Fe-

C steel, Phill. Mag. Lett. (2015) 1-8.

[9] I. Nikulin, T. Sawaguchi, K. Tsuzaki, Effect of alloying composition on low-cycle fatigue properties and microstructure of Fe-30Mn-(6-x)Si-xAl TRIP/TWIP alloys, Mater. Sci. Eng. A 587 (2013) 192-200.

[10] T. Sawaguchi, I. Nikulin, K. Ogawa, K. Sekido, S. Takamori, T. Maruyama, Y. Chiba, A. Kushibe, Y. Inoue, K. Tsuzaki, Designing Fe-Mn-Si alloys with improved low-cycle fatigue lives, Scr. Mater. 99 (2015) 49-52.

[11] Y.S. Chun, J.S. Kim, K.-T. Park, Y.-K. Lee, C.S. Lee, Role of 3 martensite in tensile properties and hydrogen degradation of high-Mn steels, Mater. Sci. Eng. A 533 (2012) 87-95.

[12] M. Koyama, T. Sawaguchi, K. Tsuzaki, Effects of Si on tensile properties associated with deformation-induced ε-martensitic transformation in high Mn austenitic alloys, Mater. Trans. 56 (2015) 819-825.

[13] L. Buchinger, A.S. Cheng, S. Stanzl, C. Laird, The cyclic stress-strain response and dislocation structures of Cu-16 at.% Al alloy III: single crystals fatigued at low strain amplitudes, Mater. Sci. Eng. 80 (1986) 155-167.

[14] S.I. Hong, C. Laird, Fatigue crack initiation and growth behavior of Cu-16 at.% a1 single crystals, Fatigue Fract. Eng. Mater. Struct. 14 (1991) 143-169.

[15] S. Allain, J.P. Chateau, O. Bouaziz, A physical model of the twinning-induced plasticity effect in a high manganese austenitic steel, Mater. Sci. Eng. A 387-389 (2004) 143-147.

[16] Y.H. Zhao, Z. Horita, T.G. Langdon, Y.T. Zhu, Evolution of defect structures during cold rolling of ultrafine-grained Cu and Cu-Zn alloys: influence of stacking fault energy, Mater. Sci. Eng. A 474 (2008) 342-347.

[17] P. Lukáš, L. Kunz, Cyclic slip localisation and fatigue crack initiation in fcc single crystals, Mater. Sci. Eng. A 314 (2001) 75-80.

[18] Z. Nishiyama, Martensitic Transformation, Elsevier, 2012.

[19] S. Takaki, T. Furuya, Y. Tokunaga, Effect of Si and Al additions on the low temperature toughness and fracture mode of Fe-27Mn alloys, ISIJ Int. 30 (1990) 632-638.

[20] T. Sawaguchi, P. Sahu, T. Kikuchi, K. Ogawa, S. Kajiwara, A. Kushibe, M. Higashino, T. Ogawa, Vibration mitigation by the reversible fcc/hcp martensitic transformation during cyclic tension-compression loading of an Fe-Mn-Si-based shape memory alloy, Scr. Mater. 54 (2006) 1885-1890.

[21] T. Sawaguchi, L.G. Bujoreanu, T. Kikuchi, K. Ogawa, M. Koyama, M. Murakami, Mechanism of reversible transformation-induced plasticity of Fe-Mn-Si shape memory alloys, Scr. Mater. 59 (2008) 826-829.

[22] J.H. Yang, C.M. Wayman, Development of Fe-based shape memory alloys associated with face-centered cubic-hexagonal close-packed martensitic transformations: part III. microstructures, Metall. Trans. A 23 (1992) 1445-1454.

[23] S. Matsumoto, A. Sato, T. Mori, Formation of h.c.p. and f.c.c. twins in an Fe·Mn·Cr·Si·Ni alloy, Acta Metall. 42 (1994) 1207-1213.

[24] X. Zhang, T. Sawaguchi, K. Ogawa, F. Yin, X. Zhao, A structure created by intersecting ε martensite variant plates in a high-manganese steel, Phil. Mag. Lett. 91 (2011) 4410-4426.

[25] L. Rémy, The interaction between slip and twinning systems and the influence of twinning on the mechanical behavior of fcc metals and alloys, Metall. Trans. A 12 (1981) 387-408.

[26] M.D. Sangid, T. Ezaz, H. Sehitoglu, I.M. Robertson, Energy of slip transmission and nucleation at grain boundaries, Acta Mater. 59 (2011) 283-296.

[27] S. Mahajan, G.Y. Chin, Twin-slip, twin-twin and slip-twin interactions in Co-8 wt.% Fe alloy single crystals, Acta Metall. 21 (1973) 173-179.

[28] L. Rémy, Twin-slip interaction in f.c.c. crystals, Acta Metall. 25 (1977) 711-714.

[29] A.S. Hamada, L.P. Karjalainen, J. Puustinen, Fatigue behavior of high-Mn TWIP steels, Mater. Sci. Eng. A 517 (2009) 68-77.

[30] S. Qu, P. Zhang, S.D. Wu, Q.S. Zang, Z.F. Zhang, Twin boundaries: strong or weak? Scr. Mater. 59 (2008) 1131-1134.

[31] Z.J. Zhang, P. Zhang, L.L. Li, Z.F. Zhang, Fatigue cracking at twin boundaries: effects of crystallographic orientation and stacking fault energy, Acta Mater. 60 (2012) 3113-3127.

[32] W.W. Gerberich, Y.T. Chen, D.G. Atteridge, T. Johnson, Plastic flow of Fe binary alloys-II. Application of the description to the ductile-brittle transition, Acta Metall. 29 (1981) 1187-1201.

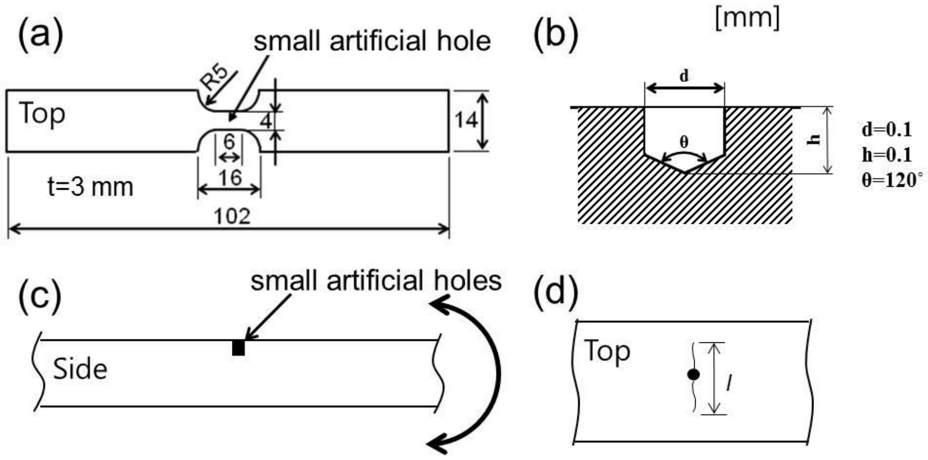

Fig. 2.1 (a) Top view of the sample geometry used for the fatigue tests. (b) Detailed schematic of the shape of the drilled hole that is indicated in (a) (d = diameter, h = height). (c) Magnified side view showing the position of the drill hole and the loading direction. (d) Definition of the crack length (*l*) that was used in this study.

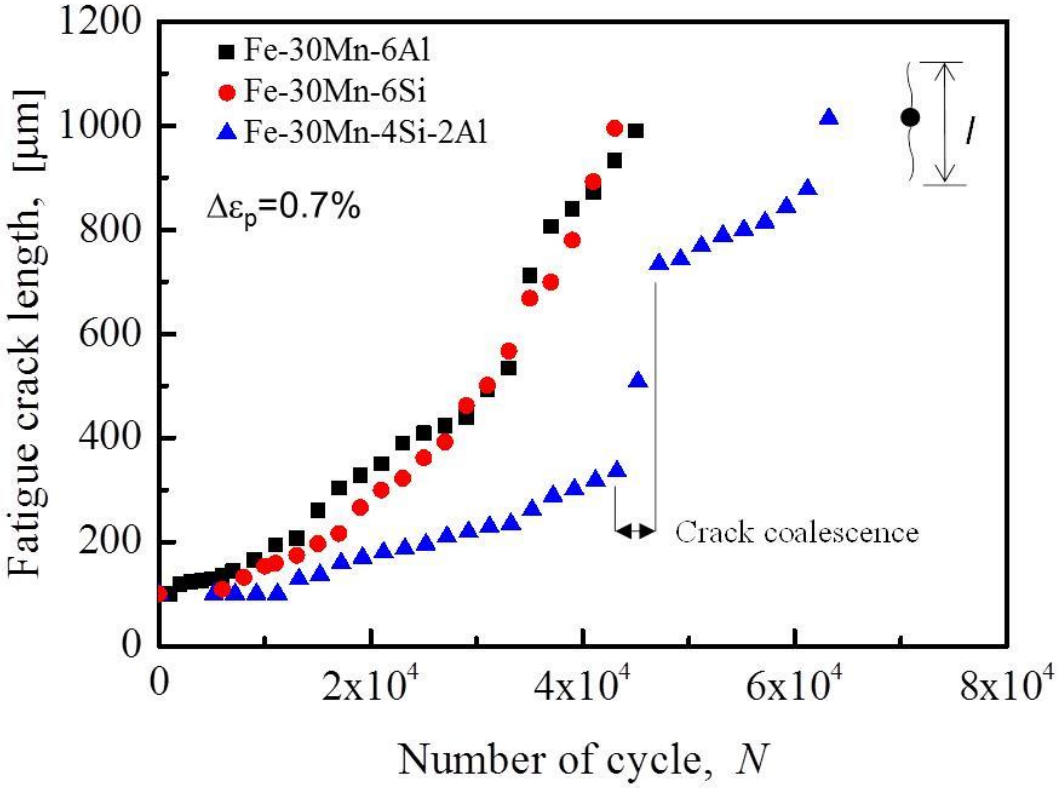

Fig. 2.2 Fatigue crack length (*l*) as a function of the number of cycles (*N*) for a maximum *l* of 1 mm for the three alloys tested.

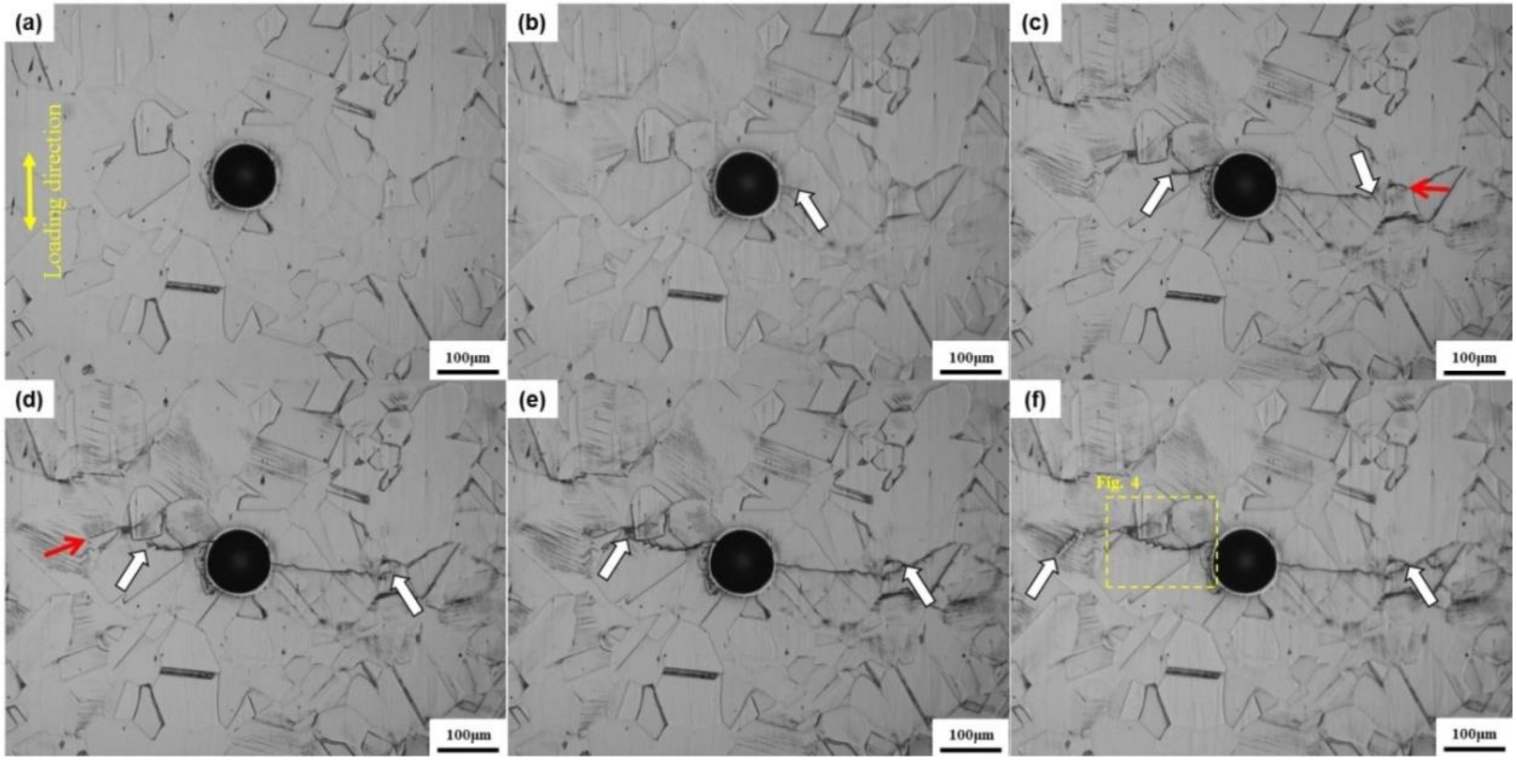

Fig. 2.3 In situ images of the Fe-30Mn-6Al alloy at various points during the fatigue test: (a) undeformed, (b) 6.0 × 10^3, (c) 1.9 × 10^4, (d) 2.3 × 10^4, (e) 2.9 × 10^4, and (f) 3.3 × 10^4 cycles. The white arrows indicate the main crack tips. The red arrows indicate subcracks.

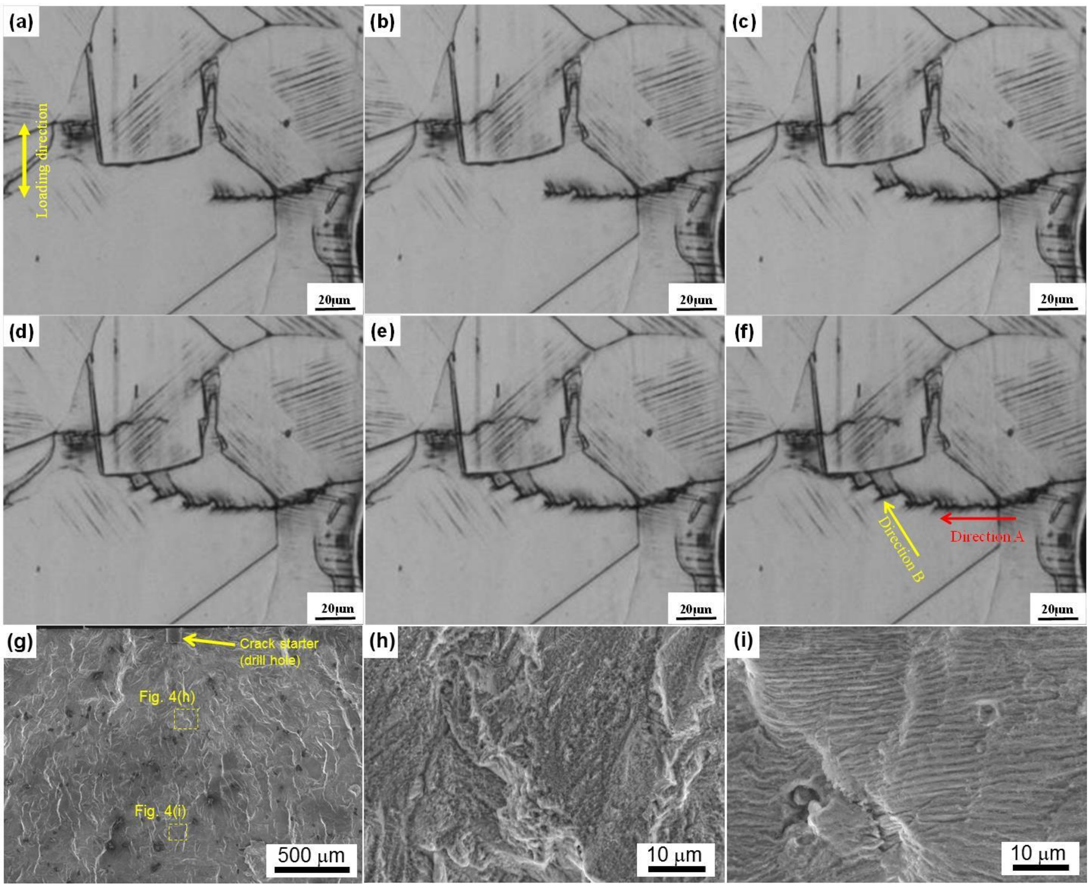

Fig. 2.4 (a-f) In situ images of the Fe-30Mn-6Al alloy at various points during the fatigue test: (a) 1.9×10^4, (b) 2.1×10^4, (c) 2.3×10^4, (d) 2.5×10^4, (e) 2.7×10^4, and (f) 2.9×10^4 cycles. (g-i) SEM images of the fatigue fracture surface of the same alloy (but a different specimen): (g) overview, and (h) early and (i) late propagation regions.

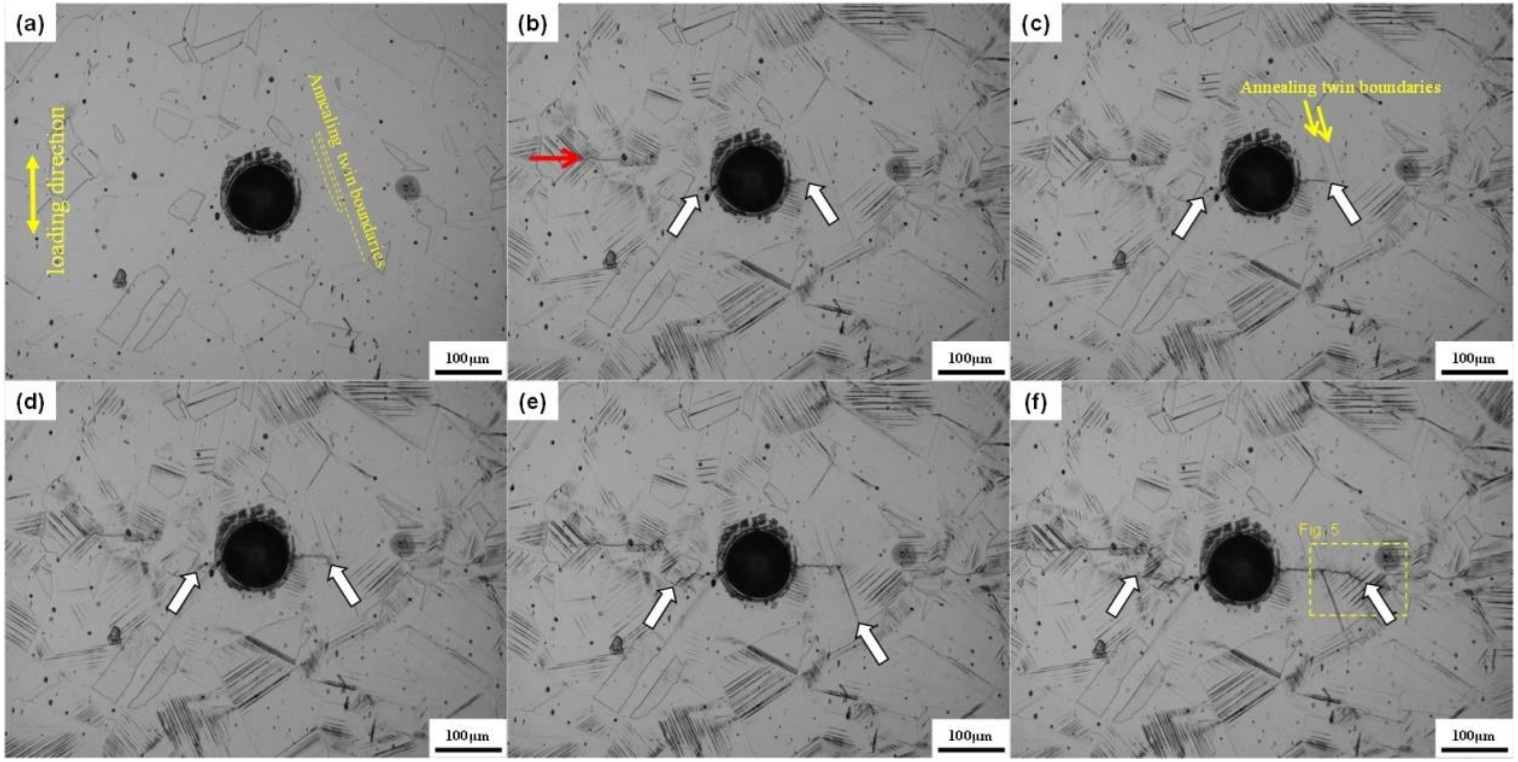

Fig. 2.5 In situ images of the Fe-30Mn-4Si-2Al alloy at various points during the fatigue test: (a) undeformed, (b) 1.9 × 10^4, (c) 2.1 × 10^4, (d) 2.5 × 10^4, (e) 3.3 × 10^4, and (f) 4.3 × 10^4 cycles. The white arrows indicate the main crack tips. The broken yellow lines indicate annealing twin boundaries. The red arrow indicates a subcrack.

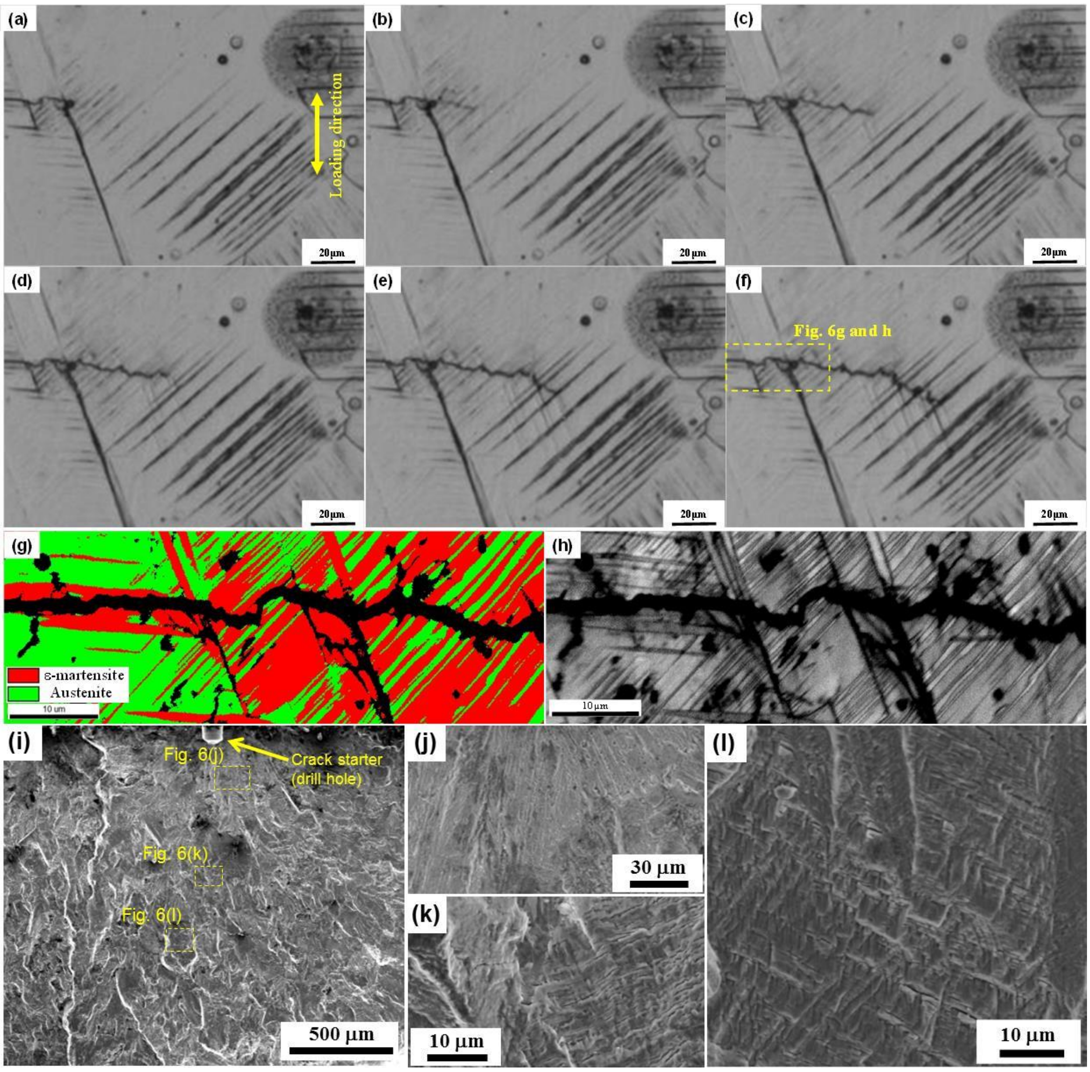

Fig. 2.6 (a-f) In-situ images of the Fe-30Mn-4Si-2Al alloy at various points during the fatigue test: (a) 3.1 × 10^4 cycles, (b) 3.5 × 10^4 cycles, (c) 3.7 × 10^4 cycles, (d) 3.9 × 10^4 cycles, (e) 4.1 × 10^4 cycles, and (f) 4.3 × 10^4 cycles. (g) Phase and (h) image quality maps corresponding to the outlined region in (f). (i-l) SEM images of the fatigue fracture surface of the same alloy (but a different specimen): (i) overview, and (j) early, (k) intermediate, and (l) late propagation regions.

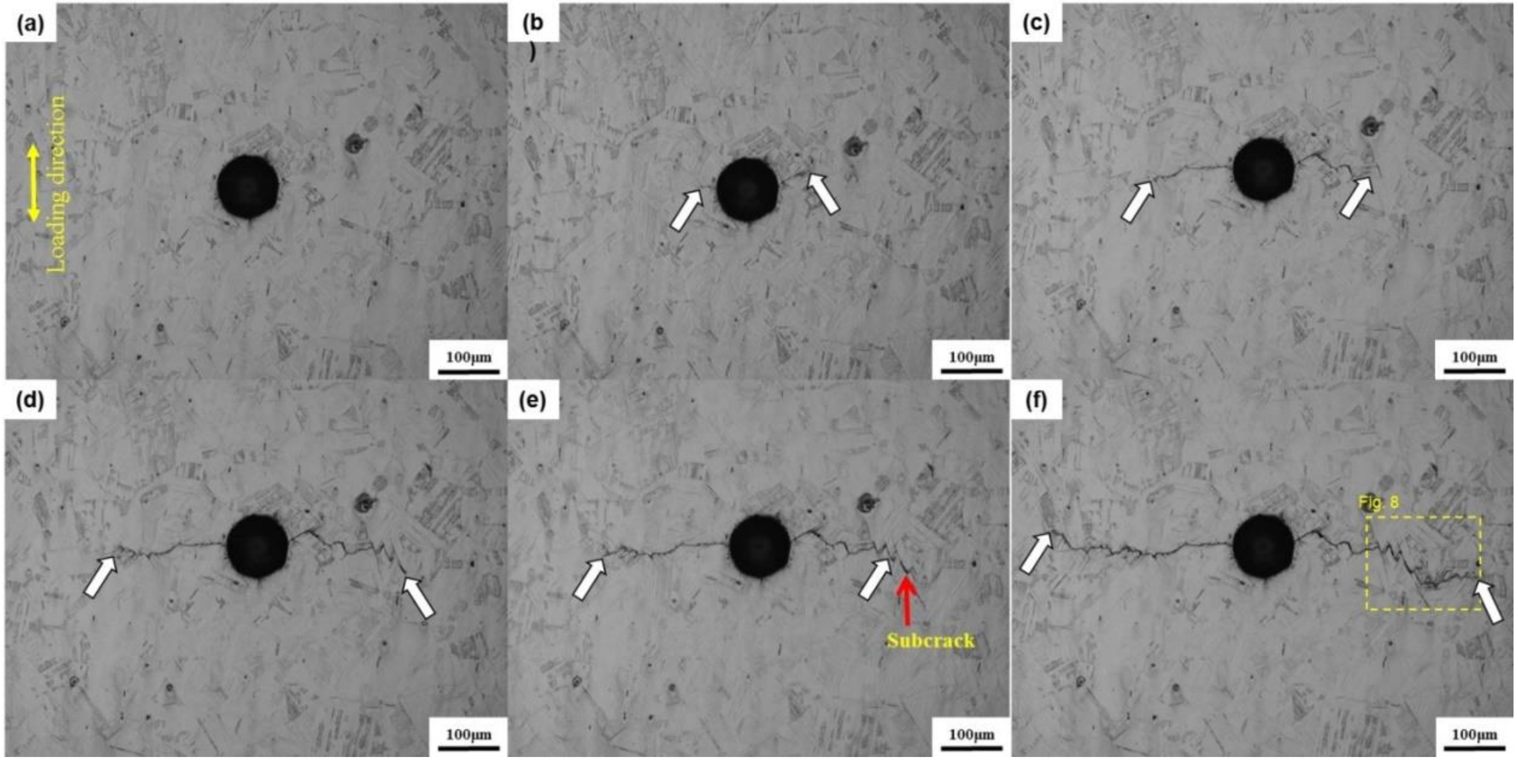

Fig. 2.7 In situ images of the Fe-30Mn-6Si alloy at various points during the fatigue test: (a) undeformed, (b) 1.3 × 10^4, (c) 2.5 × 10^4, (d) 2.9 × 10^4, (e) 3.1 × 10^4, and (f) 3.7 × 10^4 cycles. The white arrows indicated the main crack tips. The red arrows indicate subcracks.

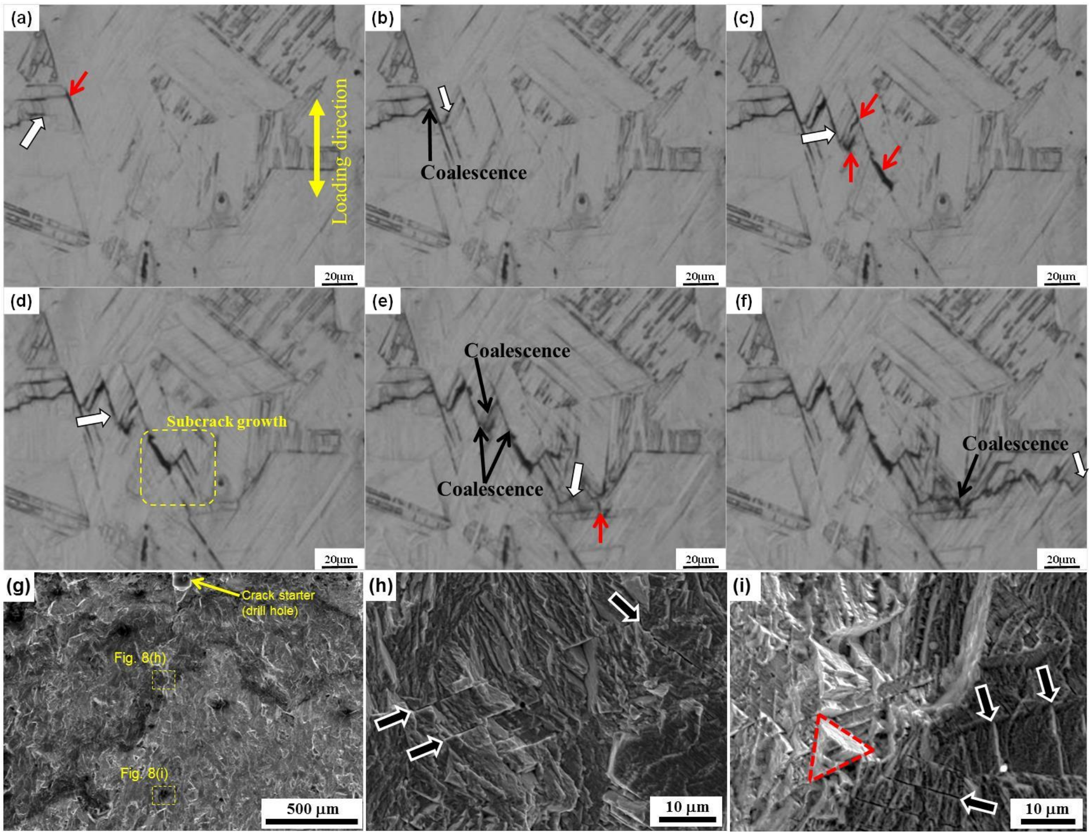

Fig. 2.8 (a-f) In situ images of the Fe-30Mn-6Si alloy at various points during the fatigue test: (a) 2.5 × 10^4 cycles, (b) 2.7 × 10^4 cycles, (c) 2.9 × 10^4 cycles, (d) 3.1 × 10^4 cycles, (e) 3.3 × 10^4 cycles, and (f) 3.5 × 10^4 cycles. The white arrows indicate the main crack, while the red arrows indicate the subcracks. (g-i) SEM images of the fatigue fracture surface of the same alloy (but a different specimen): (g) overview, and (h) early and (i) late propagation regions.

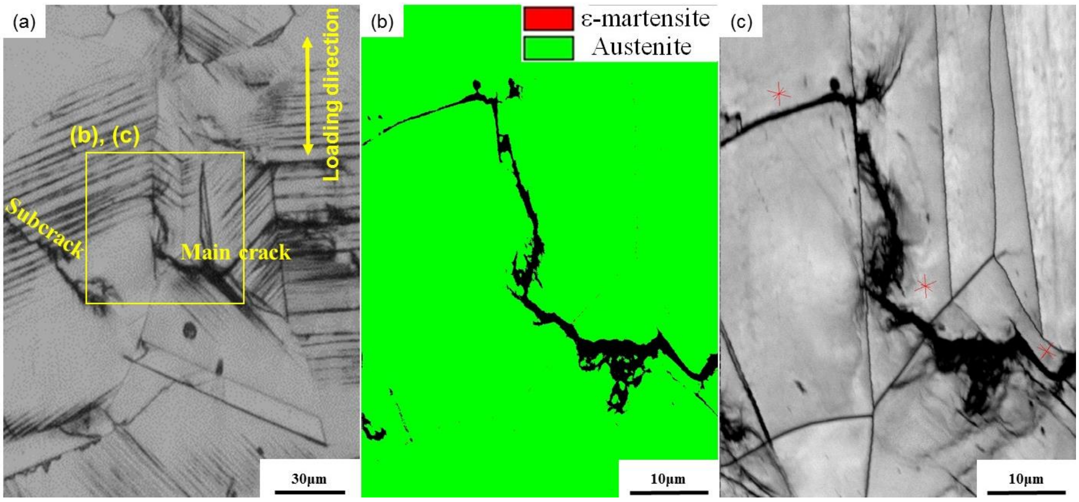

Fig. 2.9 (a) Optical microscope image of the Fe-30Mn-6Al alloy after the fatigue test (4.5×10^4 cycles). (b) Phase and (c) image quality maps corresponding to (a). The red lines in the image quality map indicate $\{111\}_\gamma$ planes.

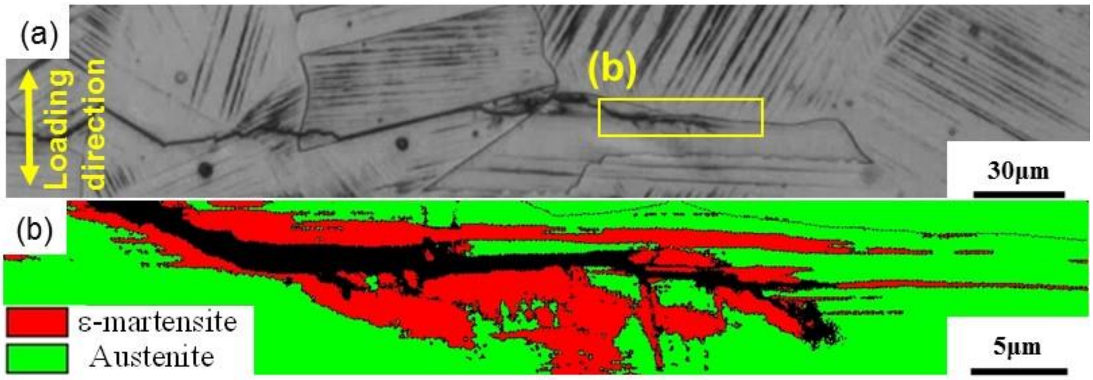

Fig. 2.10 (a) Optical microscope image of the Fe-30Mn-4Si-2Al alloy after the fatigue test (6.3×10^4 cycles). (b) EBSD phase map corresponding to the outlined region in (a).

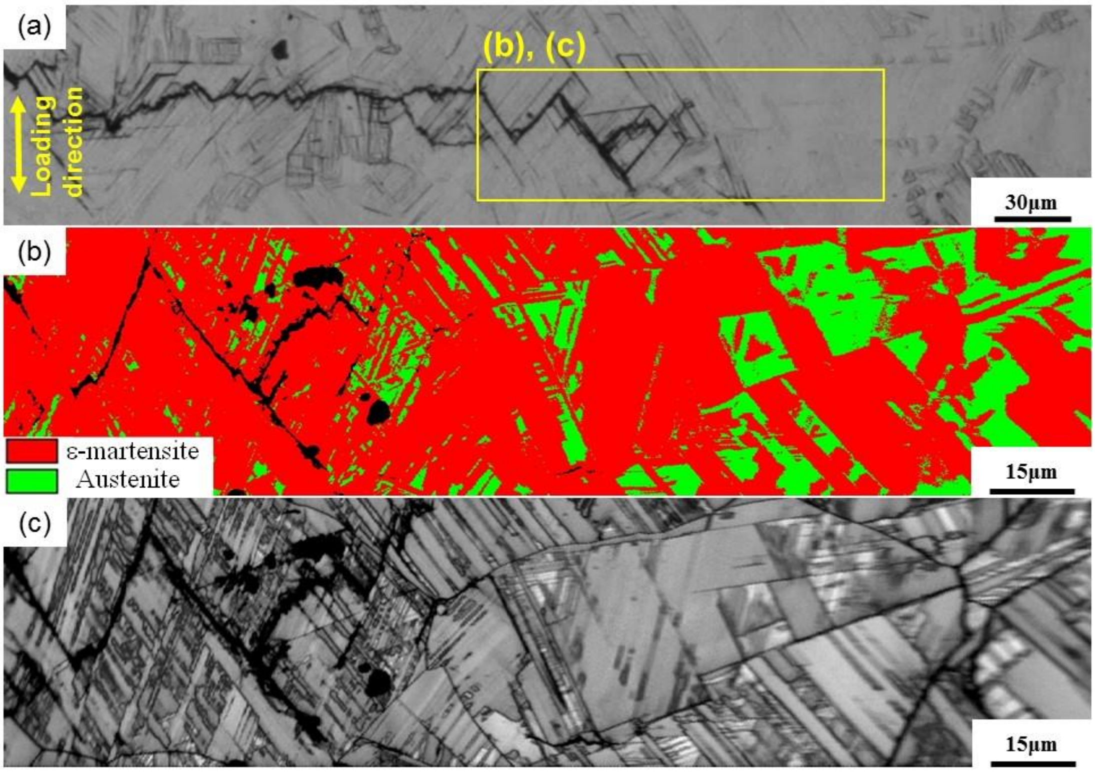

Fig. 2.11 (a) Optical microscope image of the Fe-30Mn-6Si alloy after the fatigue test (4.3 × 10^4 cycles). (b) Phase and (c) image quality maps corresponding to the outlined region in (a).

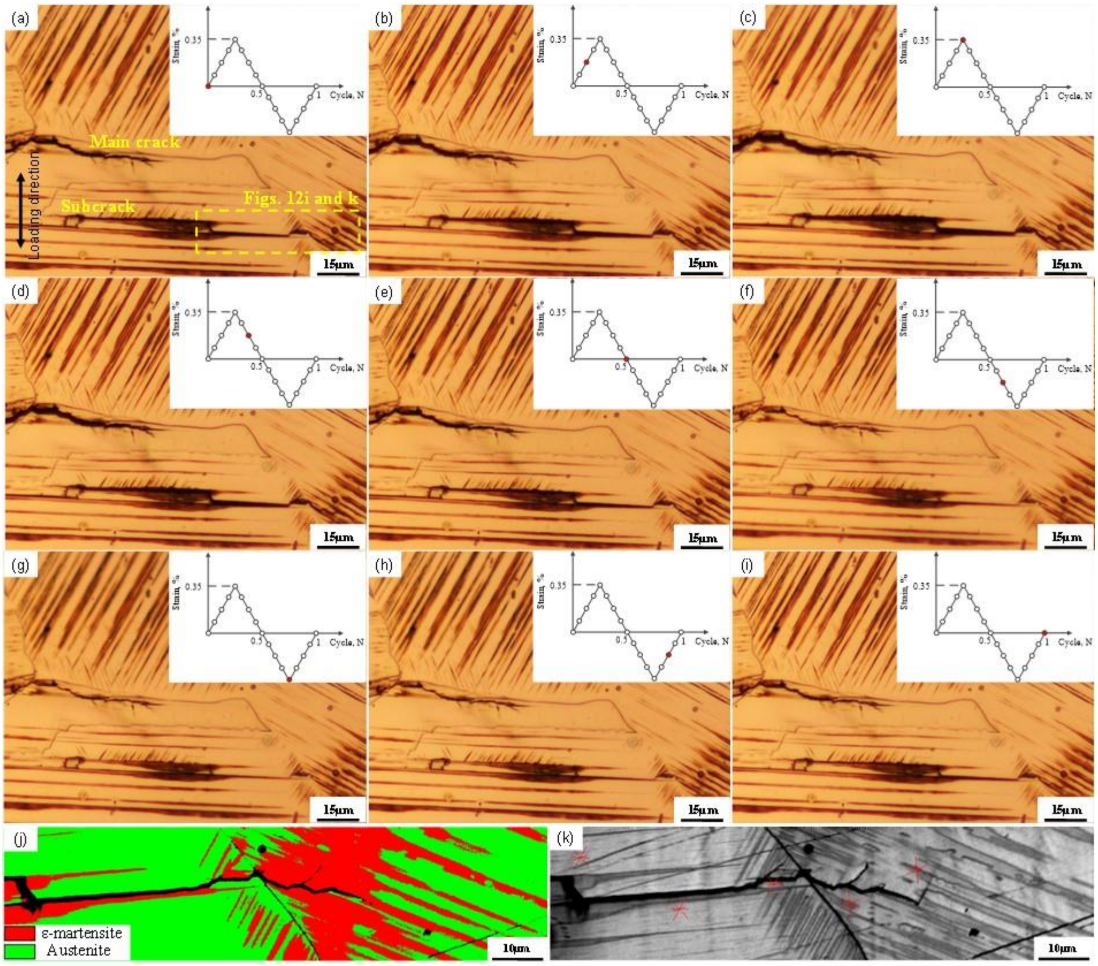

Fig. 2.12 In situ images of the Fe-30Mn-4Si-2Al alloy during one cycle of the fatigue test. These images were taken at 6.3 × 10^4 cycles. (a-i) The strain stages are indicated in the schematic graphs shown in the insets. (j) Phase and (k) image quality maps corresponding to the outlined region in (a).

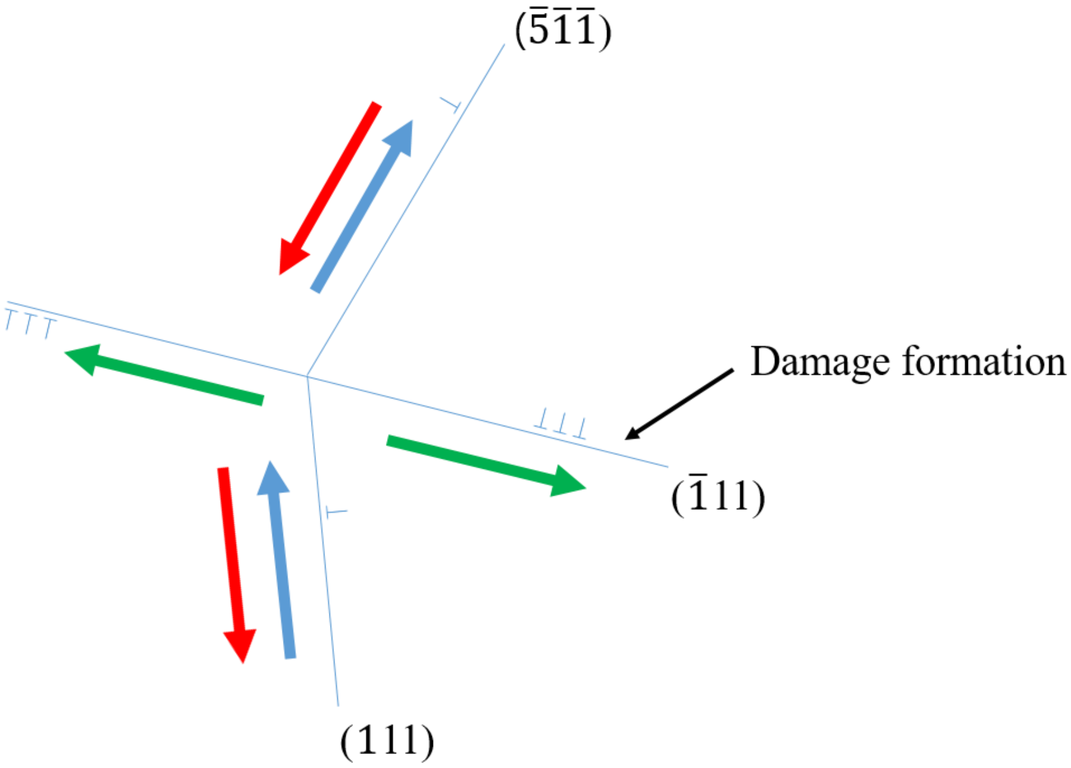

Fig. 2.13 Schematic diagram of the dislocation dissociation at the twin boundary.

CHAPTER 3. Effects of ε-martensitic transformation on crack tip deformation, plastic damage accumulation, and slip plane cracking associated with low cycle fatigue crack growth

3.1 Introduction

In chapter 2, macroscopic fatigue crack growth behavior was observed in situ by optical microscopy. The Fe-30Mn-6Al alloy showed ductile striations on fracture surface. This result indicates that a large plastic deformation is localized at the crack tip. In contrast with the Fe-30Mn-6Al alloy, the Fe-30Mn-4Si-2Al and Fe-30Mn-6Si alloys showed considerable ε-martensite near the crack path. However, the role of ε-martensite was quite different. Even the-30Mn-6Si alloy has been known to exhibit a great work hardening capacity, the occurrence of premature fracture that associated with ε-martensite-related cracking can cause extremely low elongation [1, 2]. The Fe-30Mn-4Si-2Al alloy showed the striation-like patterns on fracture surface of long crack region as shown in Fig. 2.6(l). Moreover, when the striation-like patterns were observed on fracture surface, the fatigue crack growth rate was still low, even though the rapidly increased fatigue crack length by crack coalescence with long subcrack as shown in Figs. 2.2, 2.6(i) and (l). These results indicate that the Fe-30Mn-4Si-2Al alloy has other effect of ε-martensitic transformation, as well as the positive effects of ε-martensitic transformation introduced in chapter 2 such as zigzag crack propagation, which enhances roughness-induced crack closure. Therefore, the further research is needed to investigate the low crack growth rate of the Fe-30Mn-4Si-2Al alloy.

The formation of ductile striation has been known as a result of crack blunting and re-sharpening [3, 4]. Moreover, the crack blunting and re-sharpening behavior requires a large degree of plastic strain localization [5, 6]. The low-cycle fatigue resistance of high Mn alloy is supposed that reverse transformation of ε-martensite has been recognized as the most important factor enhancing the resistance to low-cycle fatigue [7, 8]. More specifically, the reverse transformation is attributed to the forward and reverse motion of leading partials, which suppresses damage accumulation-related to low-cycle fatigue [9]. However, the relationship between the low fatigue crack growth and ε-martensitic transformation has not been thoroughly investigated in viewpoint of the localization of plastic deformation. In specific, the way in which the reverse transformation of ε-martensite decelerates the fatigue crack growth is still debatable. Moreover, we must also consider how the ε-martensitic transformation affects the deformation behavior geometrically at a crack tip based on the dislocation motions.

In order to discuss the effect of two factors mentioned above, performing a fractographic analysis and the associated electron backscatter diffraction measurements are expected to uncover the fatigue crack growth mechanism and fatigue-related plastic strain evolution, respectively. Furthermore, in order to extend the discussion from fatigue crack growth to fatigue life, the crack length dependence of the fatigue crack growth behavior must be noted. Namely, in the present study, we examine the relationship between the crack tip deformation and crack growth rate on one side, and its crack length dependency with considerations to ε-martensite cracking on the other side.

3.2 Experimental procedures

The Fe-30Mn-6Al, Fe-30Mn-4Si-2Al and Fe-30Mn-6Si alloy were used to evaluate the plastic deformation localization. The chemical composition and the results of tensile test are shown in Figs. 1.2 and 1.3. In chapter 2, the bending fatigue test was conducted to obtain the fracture surface until 1 mm crack length. Moreover, the same specimen was used in present chapter. However, the observation area of fracture surfaces was different to that of chapter 2. Fig. 3.1 shows the specimen geometry and observation area for further fracture surface and EBSD measurement. Additional observation of fracture surfaces was conducted by scanning electron microscopy (SEM) at an accelerating voltage of 20 kV and at around 2 mm crack length to extend the discussion of the crack growth behavior change as shown in Fig. 3.1(c). Then, the specimens for the SEM observations were mechanically polished from a side until the center of the specimen width (2 mm was removed) to observe the microstructures underneath the fracture surface as shown in Fig. 3.1(d) [10, 11]. The microstructures near the short and long crack regions were observed by electron backscatter diffraction measurements (EBSD) at an accelerating voltage of 15 kV and a beam step size of 50 nm. The grain reference orientation deviation (GROD) was used to confirm the distributions and maximum value of plasticity deformations.

3.3 Results

3.3.1 Fracture surface observation pertaining to short and long fatigue crack growth

Fig. 3.2 shows SEM fractographs of the regions corresponding to short crack parts (300 μm from the drill hole) of the respective alloys. All of the facture surfaces show quasi-cleavage-like features. In addition, significant roughness is observed on the fracture surface of all the alloys. This roughness might correspond to the zigzag propagation shown in Figs. 2.3, 2.5 and 2.7.

Fig. 3.3 shows the fracture surfaces at 900 μm from the drill hole. The fatigue striations appeared on the fracture surface of the Fe-30Mn-6Al alloy, shown in Fig. 3.3(a), are similar to the striation feature observed in chapter 2 as shown in Fig. 2.4(l). This result indicates that the fatigue crack growth mechanism of the Fe-30Mn-6Al alloy at 900 μm is different to that at 300 μm. In contrast, the fatigue striations were not observed at 900 μm from the drill hole of the Fe-30Mn-4Si-2Al and the Fe-30Mn-6Si alloys. Instead, striation-like patterns were observed on the fracture surface of the Fe-30Mn-4Si-2Al alloy, as shown in Fig. 3.3(b), which is different from the striations observed on the fracture surface of the Fe-30Mn-6Al alloy. These results indicate that the fatigue crack growth mechanism of the Fe-30Mn-4Si-2Al alloy changes at 900 μm and the mechanism is different to the Fe-30Mn-6Al alloy showing ductile striations. The Fe-30Mn-6Si alloy shows subcracks on the fracture surface at 900 μm, as shown in Fig. 3.3(c).

Fig. 3.4 shows the fracture surfaces at around 2 mm from the drill hole. Fatigue striations with increased spaces were observed in the Fe-30Mn-6Al alloy, as shown in Fig. 3.4(a). Similar fatigue striation was also observed in the Fe-30Mn-4Si-2Al alloy, as shown in Fig. 3.4(b). In addition, the striation spacing was narrower than that of the Fe-30Mn-6Al alloy at the same crack length. These results indicate that the fatigue crack growth mechanism of the Fe-30Mn-4Si-2Al alloy is comparable to the Fe-30Mn-6Al alloy in the long crack region with crack length of 2 mm, and associated crack growth rate of the Fe-30Mn-4Si-2Al alloy is relatively low even after 1 mm crack length. In contrast, such fatigue striation was not observed in the Fe-30Mn-6Si alloy, not even at 2 mm crack length.

3.3.2 EBSD measurements at the vicinities of fracture surfaces

Fig. 3.5 illustrates a SEM image and a set of EBSD measurements results at an identical relatively short crack part formed in the Fe-30Mn-6Al alloy. The phase and orientation maps, respectively shown in Figs. 3.5(b) and (c), indicate that ε-martensite and deformation twin did not form; instead, highly strain-localized bands that markedly decrease the image quality exist. Fig. 3.5(d) shows a GROD map that qualitatively corresponds to the plastic strain distribution in each grain [12]. High concentration of plastic deformation is observed near the slip bands, grain boundary, and fractured part.

Fig. 3.6 shows a SEM image and a set of EBSD results taken at the short crack region in the Fe-30Mn-4Si-2Al alloy. It can clearly be seen in Fig. 3.6(b) that considerable amount of ε-martensite appears particularly near the fractured part. Deformation twins were not detected in this measurement, as shown in Fig. 3.6(c). The high concentration of plastic strain existed in the ε-martensite plates, particularly near the fractured part, is the most important feature shown in Fig. 3.6(d). The maximum reported value of GROD is 27. Note that this GROD value is lower than that of the Fe-30Mn-6Al alloy (maximum GROD: 39). Furthermore, the amount of ε-martensite in the Fe-30Mn-6Si alloy is increased compared to that of the Fe-30Mn-4Si-2Al alloy, as shown in Fig. 3.7(b). Although ε-martensite forms and distribution of plastic strain deformation is widespread in the Fe-30Mn-6Si alloy at the short crack part (Fig. 3.7(b)), the maximum GROD value obtained is approximately 7. Hence, the contribution of plastic deformation within ε-martensite to fatigue crack growth in the Fe-30Mn-6Si alloy is much lower compared to the other two alloys.

The Fe-30Mn-6Al alloy did not develop ε-martensite or form deformation twins, not even at the long crack part, as shown in Figs. 3.8(b) and (c). The maximum GROD of the corresponding area (shown in Fig. 3.5(d)) is slightly higher than that at the short crack part (Fig. 3.8(d)), indicating that a comparable or higher plastic strain was developed by the fatigue crack growth at the long crack length compared to that at the short crack length. Note that plastic deformation of the Fe-30Mn-6Al is localized along the crack path.

Fig. 3.9 and 3.10 show the same sets of SEM/EBSD analyses at long crack parts of the Fe-30Mn-4Si-2Al and Fe-30Mn-6Si alloys, respectively. Note that plastic deformation of the Fe-30Mn-4Si-2Al alloy is localized on fracture surface like the Fe-30Mn-6Al alloy as shown in Fig. 3.9(d). In addition, a volume fraction of ε-martensite decreases compared with that of short crack region shown in Fig. 3.6(b). The localization of plastic strain and decreasing volume fraction of ε-martensite may indicate that the fatigue crack growth mechanism of the Fe-30Mn-4Si-2Al alloy become similar to the Fe-30Mn-6Al alloy at 900 μm. However, the maximum GROD of the Fe-30Mn-4Si-2Al alloy is still lower than the Fe-30Mn-6Al alloy. Therefore, the crack growth mechanism of the Fe-30Mn-4Si-2Al alloy is supposed that the crack growth mechanism is changing, but still slightly different at 900 μm. However, The order of the maximum GROD did not depend on the crack length: 42, 21, and 9 for the Fe-30Mn-6Al, Fe-30Mn-4Si-2Al, and Fe-30Mn-6Si alloys at the long crack parts, respectively (the corresponding GROD at the short crack parts are 39, 27, and 7). It is found that the amount of localized plastic strain decreases with increasing the Si content (or decreasing the Al content).

3.4 Discussion

3.4.1 Correlation between strain localization and crack growth, and its crack length dependence: the chemical composition effects on fatigue behavior

The obtained experimental results are summarized in terms of crack propagation path, strain localization, and crack length dependence, as follows:

a) The fracture surfaces (Fig. 3.2) in all of the three alloys revealed that crack propagation along the slip plane occurs when the crack length is short.

b) The Fe-30Mn-6Al alloy showed ductile fatigue striations at a crack length of 900 μm as shown in Fig. 3.3(a), which corresponds to the result of chapter 2.

c) The Fe-30Mn-6Al alloy showed the highest degree of strain localization in the vicinities of fracture surface. The degree of strain localization decreased with the Si content increase (or Al content decrease), regardless of crack length, as shown in Figs. 3.5 to 3.10.

d) Fatigue cracking of the Fe-30Mn-6Si alloy mostly occurred along γ/ε interfaces with a low plastic strain in ε-martensite, irrespective of crack length, as shown in Figs. 3.2 to 3.4. Accordingly, fatigue striation was not detected at all.

e) The Fe-30Mn-4Si-2Al alloy showed significant plastic deformation in ε-martensite pertaining to fine zigzag crack propagation partially along γ/ε interfaces until 900 μm. When the crack length increased to 2 mm, fatigue striation appeared, as shown in Fig. 3.4.

The fact (a) indicates that the Fe-30Mn-6Al alloy shows fatigue crack growth associated with damage accumulation, i.e. localization of lattice defects such as dislocation when the fatigue crack was short. Then, as revealed by the fact (b), the fatigue crack growth mechanism of this alloy changes to deformation-induced blunting and subsequent re-sharpening accompanied by striation formation when the fatigue crack is large. Both of the fatigue crack growth mechanisms of this alloy require a large degree of plastic strain localization, which corresponds to the fact (c). These fatigue crack growth mechanisms in the Fe-30Mn-6Al alloy are typical in ductile FCC metals [5, 6].

In contrast, the fatigue crack growth behavior of the Fe-30Mn-6Si alloy appears like a brittle manner related to γ/ε interfaces, regardless of the crack length as mentioned in the fact (d). Both of the Fe-30Mn-6Al and the Fe-30Mn-6Si alloys show crack growth along slip planes in short crack regions. However, large plastic strain localization is not observed in the Fe-30Mn-6Si alloy, not even in a long crack region, as shown in Fig. 3.10(d). These facts imply that the fatigue cracking of the Fe-30Mn-6Si alloy occurs along γ/ε interface, instead of the damage-accumulation-controlled crack growth or deformation-induced blunting and subsequent re-sharpening mechanisms. The Fe-30Mn-6Si alloy shows subcracks on the fracture surface of long crack regions (Figs. 3.3 and 3.4), which is hypothesized that the subcrack formed at the vicinity of the crack tip and subsequently coalesced with the main crack, as schematically illustrated in Fig. 3.11. The crack formation arising from ε-martensite/ε-martensite interactions has been well recognized to occur in high Mn austenitic steels [13, 14]. Note that a considerable amount of ε-martensite is observed even in locations far from the crack tip. The pre-existing ε-martensite would play an important role to assist the brittle-like fatigue cracking. This can be the reason why fatigue striation did not appear, irrespective of crack length, as mentioned in the fact (d).

Finally, we discuss the crack growth characteristics in the Fe-30Mn-4Si-2Al alloy that showed the lowest growth rate. In order to understand the nature of the high fatigue crack resistance, we must note the presence of significant plastic strain and formation of striation in the Fe-30Mn- 4Si-2Al alloy [fact (c) and (e)]. Unlike the Fe-30Mn-6Si alloy, the fatigue crack growth mechanism of the Fe-30Mn-4Si-2Al alloy does not display brittle manner, since the ductile fatigue striation appears when the crack becomes long, as mentioned in the fact (e). Accordingly, the short crack propagation mechanism is considered to stem from damage accumulation such as in the Fe-30Mn-6Al alloy, even if the crack propagation path is along γ/ε interface (in chapter 2, the fatigue crack growth along γ/ε interface was observed actually in the Fe-30Mn-4Si-2Al alloy). Assuming that the short crack growth is caused by ductile damage accumulation along ε-martensite plates at the crack tip, the damage accumulation is inhibited by the reversible transformation of ε-martensite that stems from repetitive motion of leading partials on an identical slip plane [7-9], as will be discussed in details later. Therefore, the short crack growth associated with ductile damage accumulation is decelerated by the ε-martensitic transformation as long as the ε-martensite interface does not act as brittle cracking path. This phenomenon is one of reasons why the crack growth rate of the Fe-30Mn-4Si-2Al alloy was relatively low compared to the other two alloys. The deformation-induced reverse transformation of ε-martensite decreases the residual plastic strain, which corresponds to the fact (c). Hence, the Fe-30Mn-4Si-2Al alloy has higher plastic strain level than the Fe-30Mn- 6Si alloy because of suppression of the brittle-like cracking, while it has lower degree of plastic strain than the Fe-30Mn-6Al alloy that attributed to the reversible transformation of ε-martensite. Furthermore, even when the crack is long, the fatigue crack growth rate of the Fe-30Mn-4Si-2Al alloy was lower than the other tested alloys, as shown in Fig. 2.2. Therefore, another crack growth deceleration mechanism exists pertaining to the fatigue striation formation. Within this context, in order to discuss the underlying mechanisms of short and long crack growth in the Fe-30Mn-4Si-2Al alloy, the focus will be on the effects of ε-martensite on 1) lattice defect accumulation, 2) crack tip deformation, and 3) occurrence of brittle-like cracking. These three points will be discussed in the following section using a newly proposed crack growth model based on the crystallography of ε-martensite.

3.4.2 Contribution of ε-martensitic transformation in deceleration of fatigue crack growth: from the viewpoint of crack tip deformation

In this section, we discuss the crack tip deformation mechanisms with and without ε-martensitic transformation. A continuous fatigue crack growth pertaining to crack blunting and re-sharpening has been considered as dislocation-based geometrical deformation of a crack tip [15, 16]. Fig. 3.12 shows a schematic diagram that illustrates an assumed fatigue crack growth mechanism during one cycle associated with crack tip deformation caused by perfect dislocation motions. When loading is applied to a specimen, dislocations are emitted from a crack tip which opens the crack tip. Ideally, further loading causes symmetrical dislocation emissions at the crack tip, which brings about crack blunting and crack growth. Consider that the emitted dislocations are pinned by solute atoms or pre-existing dislocations, while other dislocations formed from Frank-Read sources, and are subsequently absorbed to the crack surface causing crack closing. The resulting displacement of the crack tip perpendicular to the loading direction is a crack growth length during one cycle, Δa. Alternatively, as shown in Fig. 3.13, another type of fatigue crack growth can be caused by dislocation accumulation at a crack tip [17], which stems from asymmetrical dislocation emission from a crack tip or enormous dislocation multiplication in a plastic zone formed by stress concentration at the crack tip.

Here, we discuss micro-mechanisms of ε-martensitic transformation-driven crack tip deformation based on the abovementioned two crack growth models. An ideal case with phenomenologically accepted facts will be considered based on the following assumptions:

1) ε-martensitic transformation is a primary plasticity mechanism that occurs at a crack tip, as indicated by the present study and chapter 2 [18].
2) A leading partial dislocation rather than perfect dislocation is emitted from the crack tip in order to form ε-martensite.

3) The required stress for slip/twinning of ε-martensite is higher than the critical stress for ε-martensitic transformation.

4) The deformation-induced reverse transformation of ε-martensite exceptionally occurs by counter directional stress (compression after tension and vice versa) [7, 8]. This probably occurs because of the presence of back stress at a tip of ε-martensite plates that impinged at microstructural obstacles [19, 20].

5) Ductile micro-void formation at the vicinity of the fatigue crack does not occur during the cyclic loading.

Based on the above assumptions, we propose a model of geometrical effects of ε-martensitic transformation on a crack tip deformation, as shown in Fig. 3.14. Intrinsically, the motion of leading partials and subsequent formation of intrinsic stacking fault are the formation mechanism of ε-martensite [21, 22]. Therefore, during loading, first, a leading partial is emitted from a crack tip. Next, the second leading partial cannot sweep the same slip plane as the first leading partial motion, because of the crystallography of intrinsic stacking fault. A schematic diagram that illustrates this crystallography is shown in Fig. 3.15. A Leading partial dislocation motion changes the atomic sequence from A-B-C (austenite) to A-C-A (ε-martensite), as shown in the schematic diagrams. After A-C-A stacking sequence formation, an additional leading partial motion with the same Burgers vector that forms A-A atomic stacking sequence is energetically unfavorable in FCC crystals [21]. Thus, the second leading partial must be emitted along a near-symmetrical slip plane. Note that the third leading partial cannot be emitted from the crack tip. If the third leading partial is emitted along the neighboring slip plane of the intrinsic stacking faults, the stacking sequence becomes an extrinsic stacking fault that is a nucleus of the FCC twin, not ε-martensite, which indicates that the third dislocation emission from the crack tip is not energetically favored in the present assumptions. In other words, the neighboring slip planes plotted by red line in Fig 3.14 are geometrically immobile planes. Instead, pre-existing dislocation sources such as those activated at the vicinity of the crack front where stress is highly concentrated move to form ε-martensite. However, the pre-existing dislocation motion at the vicinity of the crack front does not contribute to crack growth and crack tip opening displacement, which means that stress concentration at the crack tip is not accommodated. Therefore, the partial dislocations must be emitted from the crack surface behind the crack tip. The atomistic zigzag structure of the crack wake decreases the macroscopic curvature of the crack tip, thus relaxing the stress concentration. During unloading or compressive loading, ε-martensite may transform reversely. However, part of ε-martensite remains even after one loading cycle, since a considerable amount of the remaining ε-martensite was observed in the vicinity of the fracture surfaces, as seen in Figs. 3.6, 3.7, 3.9, and 3.10.

The remaining ε-martensite must inhibit crack tip deformation during the next cycle. To cause significant crack tip deformation in the next cycle, ε-martensite must be deformed plastically through slip, twinning, or α'-martensitic transformation. When the plastic deformability of ε-martensite is not sufficient, the plastic deformation requirement of ε-martensite causes quasi-cleavage cracking along γ/ε interfaces that corresponds to slip plane. The occurrence of brittle-like cracking in the Fe-30Mn-6Si alloy stems from the low ductility of ε-martensite. In fact, ε-martensite in high Mn austenitic steels including the Fe-30Mn-6Si alloy has been reported to show the distinct brittle-like fracture in monotonic tension experiments [13, 23, 24]. Specifically, when the Si content is increased to over 5 wt.% in high Mn alloys, the ratio of lattice constants c/a of ε-martensite becomes close to that of the ideal hexagonal close-packed (1.633) [25]. Non-basal slip cannot preferentially occur in the near-ideal close-packed structure, because the interplanar spacing of the basal plane is much smaller than those of the other crystallographic planes. This consideration must be noted as a reason why the Fe-30Mn-6Si alloy showed brittle-like cracking associated with the low ductility of ε-martensite. In contrast, the Fe-30Mn-4Si-2Al alloy is much more ductile than the Fe-30Mn-6Si alloy [26]. Accordingly, as seen in the GROD map of Figs. 3.6(d) and 3.9(d), ε-martensite of the Fe-30Mn-4Si-2Al alloy was observed to be more plastically deformable than that of the Fe-30Mn-6Si alloy. Thus, the plastic deformation of ε-martensite could occur to accommodate stress concentration at the crack tip even with the presence of a considerable amount of ε-martensite that formed in a prior fatigue cycle. Yet, the plastic deformation in ε-martensite requires higher stress compared to slip, which can be another reason for the low crack growth rate in the Fe-30Mn4Si-2Al alloy. Moreover, the striation formation arises from heterogeneous plastic deformation on the crack surface around the crack tip. For example, Laird et al. described [27, 28] a schematic for heterogeneously stretching zone at a crack tip to explain the striation formation. As indicated in Fig. 3.14, because of the crystallographic constraint of ε-martensite, locally stretching zone cannot form easily. In order to develop striation patterns via formation of a stretching zone, ε-martensite must be highly deformed at the crack tip. Therefore, it is also considered that ε-martensitic transformation at a crack tip delays striation formation, which is a reason why the striations of the Fe-30Mn-4Si-2Al alloy appears only at the long crack (the fact (e) in Section 3.4.1)

In addition, when the crack tip deformation cannot occur easily in such abovementioned case, the fatigue crack growth along slip plane that associated with the dislocation accumulation during cyclic loading must be considered to occur as shown in Fig. 3.13. The dislocation accumulation is difficult to occur when ε-martensitic transformation acts as a primary plasticity mechanism. This is because the reversible ε-martensite must suppress the accumulation of dislocations that cause the slip plane cracking. Thus, when fatigue crack growth occurs via damage accumulation, the fatigue crack growth rate is relatively low compared to the case without ε-martensite. Namely, in terms of crack tip deformation, it is summarized that reversible deformation-induced ε-martensitic transformation can suppress both of the crack growth mechanisms arising from crack tip deformation and the dislocation accumulation on a slip plane. Accordingly, the Fe-30Mn-4Si-2Al alloy with ductile ε-martensite could show markedly low fatigue crack growth rate.

3.5 Conclusions

In this study, fully reversed bending fatigue tests are conducted in Fe-30Mn-6Al, Fe-30Mn-4Si-2Al, and Fe-30Mn-6Si alloys with different austenite stability to ε-martensitic transformation. Accordingly, the fracture surfaces and plastic deformation localization near the crack growth path were analyzed. Consequently, the following conclusions were drawn:

(1) The fatigue crack growth mechanism of the Fe-30Mn-6Al and Fe-30Mn-4Si-2Al alloys changes from crack propagation along slip plane to crack growth with striations. The critical crack length for the growth mechanism transition of the Fe-30Mn-4Si-2Al alloy was greater than that of the Fe-30Mn-6Al alloy. In contrast, the Fe-30Mn-6Si alloy did not show striation until failure.

(2) Both of Fe-30Mn-4Si-2Al and Fe-30Mn-6Si alloys showed fatigue crack propagation along γ/ε interface. However, more fine zigzag propagation path configuration was observed in the Fe-30Mn-4Si-2Al alloy compared to that of the Fe-30Mn-6Si alloy. The crack growth mode along the interface in the Fe-30Mn-6Si alloy is brittle-like cracking, while that in the Fe-30Mn-4Si-2Al is ductile mode with a considerable amount of plastic staining.

(3) The ε-martensite formed in the vicinity of the fractured part of the Fe-30Mn-6Si alloy was not remarkably plastically deformed, even when the crack is long. In contrast, the ε-martensite formed in the Fe-30Mn-4Si-2Al alloy was observed to contain a considerable amount of plastic strain. In other words, the

ε-martensite formed in the Fe-30Mn-4Si-2Al alloy is more ductile than that of the Fe-30Mn-6Si alloy.

(4) The geometric constraint of crack tip deformation that arises from the crystallographic structure of ε-martensite is believed to decelerate fatigue crack growth rate. When this effect of ε-martensite works, significant plastic deformability of ε-martensite is required such as the case of the Fe-30Mn-4Si-2Al alloy. Therefore, the Fe-30Mn-4Si-2Al alloy showed a lower fatigue crack growth rate than the other tested alloys, and showed striation even with ε-martensite when the crack becomes long.

References

[1] O. Grässel, L. Krüger, G. Frommeyer, L.W. Meyer, High strength Fe–Mn–(Al, Si) TRIP/TWIP steels development— properties — application, Int. J. Plast. 16 (2000) 1391-1409.

[2] D.R. Steinmetz, T. Jäpel, B. Wietbrock, P. Eisenlohr, I. Gutierrez-Urrutia, A. Saeed–Akbari, T. Hickel, F. Roters, D. Raabe, Revealing the strain-hardening behavior of twinning-induced plasticity steels: Theory, simulations, experiments, Acta Mater. 61 (2013) 494-510.

[3] J. Schijve, Fatigue of Structures and Materials, Springer, 2009

[4] S. Suresh, Fatigue of Materials, Cambridge, 1998

[5] C. Laird, G.C. Smith, Initial stages of damage in high stress fatigue in some pure metals, Phil. Mag. Lett. 8 (1963) 1945-1963.

[6] P.J.E. Forsyth, Fatigue damage and crack growth in aluminium alloys, Acta Metall. 11 (1963) 703-715.

[7] T. Sawaguchi, L.-G. Bujoreanu, T. Kikuchi, K. Ogawa, M. Koyama, M. Murakami, Mechanism of reversible transformation-induced plasticity of Fe–Mn–Si shape memory alloys, Scri. Mater. 59 (2008) 826-829.

[8] H. Li, M. Koyama, T. Sawaguchi, K. Tsuzaki, H. Noguchi, Importance of crack-propagation-induced ε-martensite in strain-controlled low-cycle fatigue of high-Mn austenitic steel, Phil. Mag. Lett. (2015) 1-9.

[9] T. Sawaguchi, I. Nikulin, K. Ogawa, K. Sekido, S. Takamori, T. Maruyama, Y. Chiba, A. Kushibe, Y. Inoue, K. Tsuzaki, Designing Fe–Mn–Si alloys with

improved low-cycle fatigue lives, Scr. Mater. 99 (2015) 49-52.

[10] M. Koyama, Y. Onishi, H. Noguchi, Characteristics of hydrogen-assisted intergranular fatigue crack growth in interstitial-free steel: role of plastic strain localization, Int. J. Fract. (2017) 1-8.

[11] K. Habib, M. Koyama, H. Noguchi, Impact of Mn–C couples on fatigue crack growth in austenitic steels: Is the attractive atomic interaction negative or positive?, Int. J. Fat. 99. Part 1 (2017) 1-12.

[12] H.-a. Nishikawa, Y. Oda, Y. Takahashi, H. Noguchi, Microscopic Observation of the Brittle-Striation Formation Mechanism in Low Carbon Steel Fatigued in Hydrogen Gas (TEM and EBSD Observation Corresponding to Fractography), J. Solid Mech. Mater. Eng. 5 (2011) 179-190.

[13] M. Koyama, T. Sawaguchi, K. Tsuzaki, Effects of Si on Tensile Properties Associated with Deformation-Induced ε-Martensitic Transformation in High Mn Austenitic Alloys, Mater. Trans. 56 (2015) 819-825.

[14] S. Takaki, T. Furuya, Y. Tokunaga, Effect of Si and Al Additions on the Low Temperature Toughness and Fracture Mode of Fe-27Mn Alloys, ISIJ. Int. 30 (1990) 632-638.

[15] P. Neumann, New experiments concerning the slip processes at propagating fatigue cracks—I, Acta Metall. 22 (1974) 1155-1165.

[16] Y. Oda, Y. Furuya, H. Noguchi, K. Higashida, AFM and SEM observation on mechanism of fatigue crack growth in an Fe-Si single crystal, Int. J. Fract. 113 (2002) 213-231.

[17] K. Tanaka, T. Mura, Fatigue crack growth along planar slip bands, Acta Metall. 32 (1984) 1731-1740.

[18] H. Li, M. Koyama, T. Sawaguchi, K. Tsuzaki, H. Noguchi, Importance of crack-propagation-induced ε-martensite in strain-controlled low-cycle fatigue of high-Mn austenitic steel, Phil. Mag. Lett. (2015) 1-9.

[19] S. Kajiwara, D. Liu, T. Kikuchi, N. Shinya, Remarkable improvement of shape memory effect in Fe-Mn-Si based shape memory alloys by producing NbC precipitates, Scr. Mater. 44 (2001) 2809-2814.

[20] Y.H. Wen, L.R. Xiong, N. Li, W. Zhang, Remarkable improvement of shape memory effect in an Fe–Mn–Si–Cr–Ni–C alloy through controlling precipitation direction of Cr23C6, Mater. Sci. Eng. A 474 (2008) 60-63.

[21] G.B. Olson, M. Cohen, A general mechanism of martensitic nucleation: Part I. General concepts and the FCC → HCP transformation, Metall. Trans. A 7 (1976) 1897-1904.

[22] Y. Hoshino, S. Nakamura, N. Ishikawa, Y. Yamaji, S. Matsumoto, Y. Tanaka, A. Sato, In-situ Observation of Partial Dislocation Motion during γ ↔ ε Transformation in a Fe–Mn–Si Shape Memory Alloy, Mater. Trans. JIM. 33 (1992) 253-262.

[23] M. Koyama, T. Sawaguchi, K. Tsuzaki, Premature Fracture Mechanism in an Fe-Mn-C Austenitic Steel, Metallurgical and Mater. Trans. A 43 (2012) 4063-4074.

[24] K. Ogawa, T. Sawaguchi, T. Kikuchi, M. Koyama, M. Murakami, Influence of Al concentration on deformation behavior and fracture mode of fe-30Mn-6(Si, Al) alloys, SMST-2007. 2008.

[25] N. Stanford, D.P. Dunne, Effect of Si on the reversibility of stress-induced martensite in Fe–Mn–Si shape memory alloys, Acta Mater, 58 (2010) 6752-6762.

[26] M. Koyama, M. Murakami, K. Ogawa, T. Kikuchi, T. Sawaguchi, Influence of Al on shape memory effect and twinning induced plasticity of Fe-Mn-Si-Al system alloy, Mater. Trans. 48 (2007) 2729-2734.

[27] C. Laird, The influence of metallurgical structure on the mechanisms of fatigue crack propagation, in: Fatigue crack propagation, ASTM Int. 1967.

[28] C. Laird, R. de la Veaux, Additional evidence for the plastic blunting process of fatigue crack propagation, Metall. Trans. A 8 (1977) 657-664.

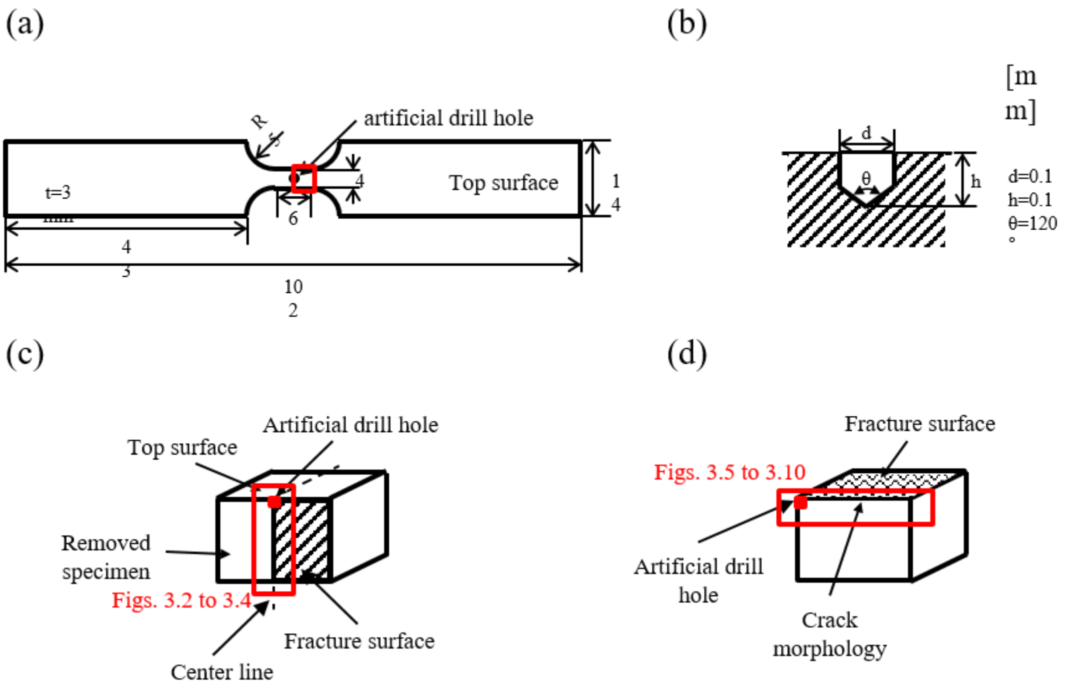

Fig. 3.1 (a) Specimen geometry used for the bending fatigue test. (b) Magnified schematic of the shape of the drill hole. (c) A schematic of fractured specimen cut by saw machine for fracture surface observation. (d) Mechanically polished specimen geometry until the center line for the observation of crack morphology and corresponding microstructure.

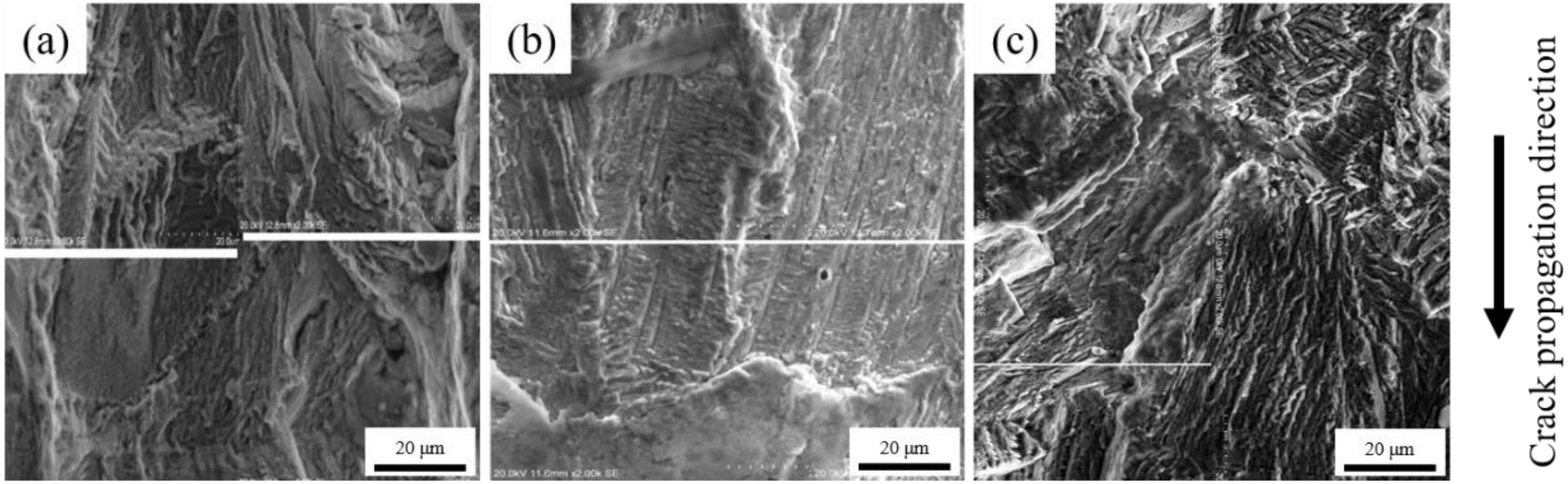

Fig. 3.2 Fatigue fracture surfaces at 300 μm from the drill hole in the (a) Fe-30Mn-6Al, (b) Fe-30Mn-4Si-2Al, and (c) Fe-30Mn-6Si alloy specimens. The loading direction is perpendicular to the crack propagation direction.

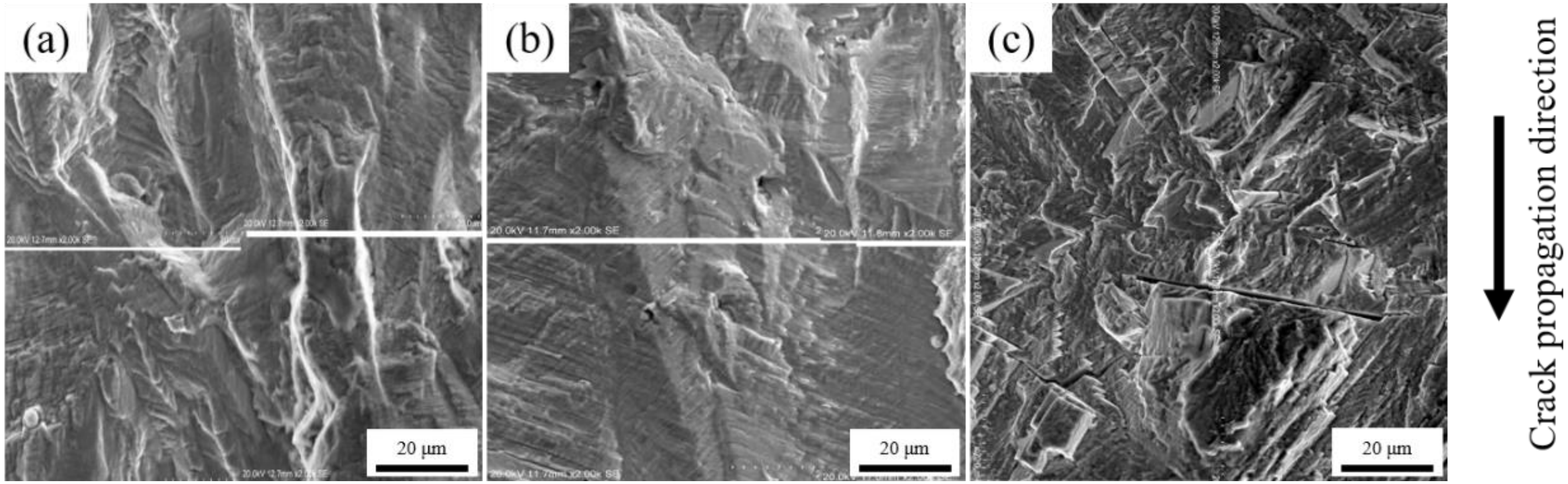

Fig. 3.3 Fatigue fracture surfaces at 900 μm from the drill hole of the (a) Fe-30Mn-6Al, (b) Fe-30Mn-4Si-2Al, and (c) Fe-30Mn-6Si alloy specimens. The loading direction is perpendicular to the crack propagation direction.

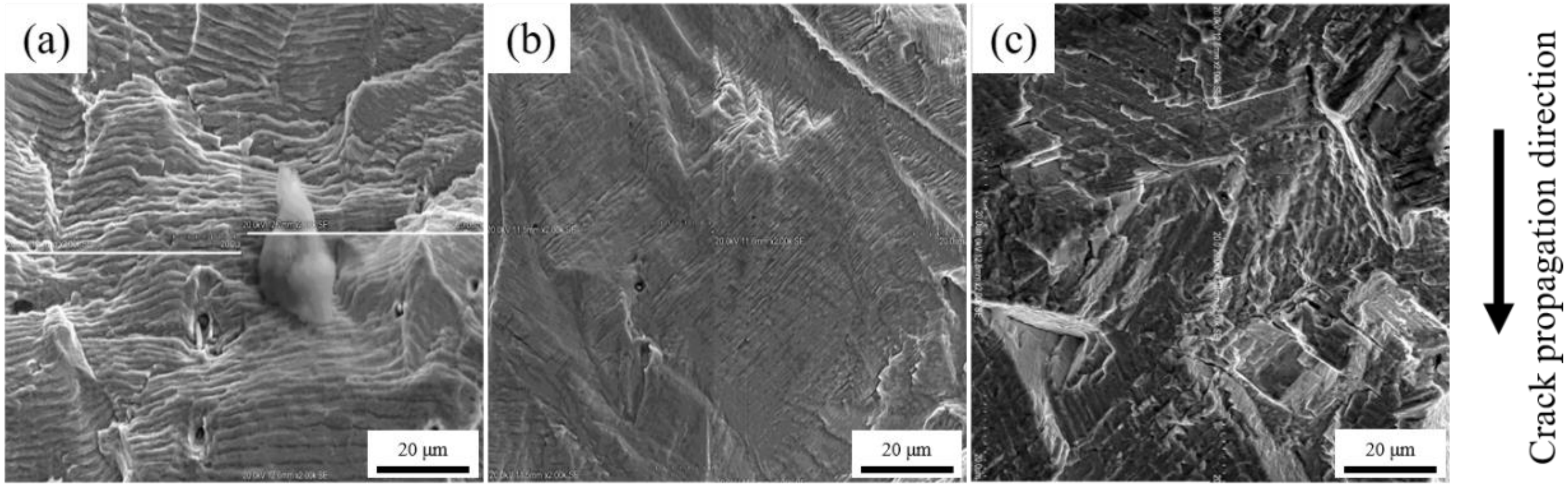

Fig. 3.4 Fatigue fracture surfaces at 2 mm from the drill hole of the (a) Fe-30Mn-6Al, (b) Fe-30Mn-4Si-2Al, and (c) Fe-30Mn-6Si alloy specimens. The loading direction is perpendicular to the crack propagation direction.

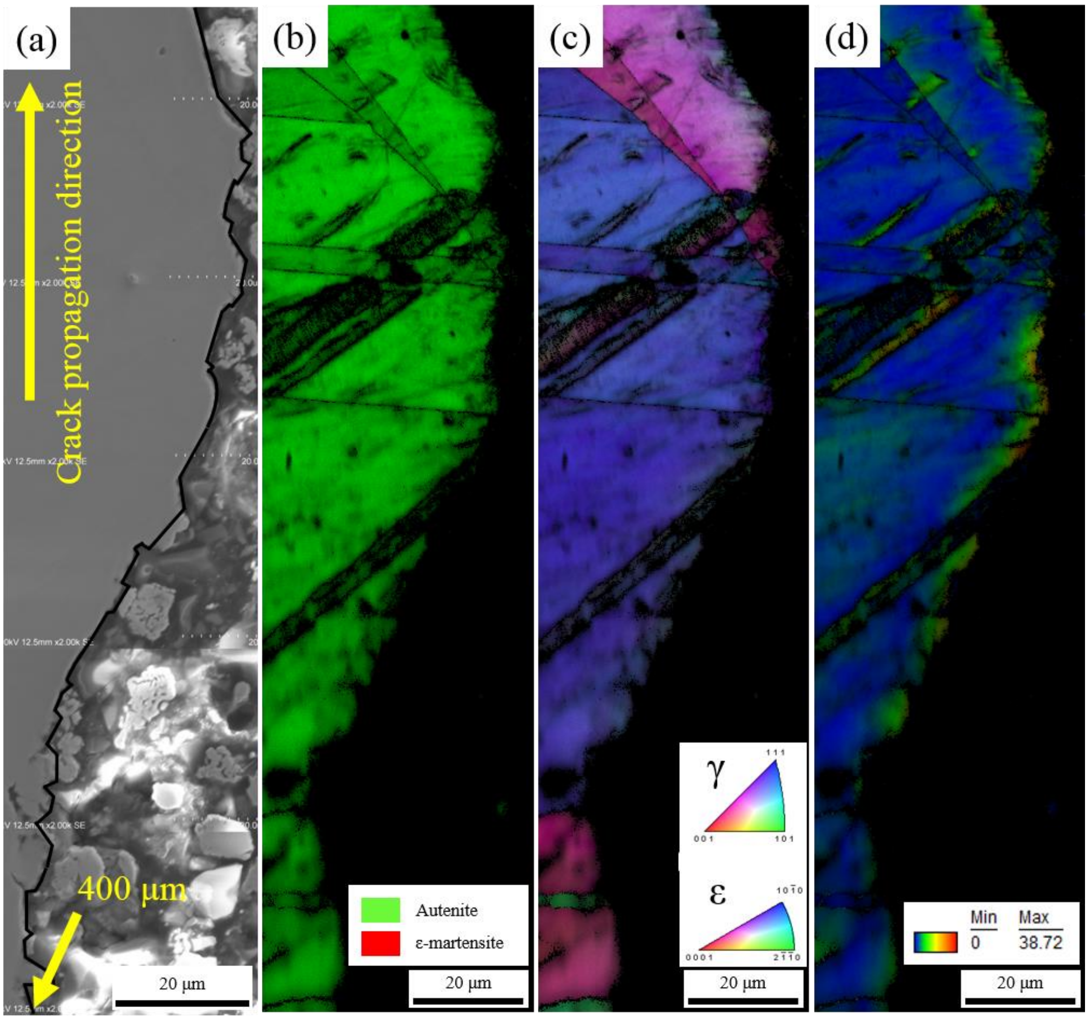

Fig. 3.5 Fatigue crack morphology at 400 μm from the top surface along the width central line of the Fe-30Mn-6Al alloy specimen. (a) Cross sectional SEM image near the fracture surface, and corresponding (b) phase map, (c) IPF map of the horizontal direction, and (d) grain reference orientation deviation (GROD) map. The EBSD images are overlapped on the image quality map.

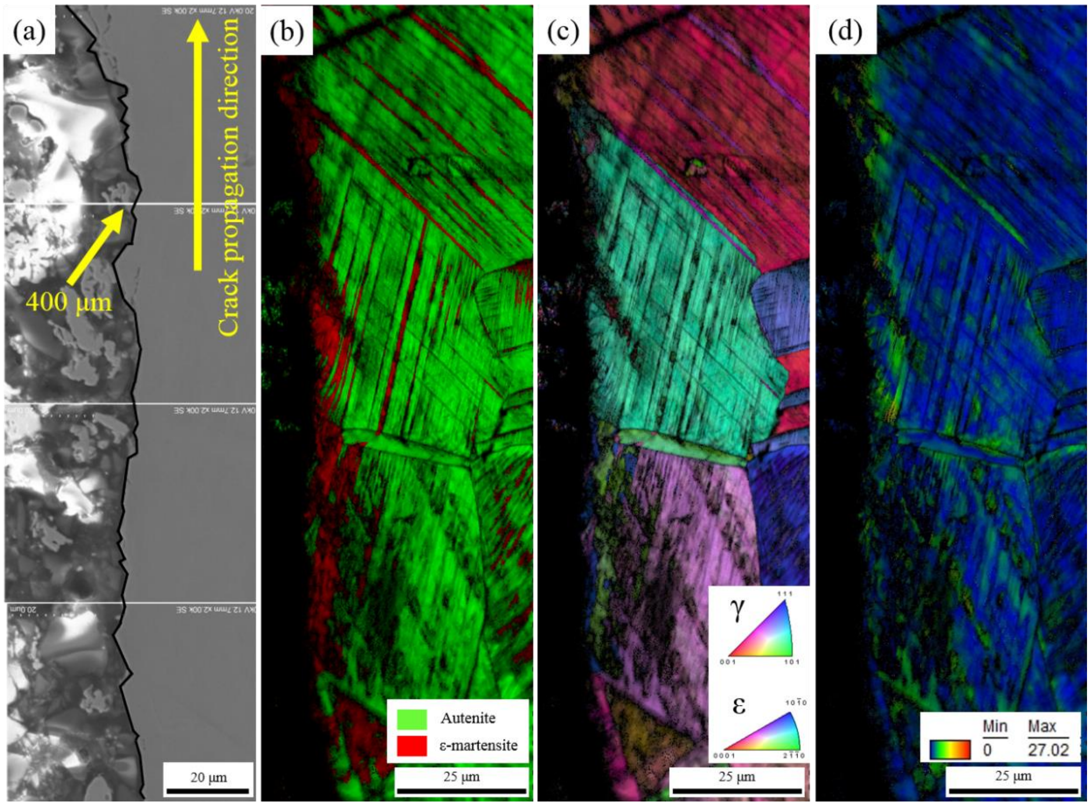

Fig. 3.6 Fatigue crack morphology at 400 μm from the top surface along the width central line of the Fe-30Mn-4Si-2Al alloy specimen. (a) Cross sectional SEM image near the fractured part, and corresponding (b) phase map, (c) IPF map of the horizontal direction, and (d) GROD map. The EBSD images are overlapped on the image quality map.

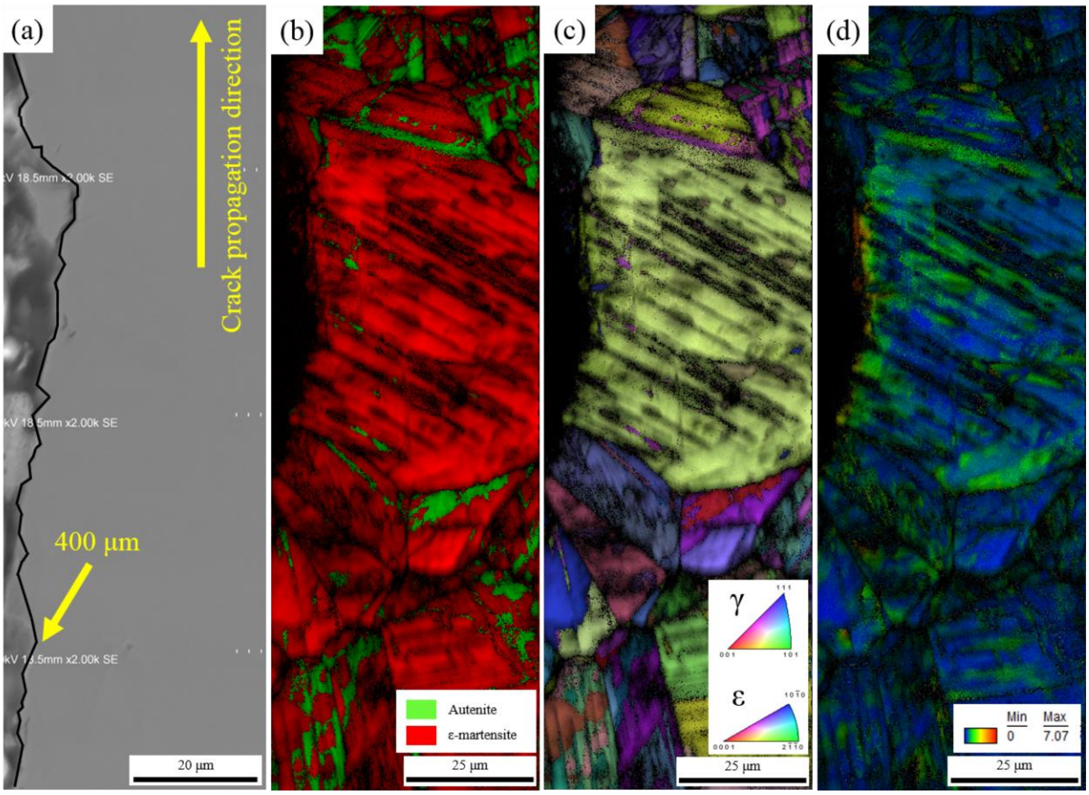

Fig. 3.7 Fatigue crack morphology at 400 μm from the top surface along the width central line of the Fe-30Mn-6Si alloy specimen. (a) Cross sectional SEM image near the fractured part, and corresponding (b) phase map, (c) IPF map of the horizontal direction, and (d) GROD map. The EBSD images are overlapped on the image quality map.

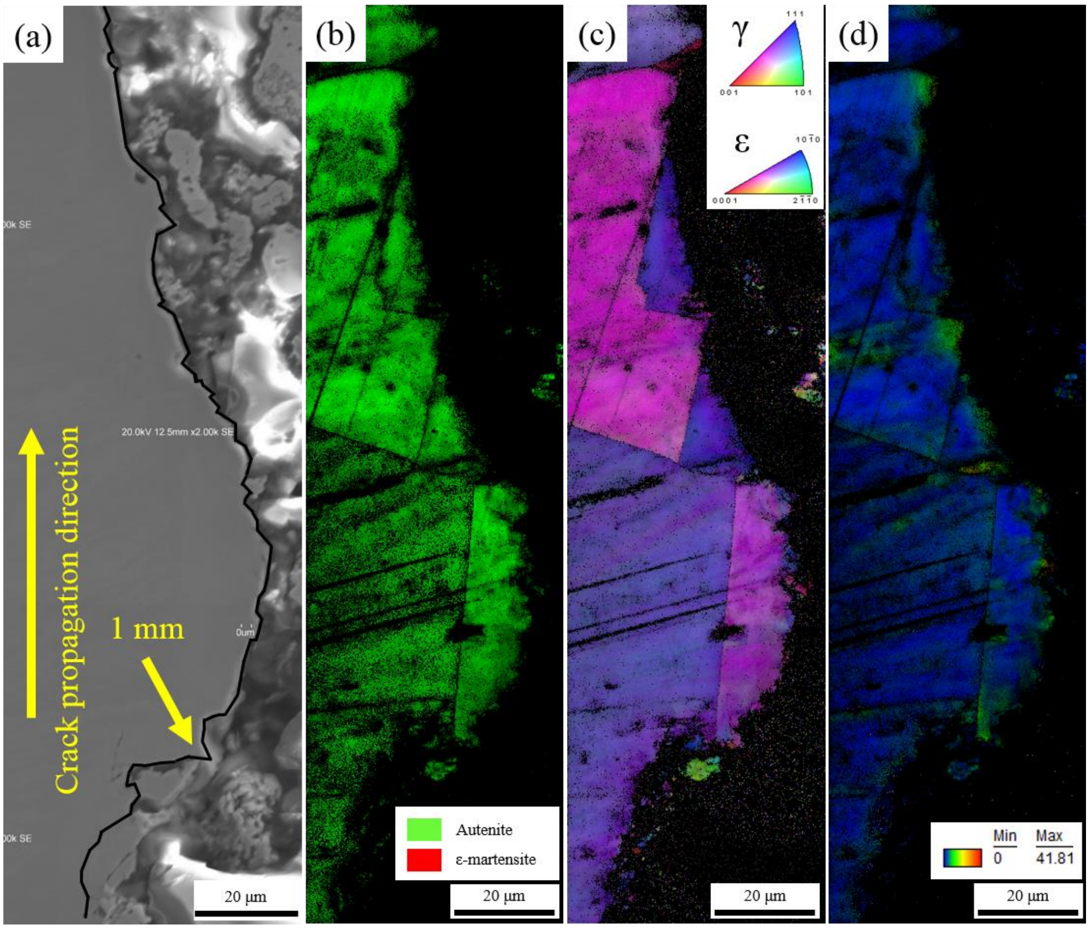

Fig. 3.8 Fatigue crack morphology at 1 mm from the top surface along the width central line of the Fe-30Mn-6Al alloy specimen. (a) Cross sectional SEM image near the fractured part, and corresponding (b) phase map, (c) IPF map of the horizontal direction, and (d) GROD map. The EBSD images are overlapped on the image quality map.

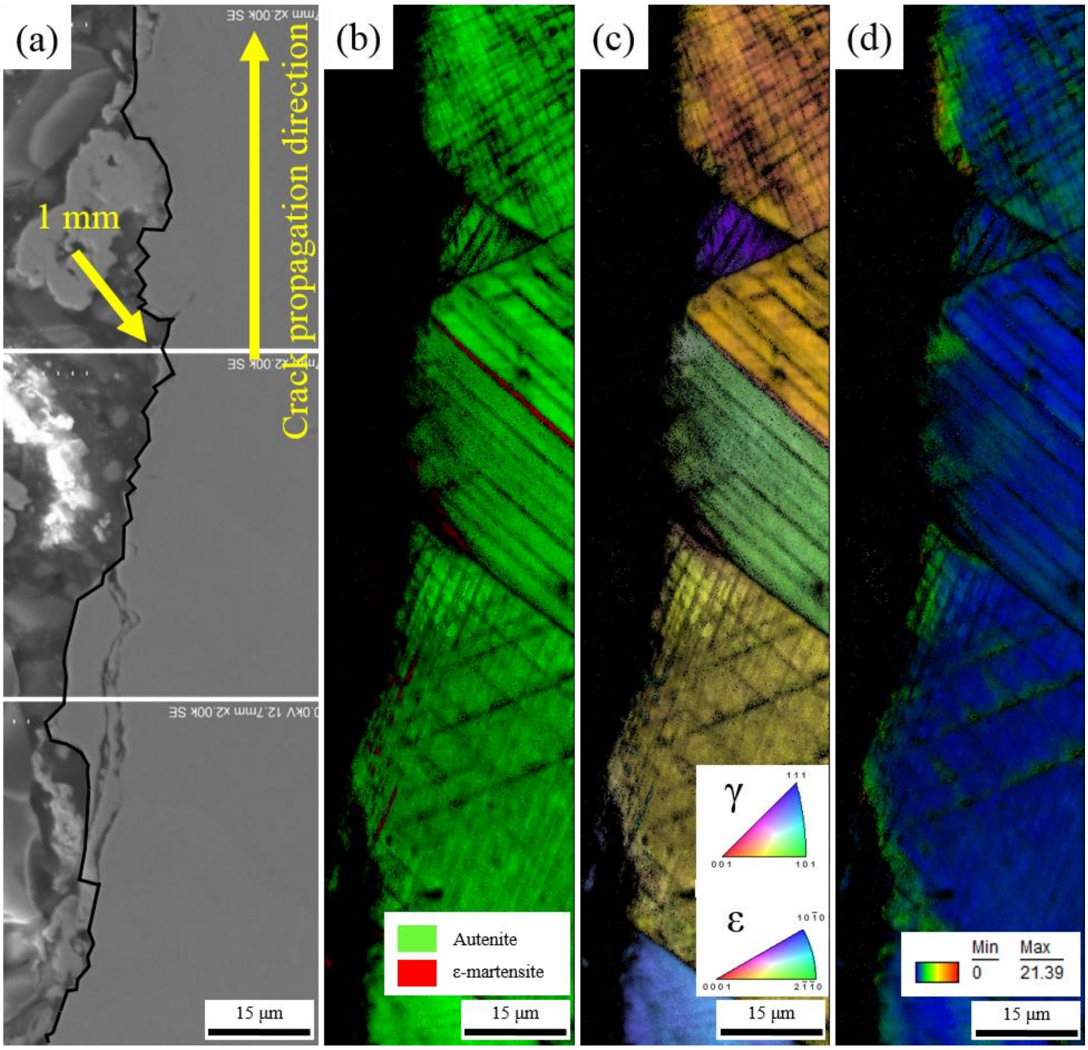

Fig. 3.9 Fatigue crack morphology at 1 mm from the top surface along the width central line of the Fe-30Mn-4Si-2Al alloy specimen. (a) Cross sectional SEM image near the fractured part, and corresponding (b) phase map, (c) IPF map of the horizontal direction, and (d) GROD map. The EBSD images are overlapped on the image quality map.

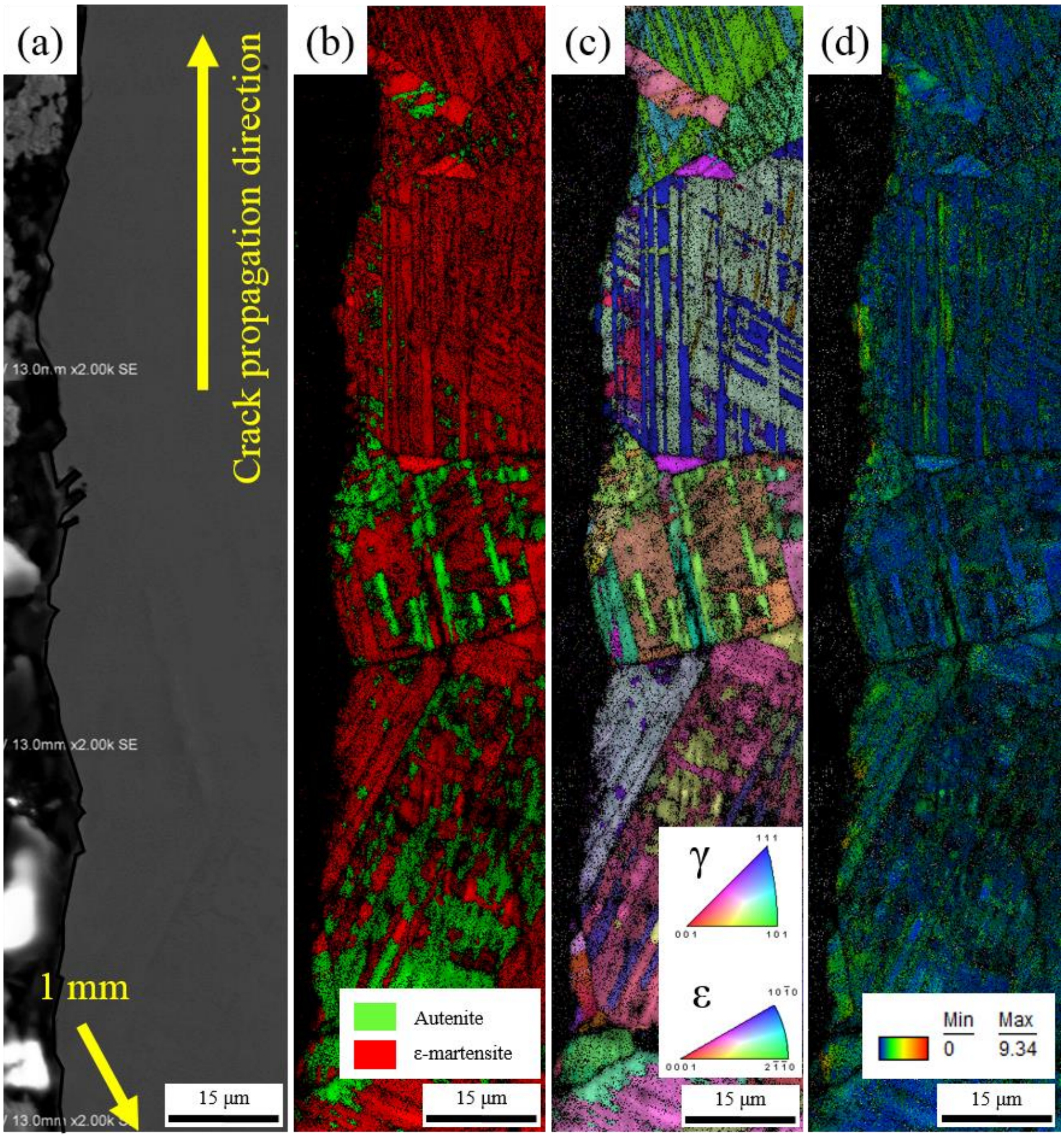

Fig. 3.10 Fatigue crack morphology at 1 mm from the top surface along the width central line of the Fe-30Mn-6Si alloy specimen. (a) Cross sectional SEM image near the fractured part, and corresponding (b) phase map, (c) IPF map of the horizontal direction, and (d) GROD map. The EBSD images are overlapped on the image quality map.

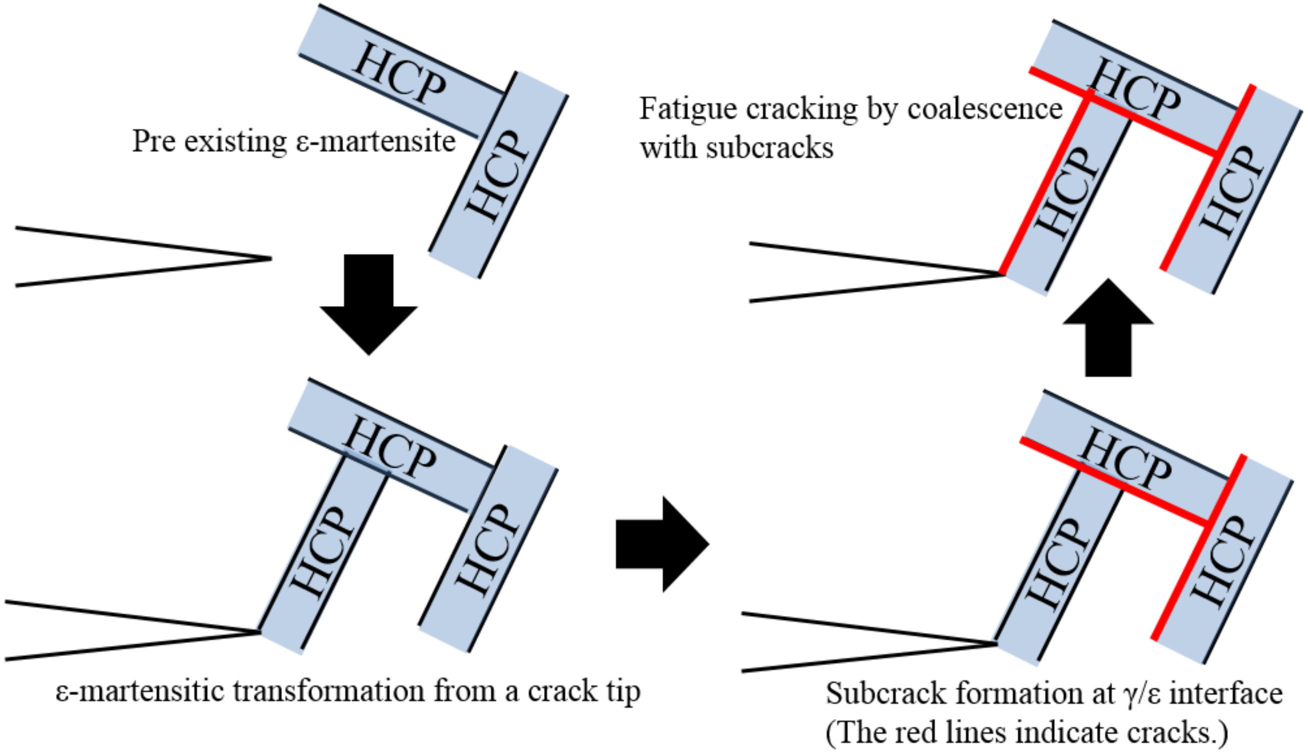

Fig. 3.11 Schematic diagrams of the fatigue cracking mechanism associated with pre-existing ε-martensite at a crack tip. The vertical direction corresponds to the loading direction.

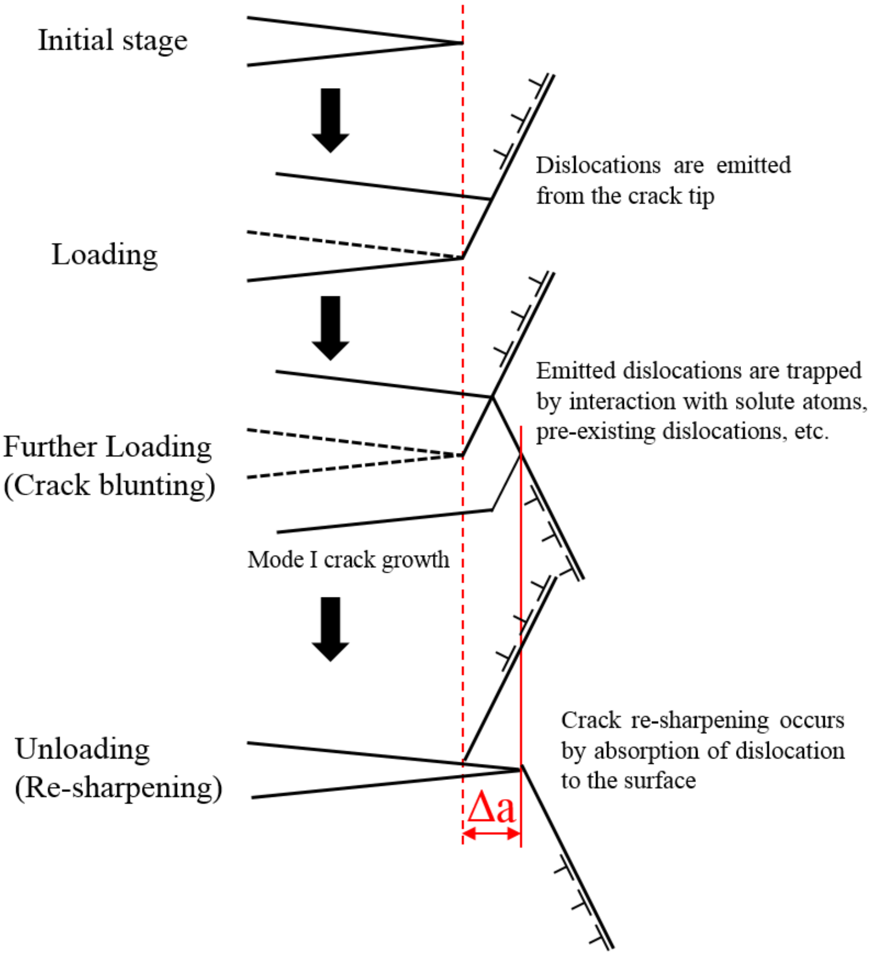

Fig. 3.12 Schematic diagram of crack tip deformation pertaining to dislocation emission. The vertical direction corresponds to the loading direction.

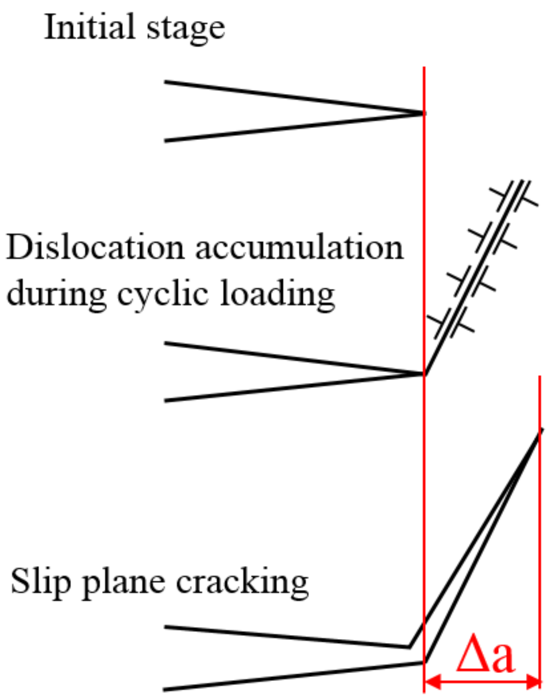

Fig. 3.13 Schematic diagram of fatigue slip plane cracking associated with dislocation accumulation at a crack tip. The vertical direction corresponds to the loading direction.

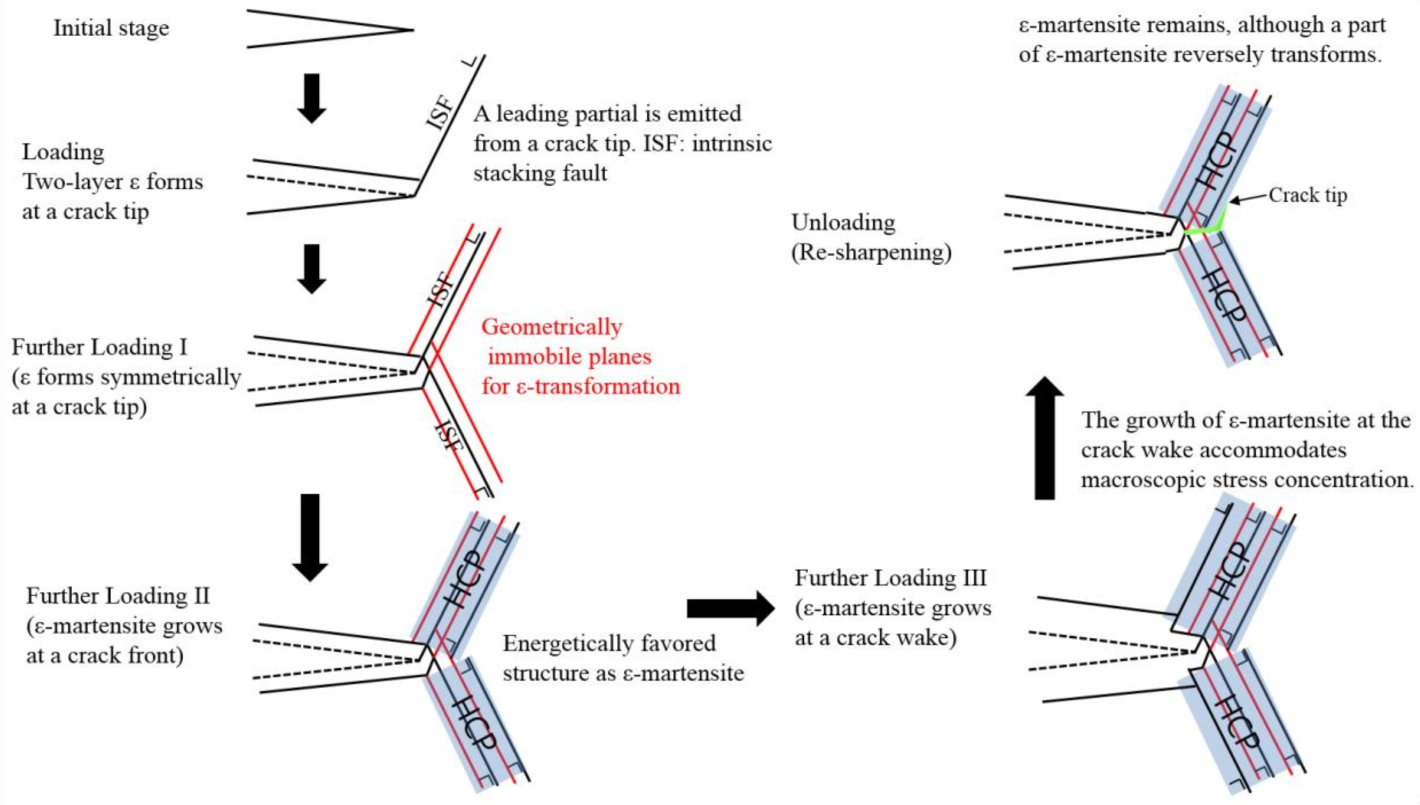

Fig. 3.14 Proposed model of a geometrical relationship between crack tip deformation and ε-martensitic transformation. The vertical direction corresponds to the loading direction. The red lines mark the neighboring slip planes of the intrinsic stacking faults.

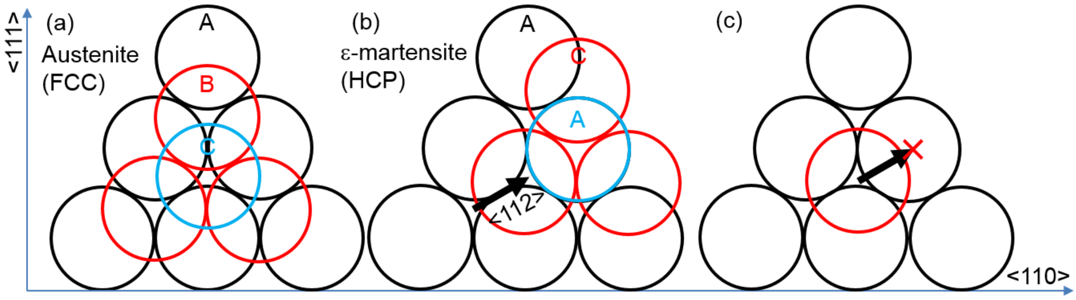

Fig. 3.15 Schematic diagram of the stacking sequences of (a) austenite and (b) ε-martensite. Atoms on the bottom, middle, and top layers are drawn as black, red, and blue, respectively. (c) Crystallographic restriction of partial dislocation motions in ε-martensite. Atoms on the bottom layer and a central atom on the middle layer are picked up from (b).

CHAPTER 4. Microscopic observation of low-cycle fatigue crack propagation for investigation of fatigue crack growth mechanism

4.1 Introduction

In chapter 2, the macroscopic crack growth behavior was observed by optical microscopy. In addition, the effects of ε-martensitic transformation were also investigated. However, the crack opening and closure behavior was not conducted during one cycle because of a low magnification and focusing problem by bending of specimen. Moreover, the crack growth mechanisms of the Fe-30Mn-4Si-2Al and Fe-30Mn-6Si alloys were proposed, using schematics in chapter 3. In the proposed mechanism, both alloys are expected to show different crack opening behavior. More specifically, a large crack tip opening can occurs because dislocation emission from the crack wake may contribute to a large crack tip opening in the Fe-30Mn-4Si-2Al alloy. However, the dislocation emission at the crack wake not contributes to the crack propagation. On the other hand, the Fe-30Mn-6Si alloy showed the brittle-like cracking and subcrack formation by pre-existing ε-martensite in chapter 2. Moreover, the plastic strain localization was not observed in chapter 3. These results indicate that the crack tip opening behavior of the Fe-30Mn-6Si alloy may quite different to the Fe-30Mn-4Si-2Al alloy. However, the fatigue crack growth behavior during one cycle was not investigated yet. Therefore, in order to examine the crack growth mechanisms proposed in chapter 3, further microscopic investigation is needed.

The observation of crack tip deformation requires a high magnification.

Accordingly, numerous in-situ SEM observation has been conducted to investigate the fatigue crack growth behavior [1, 2]. In-situ SEM observation has been mainly used to measure the crack opening displacement (COD) as well as to observe the crack propagation at applied maximum loading. Therefore, in order to investigate the fatigue crack tip deformation behavior and examine the crack growth mechanism proposed in chapter 2, in situ SEM observation during fatigue test was conducted with a high magnification. In present study, the Fe-30Mn-4Si-2Al and Fe-30Mn-6Si alloys were used for comparison of the crack tip deformation behavior. In addition, the crack opening behavior of both alloys during three cycles was observed.

4.2 Experimental procedure

In present study, the Fe-30Mn-4Si-2Al and Fe-30Mn-6Si alloys were used. The chemical composition and the results of tensile test are shown in chapter 1 [3]. Three alloys were forged and rolled at 1000 ℃, followed by annealing at 1000 ℃ for 1h and subsequently water-quenched. The alloys were cut by electric discharge machining (EDM) to prepare the fatigue specimens. Then, four through hole were introduced to fix the specimen in SEM machine during fatigue test. All surfaces of the fatigue specimens were mechanically polished to remove the EDM-affected layer. Then, a 100 (l) × 6 (w) × 36 (d) μm of FIB notch was introduced at center of the fatigue specimen to make a fatigue crack initiation site. The specimen geometry and size of FIB notch were shown in Fig. 4.1.

The tensile fatigue tests were carried out under optical microscopy to measure the fatigue crack length at room temperature. The fatigue tests were stress controlled by hydraulic fatigue machine at a frequency of 10 Hz. During the fatigue test, constant stress is applied and corresponding stress to 5% strain obtained from the tensile test results was used. When the fatigue crack length reached to 700 μm, the fatigue tests were conducted in SEM for the observation of crack tip deformation during one cycle at an accelerating voltage of 15 and 30 kV in the Fe-30Mn-6Si and Fe-30Mn-4Si-2Al alloy respectively. The applied stress for in situ SEM observation is same to that applied in tensile fatigue test. Total 11 points were used for the observation of crack tip deformation as shown in Fig. 4.2.

4.3 Experimental results

4.3.1 Fatigue crack growth rate

Fig. 4.3 shows the fatigue crack growth up to about 700 μm crack length in the Fe-30Mn-4Si-2Al and Fe-30Mn-6Si alloys. The fatigue crack initiation of the Fe-30Mn-6si alloy occurred at 7.6 × 10^4 cycles. Then, the fatigue crack propagated rapidly and reached to 700 μm crack length at 1.24 × 10^5 cycles. The fatigue crack initiation cycle is more than two times than the crack propagation cycle. These tendency was reported in chapter 2 [4, 5].

The Fe-30Mn-4Si-2Al alloy showed early crack initiation compared to the Fe-30Mn-6Si alloy at 6.0 × 10^4 cycles. Note that the crack propagation cycle to 700 μm crack length is 2.0 × 10^5 cycles and is longer than the Fe-30Mn-6Si alloy, even the crack initiation of the Fe-30Mn-4Si-2Al alloy occurred earlier than the Fe-30Mn-6Si alloy. And these results indicate that the low cycle fatigue resistance of the Fe-30Mn-4Si-2Al alloy is higher than the Fe-30Mn-6Si alloy.

4.3.2 In-situ SEM observation during one cycle in the Fe-30Mn-4Si-2Al alloy

When the fatigue crack length reached to 700 um, the microscopic fatigue crack tip deformation was observed in situ by SEM during one cycle. The two fatigue crack tips, which initiated and propagated from a FIB notch were observed in each specimen. Figs. 4.4 and 4.5 showed results of in situ observation in the Fe-30Mn-

4Si-2Al alloy during one cycle. The fatigue crack propagated perpendicular to loading direction as shown Fig. 4.4. Two annealing twin boundary (TB) were observed at vicinity of the crack tip. When the fatigue crack penetrated the annealing TB, a large crack deflection occurred along the TB. Note that the fatigue crack propagated along the TB, even the TB existed along the loading direction as shown in Fig. 4.4(a). These results indicate that the roughness-induced crack closure occurs because of the crack deflection at TB. During loading cycle, the fatigue crack opening occurred as shown in Fig. 4.4(a-f). However, the fatigue crack propagation was not observed. It should note that the fatigue crack growth was delayed at TB because of the roughness-induced crack closure.

Fig. 4.5 shows the fatigue crack growth behavior at opposite fatigue crack tip in the Fe-30Mn-4Si-2Al alloy. The subcrack initiation was observed near the fatigue crack tip as shown in Fig. 4.5(a). During the loading cycle, the main crack did not propagate as shown in Fig. 4.5(a-f). Instead, the crack coalesces between the main crack and subcrack occurred as shown in Fig. 4.5(f). Then, the new main crack tip was totally closed during the unloading cycle as shown in Fig. 4.5 (g-k).

4.3.3 In-situ SEM observation during one cycle in the Fe-30Mn-6Si alloy

Fig. 4.6 shows the microscopic fatigue crack growth behavior during one cycle in the Fe-30Mn-6Si alloy. The long subcrack in front of the main crack tip was observed as shown in Fig. 4.6(a). When the main crack tip was opened during loading cycle, the subcrack tip opening was also observed as shown in Fig. 4.6(a-f).

And some slip planes between the main crack and subcrack was observed. However, the crack propagation was not observed at both crack tips. The similar fatigue crack coalescence between the main crack and subcrack and cracking behavior along γ/ε or ε/ε interfaces in the Fe-30Mn-6Si alloy were reported in chapter 2.

Fig. 4.7 shows the crack growth behavior of subcrack tip shown in Fig. 4.6. During loading cycle, the fatigue crack tip opening was observed as shown in Fig. 4.7(a-f). However, the fatigue crack opening displacement (COD) of the Fe-30Mn-6Si alloy was smaller than the Fe-30Mn-4Si-2Al alloy as shown in Fig. 4.4 and 4.5. Note that the Fe-30Mn-6Si alloy shows small COD compared with the Fe-30Mn-4Si-2Al alloy, even though the similar fatigue crack length and rapid crack growth rate as shown in Fig. 4.3. A highly deformed area was observed in front of the subcrack tip during the loading cycle. Note that the Fe-30Mn-6Si alloy shows the subcrack initiation in front of the main crack tip.

Fig. 4.8 shows the crack growth behavior of an opposite main crack tip in the Fe-30Mn-6Si alloy. The cracking behavior was observed at vicinity of the crack tip at applied maximum load with sharp crack tip (Fig. 4.8(f)). These results indicate that the cracking behavior of the Fe-30Mn-6Si alloy occurs without accumulation of plastic strain because a crack tip blunting and re-sharpening behavior associated with dislocation-based deformation was not observed.

4.4 Discussion

In chapter 3, the crack growth mechanism of the Fe-30Mn-6Si alloy was proposed. The proposed mechanism was the subcrack initiation and crack coalescence with the main crack. In present chapter, the subcrack initiation in front of the main crack tip was observed as shown in Fig. 4.6. Fig. 4.10 shows the crack tip opening behavior observed during three cycles at maximum loading. The subcrack initiation was observed in front of subcrack tip. The pre-existing ε-martensite of the Fe-30Mn-6Si alloy has been reported [5]. Moreover, the subcrack formation caused from ε/ε interactions has been recognized to occur in high Mn austenitic alloys [6, 7]. In addition, in chapter 3, a large plastic strain localization was not observed in Fe-30Mn-6Si alloy. Therefore, the crack propagation by a large crack tip opening was not considered such as the crack tip blunting and re-sharpening behavior like the Fe-30Mn-6Al alloy. In this chapter, a large crack tip opening of the Fe-30Mn-6Si alloy was not observed as shown in Figs. 4.6 to 4.8. Therefore, the proposed crack growth mechanism of the Fe-30Mn-6Si alloy in chapter 3 is demonstrated.

The subcrack initiations were also observed in the Fe-30Mn-4Si-2Al alloy as shown in Fig. 4.5. However, after the crack coalescence, the Fe-30Mn-4Si-2Al alloy showed a large crack tip opening compared with the Fe-30Mn-6Si alloy. Fig. 4.9 shows the crack tip deformation behavior during three cycles at maximum loading in the Fe-30Mn-4Si-2Al alloy. The crack tip opening displacement gradually increased during three cycles. However, the fatigue crack propagation did not occur even though a large crack tip opening. Therefore, these behavior is not related to deformation-induced crack tip blunting and re-sharpening behavior because the fatigue crack propagates continuously when the blunting and re-sharpening behavior occurs with ductile striations. Therefore, the crack growth behavior observed in present chapter is associated with reverse ε-martensitic transformation at the crack tip proposed in chapter 3 because the proposed crack growth mechanism described the crack growth behavior, which occurred before formation of ductile striation.

In the proposed crack growth mechanism, dislocation emission occurs from the crack wake, causing a large crack tip opening. In addition, the fatigue crack propagation by a large plastic strain localization was suppressed due to reverse ε-martensitic transformation. In present chapter, a large crack tip opening was observed without the crack propagation as shown in Fig. 4.10. This result indicates that the crack propagation by the crack tip blunting and re-sharpening behavior not occurs and a large crack tip opening occurs due to dislocation emission from a crack wake. Therefore, the proposed crack growth mechanism of the Fe-30Mn-4Si-2Al alloy in chapter 3 is demonstrated.

In chapter 3 the considerable localization of plastic deformation of the Fe-30Mn-4Si-2Al alloy was observed near the fatigue crack path in chapter 3 as shown in Fig. 3.9. However, ductile striations was not observed in that region. Instead, the striation-like patterns were observed on fracture surface of the Fe-30Mn-4Si-2Al alloy as shown in Figs. 2.6(l) and 3.3(b). In addition, the fatigue crack growth rate was still low. These results indicate that the striation-like patterns are formed when a large crack tip opening occurs with decreased plastic strain localization, which is not enough to cause the crack tip blunting and re-sharpening behavior. Therefore, the fatigue crack growth rate was delayed when the crack growth behavior follows the proposed mechanism demonstrated in present chapter.

The other reason why the Fe-30Mn-4Si-2Al alloy shows the low cycle fatigue resistance is presence of annealing twinning boundary. In chapter 2, twinning boundaries were observed along the crack path. Moreover, the fatigue crack deflection occurred along the twinning boundaries, even if the twinning boundaries exists along loading direction. In chapter 2, the delay of crack propagation was explained by dislocation dissociation as shown in Fig. 2.13. In this chapter, the brittle cracking along the annealing twinning boundaries was observed as shown in Fig. 4.4. In addition, the fatigue crack not propagates, even though a considerable crack tip opening, when the crack tip reached to the twinning boundaries as shown in Fig. 4.4(f). These results indicate that the dislocation dissociation occurs to penetrate the annealing twinning boundary and the brittle cracking occurs due to accumulated dislocation along the twinning boundary [8-11]. In addition, the frequent crack deflections were observed as shown in Fig. 4.4. The crack deflections contribute to cause the roughness-induced crack closure. The roughness-induced crack closure was reported that the crack deflection deceases driving force at a crack tip [12-14]. In the result, the twin boundaries have positive and negative effects in the fatigue crack growth. The positive effects is that twin boundaries causes the crack deflection and deceases the driving force at a crack tip due to the roughness-induced crack closure. The negative effect is that the twin boundaries causes the dislocation accumulation. Therefore, the fatigue crack can propagate easily along the twinning boundary, showing brittle-cracking behavior.

4.5 Conclusion

In this study, the microscopic crack growth behavior during one cycle was observed in the Fe-30Mn-4Si-2Al and Fe-30Mn-6Si alloys by SEM to examine the crack growth mechanism proposed in chapter 3. From the results. The fatigue crack growth behavior of the Fe-30Mn-4Si-2Al and The Fe-30Mn-6Si alloys is same to the proposed mechanism. The main conclusions are summarized below.

(1) The twin boundaries in the Fe-30Mn-4Si-2Al alloy have positive and negative effects. The positive effects is the frequent crack deflection, causing decrease of driving force at the crack tip. The negative effect is brittle cracking occurrence along the twinning boundaries due to accumulation of dislocations emitted from the crack tip.

(2) The Fe-30Mn-6Si alloy showed the subcrack initiation in front of the main crack and subcrack tip. Then, the crack coalescence with the main crack occurred. Moreover, a large crack tip opening not occurred at maximum loading. Therefore, the proposed crack growth mechanism of the Fe-30Mn-6Si alloy is demonstrated.

(3) The Fe-30Mn-4Si-2Al alloy showed a large crack tip opening. However, the fatigue crack not propagated. Therefore, the large crack tip opening was not related to the blunting and re-sharpening behavior because those behavior caused the crack propagation at maximum loading. The large crack tip opening occurred due to the dislocation emission from a crack wake.

(4) In the proposed mechanism of the Fe-30Mn-4Si-2Al alloy, reverse transformation of ε-martensite contributed to suppression of the plastic strain localization, causing the delay of formation of ductile striations. The large crack tip opening of the present chapter without the crack propagation can demonstrate the formation of striation-like patterns in chapter 2 and decreased the plastic strain localization, is not enough to cause the blunting and re-sharpening behavior due to reverse transformation of ε-martensite. This is the main reason why the Fe-30Mn-4Si-2Al alloy shows low cycle fatigue resistance.

References

[1] C. Blochwitz, W. Tirschler, A. Weidner, Crack opening displacement and propagation rate of microstructurally short cracks, Mat. Sci. Eng. A 357 (2003) 264-269.

[2] W. Zhang, Y. Liu, Investigation of incremental fatigue crack growth mechanisms using in situ SEM testing, Int. J. Fat. 42 (2012) 14-23.

[3] M. Scharnweber, W. Tirschler, C-G. Oertel, W. Skrotzki, Mechanisms of short crack propagation in austenitic-ferritic duplex steel, Mat. Sci. Eng. A 595 (2014) 269-283.

[4] K. yamada, M. Koyama, T. Kaneko, K. Tsuzaki, Positive and negative effects of hydrogen on tensile behavior in polycrystalline Fe-30Mn-(6-x)Si-xAl austenitic alloys, Scr. Mat. 105 (2015) 57-57.

[5] Y.-B. Ju, M. Koyama, T. Sawaguchi, K. Tsuzaki, H. Noguchi, In situ microscopic observations of low-cycle fatigue-crack propagation in high-Mn austenitic alloys with deformation-induced ε-martensitic transformation, Acta Mater. 112 (2016) 326-336.

[6] I. Nikulin, T. Sawaguchi, K. Tsuzaki, Effect of alloying composition on low-cycle fatigue properties and microstructure of Fe–30Mn–(6−x)Si–xAl TRIP/TWIP alloys, Mater. Sci. Eng. A 587 (2013) 192-200.

[7] M. Koyama, T. Sawaguchi, K. Tsuzaki, Effects of Si on Tensile Properties Associated with Deformation-Induced ε-Martensitic Transformation in High Mn Austenitic Alloys, Mater. Trans. 56 (2015) 819-825.

[8] S. Takaki, T. Furuya, Y. Tokunaga, Effect of Si and Al Additions on the Low Temperature Toughness and Fracture Mode of Fe-27Mn Alloys, ISIJ Int. 30 (1990) 632-638.

[9] K. Tanaka, T. Mura, Fatigue crack growth along planar slip bands, Acta Metall. 32 (1984) 1731-1740.

[10] S. Kajiwara, D. Liu, T. Kikuchi, N. Shinya, Remarkable improvement of shape memory effect in Fe-Mn-Si based shape memory alloys by producing NbC precipitates, Scr. Mater. 44 (2001) 2809-2814.

[11] Y.H. Wen, L.R. Xiong, N. Li, W. Zhang, Remarkable improvement of shape memory effect in an Fe–Mn–Si–Cr–Ni–C alloy through controlling precipitation direction of Cr23C6, Mater. Sci. Eng. A 474 (2008) 60-63.

[12] G.B. Olson, M. Cohen, A general mechanism of martensitic nucleation: Part I. General concepts and the FCC → HCP transformation, Metall. Trans. A 7 (1976) 1897-1904.

[13] M. Koyama, T. Sawaguchi, K. Tsuzaki, Premature Fracture Mechanism in an Fe-Mn-C Austenitic Steel, Metall. Mater. Trans. A 43 (2012) 4063-4074.

[14] J.-B. Seol, J.E. Jung, Y.W. Jang, C.G. Park, Influence of carbon content on the microstructure, martensitic transformation and mechanical properties in austenite/ε-martensite dual-phase Fe-Mn-C steels, Acta Mater 61 (2013) 558-578.

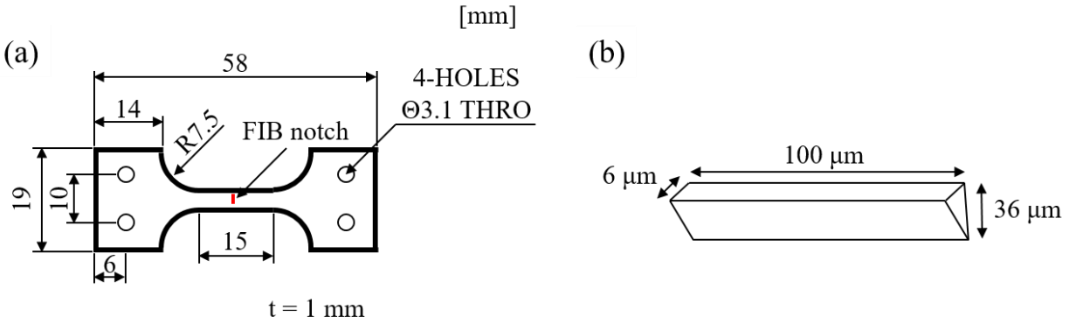

Fig. 4.1 specimen geometry used for the fatigue test. (a) Top view of the specimen with FIB notch. (b) Detailed schematic of the shape of the FIB notch is indicated in (a).

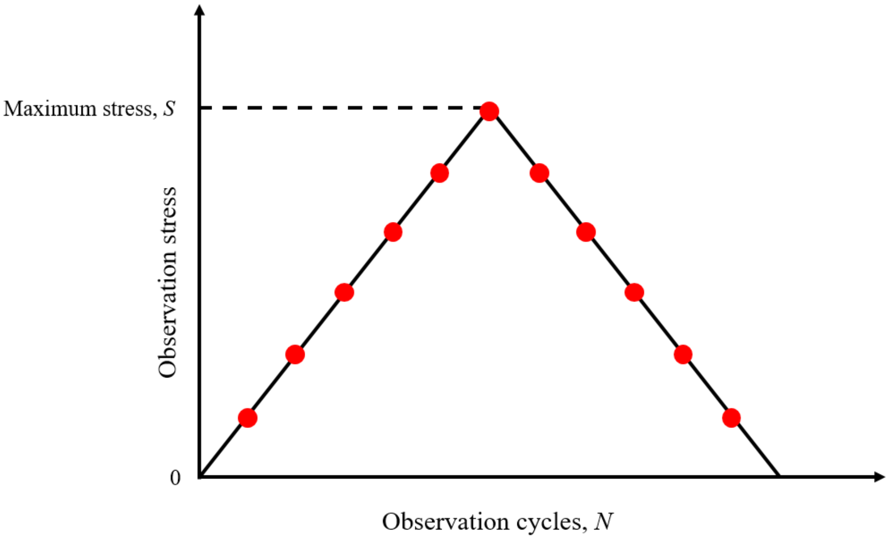

Fig. 4.2 Schematic of the observation point for in-situ during one cycle.

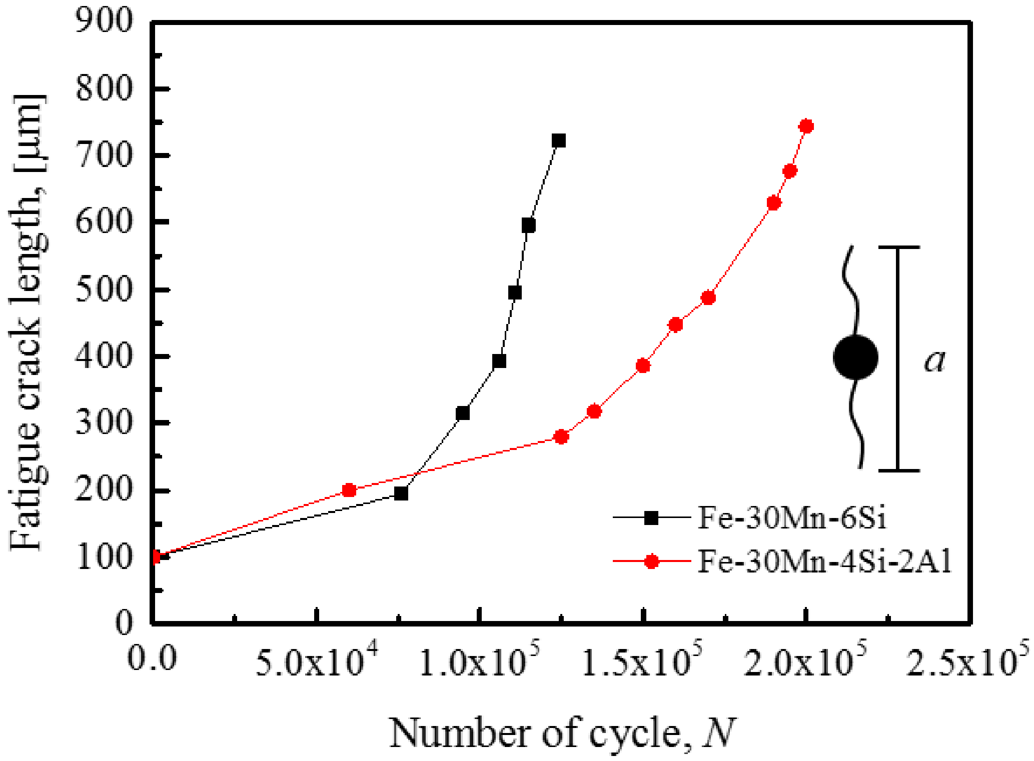

Fig. 4.3 Fatigue crack length (*l*) as a function of the number of cycles (*N*) for the Fe-30Mn-4Si-2Al and Fe-30Mn-6Si alloys tested.

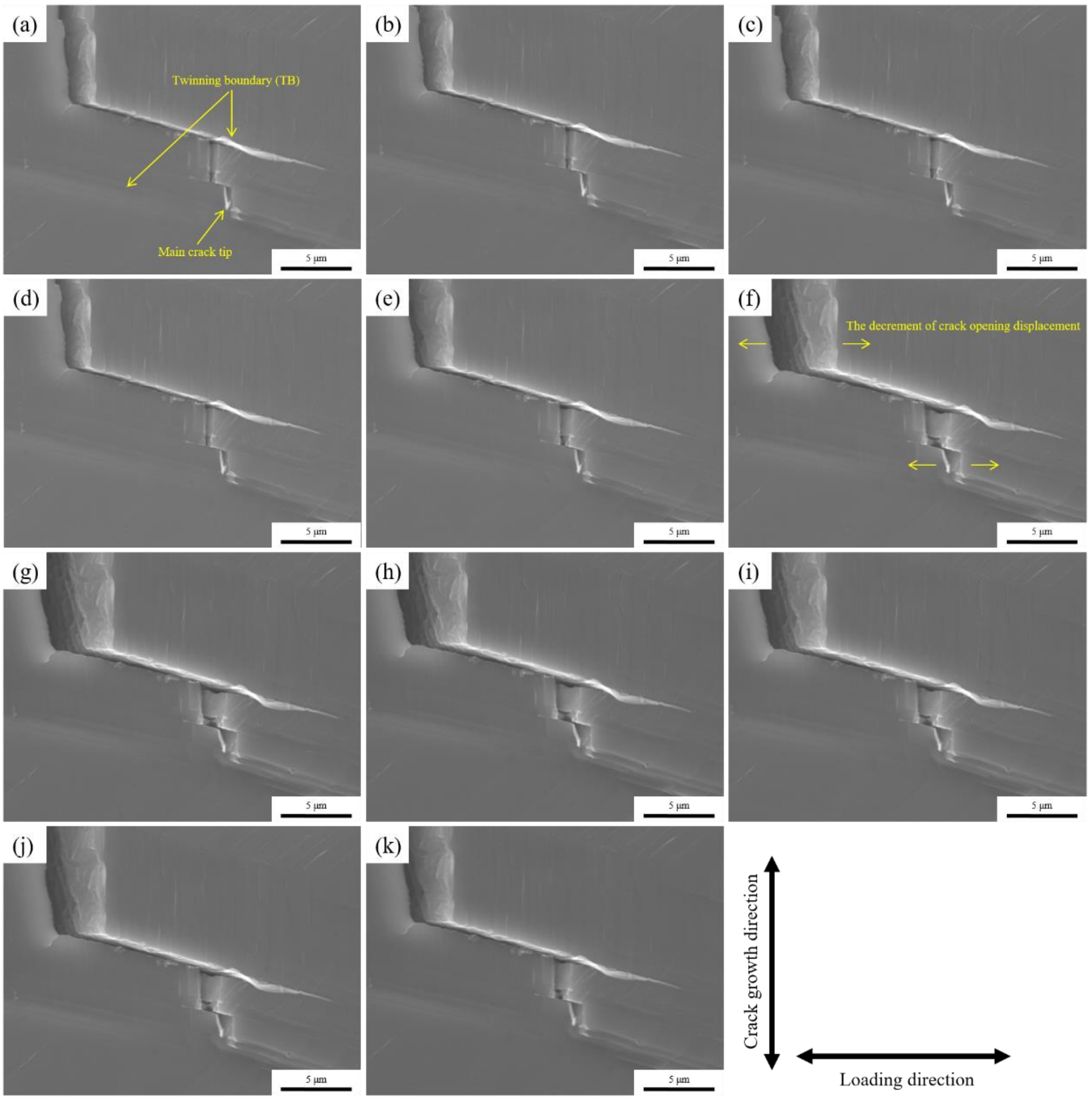

Fig. 4.4 In situ SEM observation images of the Fe-30Mn-4Si-2Al alloy at one of main fatigue crack tip with 750 μm crack length during one cycle.

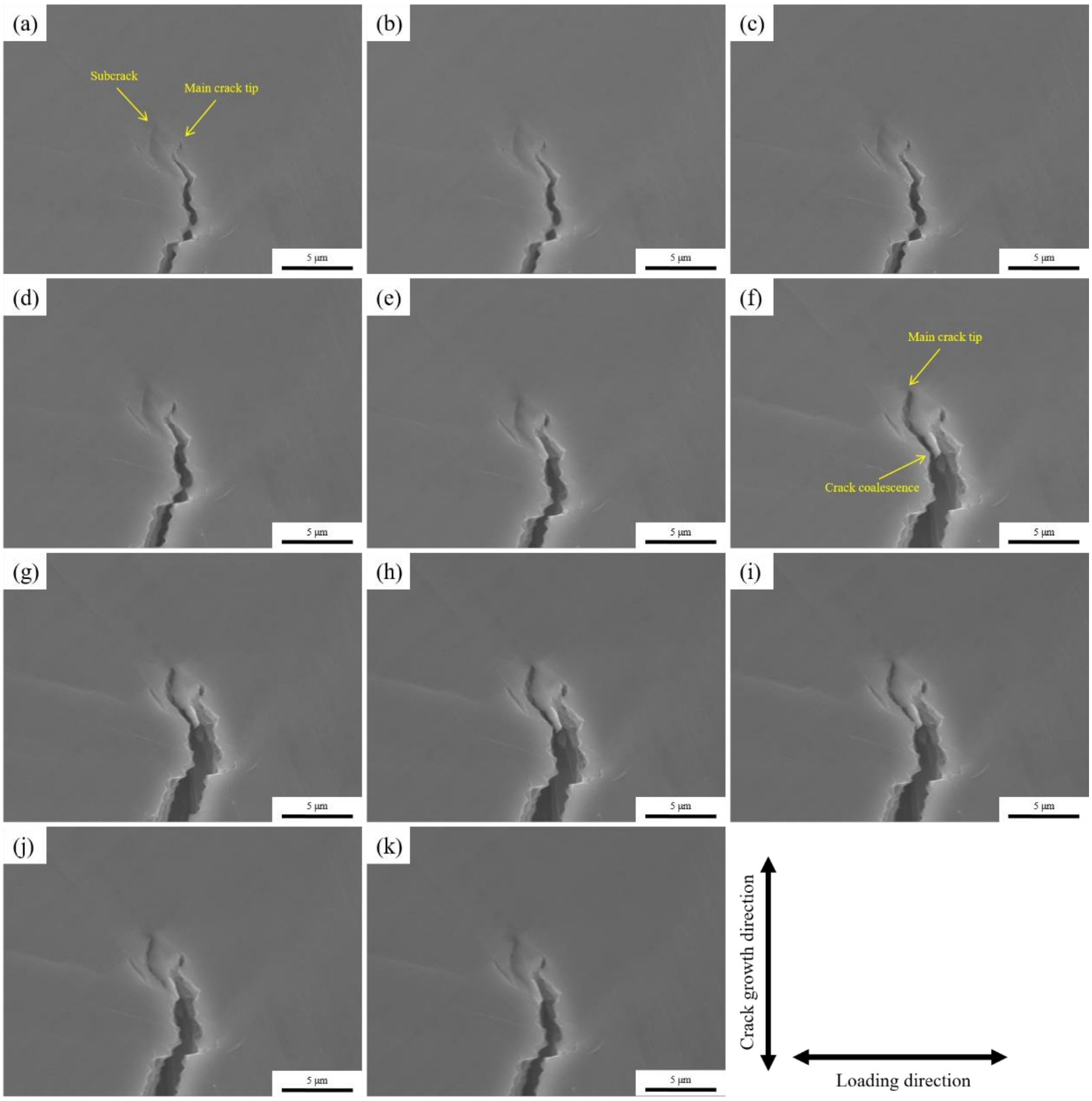

Fig. 4.5 In situ SEM observation images of the Fe-30Mn-4Si-2Al alloy at the other of main fatigue crack tip with 750 μm crack length during one cycle.

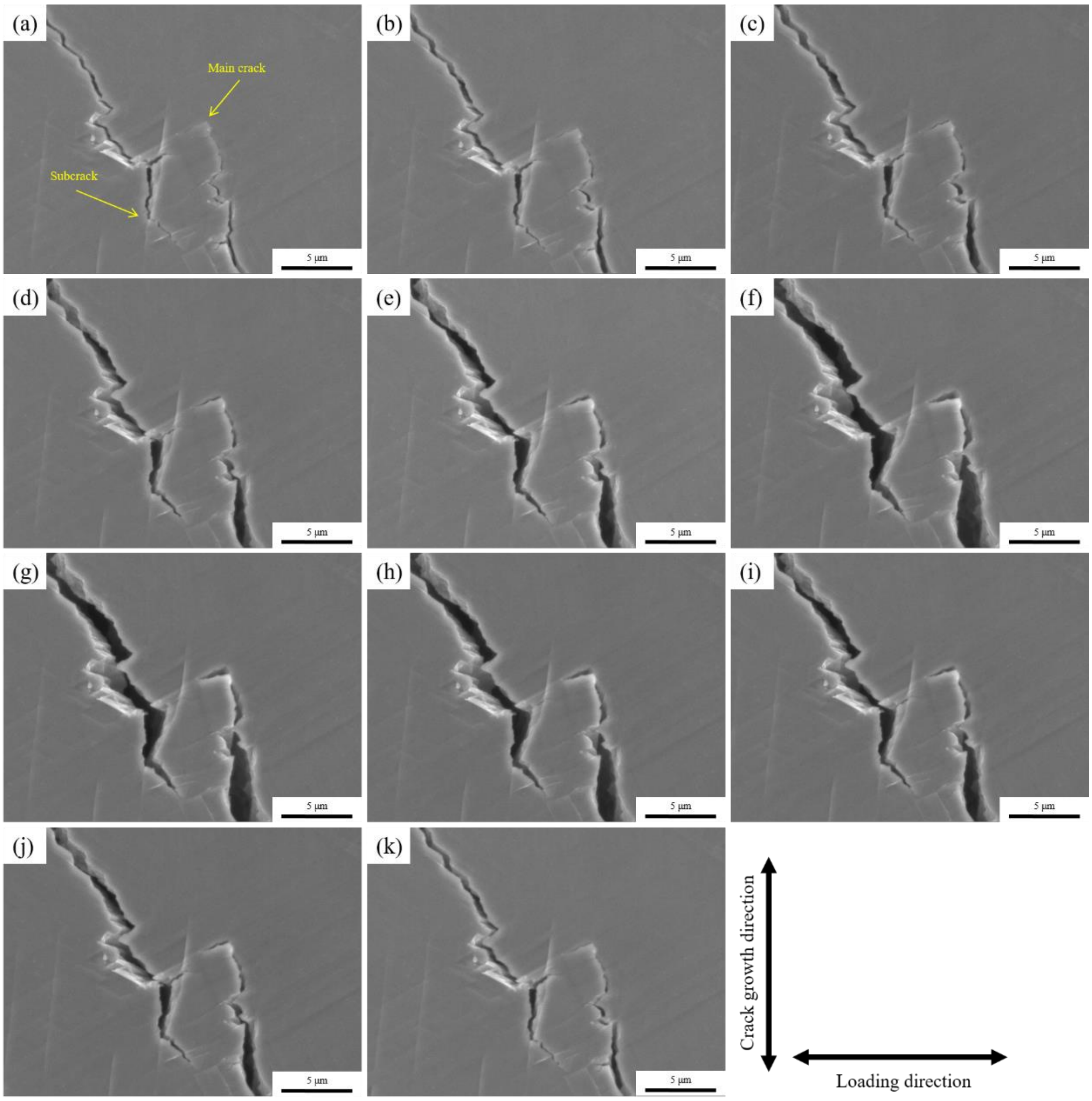

Fig. 4.6 In situ SEM observation images of the Fe-30Mn-6Si alloy at one of main fatigue crack tip with 730 μm crack length during one cycle.

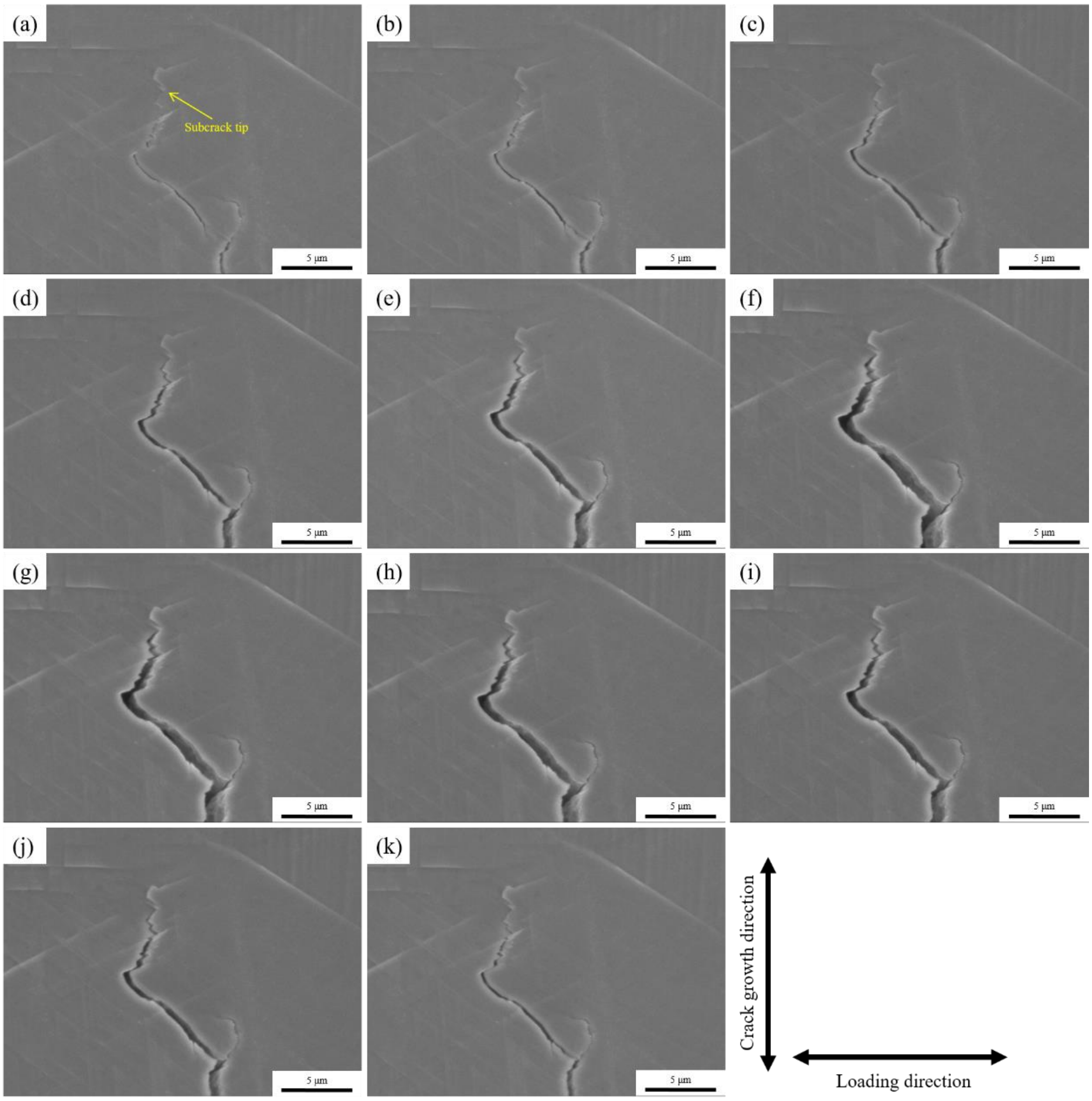

Fig. 4.7 In situ SEM observation images of the Fe-30Mn-6Si alloy at subcrack tip with 730 μm crack length during one cycle.

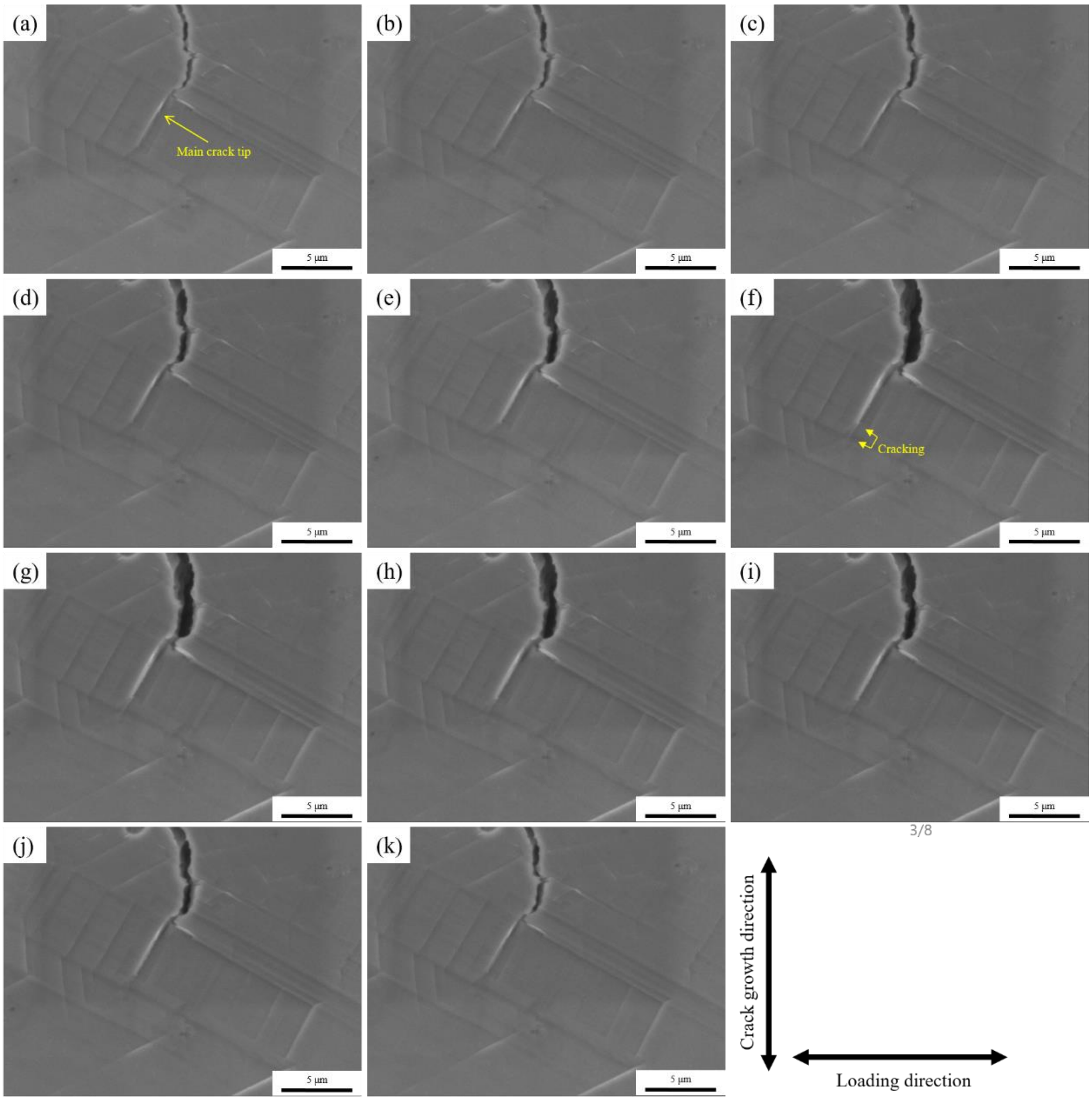

Fig. 4.8 In situ SEM observation images of the Fe-30Mn-6Si alloy at the other of main fatigue crack tip with 730 µm crack length during one cycle.

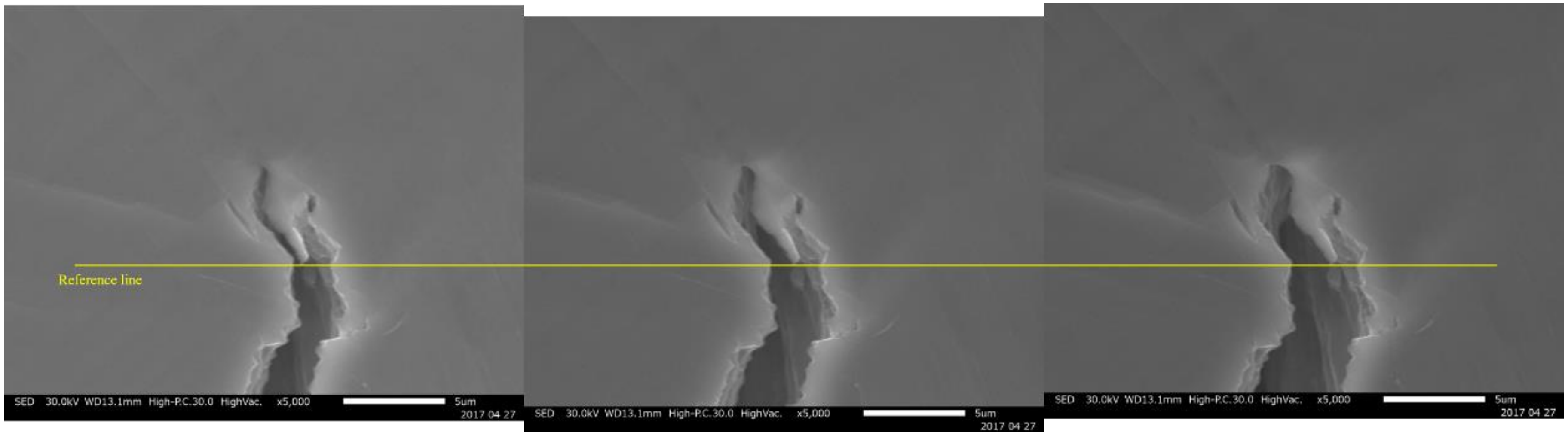

Fig. 4.9 Crack tip deformation behavior of the Fe-30Mn-4Si-2Al alloy at maximum loading applied in the fatigue test during three cycles.

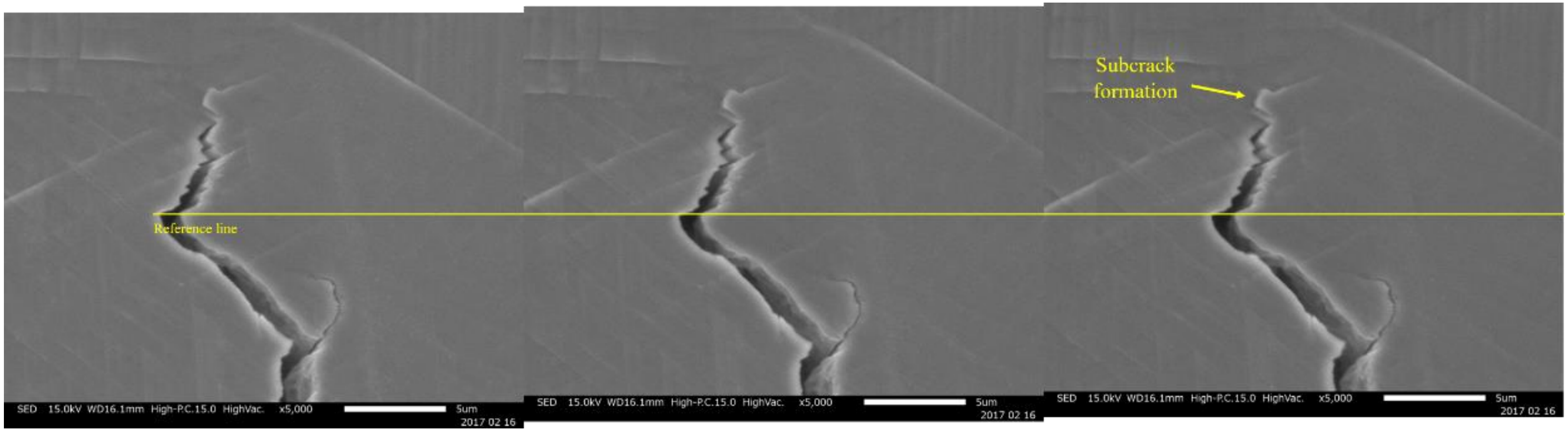

Fig. 4.10 Crack tip deformation behavior of the Fe-30Mn-6Si alloy at maximum loading applied in the fatigue test during three cycles.

CHAPTER 5. GENERAL CONCLUSION

In this thesis, the macroscopic and microscopic fatigue crack growth behaviors of high Mn steels were observed in situ by an optical microscopy and scanning electron microscope (SEM) during low cycle fatigue test. The Fe-30Mn-6Al, Fe-30Mn-4Si-2Al and Fe-30Mn-6Si alloys were used for fatigue test. To investigate the fatigue crack growth behavior, fracture surface observations, electron backscatter diffraction (EBSD) measurements and crack opening behaviors during one cycle are used.

The fatigue crack initiation and propagation are closely related to microstructure of each material. Therefore, the fatigue crack growth behaviors are investigated with microstructures near the fatigue crack. In particular, the deformation-induced ε-martensitic transformation and ε-martensite associated fatigue crack growth behavior are focused on low cycle fatigue. In addition, the fatigue crack propagation mechanism are investigated with or without ε-martensitic transformation and pre-existing ε-martensite.

The high Mn austenitic steels have been studied in many industries such as a damping materials for building, structural materials for automobile industries, etc. Even there are many kinds of chemical compositions in the high Mn austenitic steels, I believe that present investigations can be used in various industries, which considered the application of high Mn austenitic steels and tried to solve the fatigue crack problems of applied high Mn steels in low cycle fatigue as a fundamental study in view point of fatigue.

The results of the experimental works were obtained as following:

1. The Fe-30Mn-6Al alloy exhibited fatigue crack growth along {111} slip plane in short fatigue crack region. However, the fatigue crack growth behavior changed to deformation-induced blunting and re-sharpening behavior accompanied by striation formation. These crack growth behaviors require a large degree of plastic strain localization. And these fatigue crack growth mechanisms in the Fe-30Mn-6Al alloy are typical in ductile FCC metals.

2. The Fe-30Mn-6Si alloy showed the cracking behavior along γ/ε or ε/ε interfaces with a low plastic strain irrespective of crack length. Moreover, frequent subcrack formations in front of the main crack tip were observed. These subcracks caused crack coalescence with the main crack and acceleration of the crack growth rate. The Fe-30Mn-6Si alloy has many stress concentration site such as γ/ε or ε/ε interfaces occurred by deformation-induced ε-martensitic transformation and pre-existing ε-martensite. When the main crack initiated, these interfaces received high stress concentration as well as the fatigue crack tip. Therefore, the subcracks easily initiated and coalesced with the main crack instead of plastic strain accumulation at the crack tip.

3. The Fe-30Mn-4Si-2Al alloy showed the crack growth along γ/ε interfaces when the fatigue crack is short. The fatigue crack propagation mechanism changed to the crack blunting and re-sharpening behavior like the Fe-30Mn-6Al alloy in long fatigue crack length. However, reverse transformation of ε-martensite suppressed the plastic strain localization. In addition, the dislocation emission from a crack wake contributed to a large crack tip opening. However, the fatigue crack did not propagate. Therefore, the

deformation-induced blunting and re-sharpening behavior was delayed due to decreased plastic strain localization by reverse motion of dislocation. Instead, the striation-like patterns was formed by a large crack tip opening and fatigue crack growth rate was low.

4. The fatigue crack growth rate delayed by the annealing twinning boundaries was observed in the Fe-30Mn-4Si-2Al alloy. However, the brittle-like cracking occurred along the twinning boundaries. The dislocation dissociation occurred to penetrate the twinning boundaries. Moreover, the fatigue damage is accumulated along the twinning boundaries. Therefore, the fatigue crack propagates along the twinning boundaries easily and the fatigue crack growth penetrating the twinning boundaries was delayed.

5. The pre-existing ε-martensite has negative effects to the fatigue crack growth, causing brittle-like cracking and subcrack formation along ε/ε interfaces. Moreover, the twinning boundaries existing perpendicular to the fatigue crack growth have positive effects to the fatigue crack growth, preventing the fatigue crack growth. In addition, the crack deflections at the twinning boundaries has a positive effect. These crack deflections cause the roughness-induced crack closure and decrease the driving force at the crack tip. Therefore, the Fe-30Mn-4Si-2Al alloy is optimized to low cycle fatigue due to suppression of the plastic strain localization and the positive effect of twinning boundaries without the pre-existing ε-martensite.

Acknowledgement

The present work has been carried out during the author’s tenure of a doctoral course at the department of hydrogen energy systems, faculty of engineering, Kyushu University under the supervision of Prof. Hiroshi Noguchi.

My greatest appreciation and gratitude goes to my supervisor Prof. Hiroshi Noguchi for his esteemed guidance, valuable suggestions and numerous discussions. I am especially grateful to Prof. Kaneaki Tsuzaki and Prof. Hiroyuki Toda for the valuable guidance and advice.

Thanks are due to all the members of Solid Mechanics Laboratory for their kind co-operation and assistance. I would like to thank Prof. Motomichi Koyama for numerous and valuable discussions during my doctoral course.

In particular, I would like to thank Prof. Seong-Kyun Cheong in Seoul National University of Science and Technology for encouragement and support.

Finally, I would like to thank my family for all their help and supports.